Spatiotemporal Variability of Methane Ebullition from Lake Sediments

by

Benjamin Paul Scandella

B.S., University of North Carolina at Chapel Hill (2008)
S.M., Massachusetts Institute of Technology (2010)

Submitted to the Department of Civil and Environmental Engineering
in partial fulfillment of the requirements for the degree of

Doctor of Philosophy

at the

MASSACHUSETTS INSTITUTE OF TECHNOLOGY

June 2016

Author .....
Department of Civil and Environmental Engineering
May 19, 2016

Certified by .....
Ruben Juanes
Associate Professor,
Department of Civil and Environmental Engineering and
Department of Earth, Atmospheric and Planetary Sciences
Thesis Supervisor

Accepted by .....
Heidi M. Nepf
Donald and Martha Harleman Professor of
Civil and Environmental Engineering
Chair, Departmental Committee for Graduate Students

Spatiotemporal Variability of Methane Ebullition from Lake Sediments

by

Benjamin Paul Scandella

Submitted to the Department of Civil and Environmental Engineering
on May 19, 2016, in partial fulfillment of the
requirements for the degree of
Doctor of Philosophy

Abstract

Methane is a potent greenhouse gas, and natural sources to the atmosphere include inland waterways and shallow oceans. However, the magnitude of these emissions and their potential for feedbacks with climate change remain poorly constrained. In many settings the majority of atmospheric methane emissions is delivered by bubbles, and the spatiotemporal heterogeneity of ebullition makes measurement challenging and impacts bubble dissolution and atmospheric emissions. In this thesis, we present an analysis of both the episodicity and spatial structure of methane venting from soft sediments in a eutrophic lake over a range of spatial scales, from 1 cm to 20 m, and using a combination of field observations and laboratory experiments.

Field-scale measurements of ebullition were acquired at the bottom of Upper Mystic Lake, MA, USA, using a high-resolution multibeam sonar during multiple deployments over a 9-month period. The sonar was calibrated to estimate the gas flow rates throughout a 330 m^2 lateral observation area with resolution of 0.5 m. The results confirm that ebullition is strongly episodic, with distinct regimes of high- and low-flux largely controlled by changes in hydrostatic pressure. Statistical analysis shows that the spatial pattern of ebullition becomes homogeneous at the sonar's resolution over timescales of hours (for high-flux periods) or days (for low-flux periods), demonstrating that meter-scale methane vents are ephemeral rather than persistent.

Laboratory-scale measurements were made in a controlled incubation of reconstituted sediments from the same field site. Image analysis of the 0.14 m^2 observation area allowed identification of individual bubble outlets and resolved their location to $\sim$ 1 cm. While ebullition events were typically concentrated in bursts lasting $\sim$ 2 min, some major outlets showed persistent activity over the scale of days and even months. This persistence was surprising given the ephemerality of spatial structure at the field-scale. It suggests that, at the centimeter scale, conduits are re-used as a result of a drop in tensile strength due to deformation of sediments by the rising

bubbles. By combining novel measurement techniques at different scales, we elucidate the mechanisms governing bubble growth and mobility, thereby supporting estimates of global methane fluxes from lakes and how their magnitude may vary with climate change.

Thesis Supervisor: Ruben Juanes
Title: Associate Professor,
Department of Civil and Environmental Engineering and
Department of Earth, Atmospheric and Planetary Sciences

Acknowledgments

I thank my advisor, Ruben Juanes, for his encouragement, patience and support throughout my time here at MIT. His boundless enthusiasm for research is infectious, and it's a privilege to work with him. I hope that I've learned a fraction of his unmatched writing skill and fabulous teaching technique and that I will some day inspire students as he does.

My other thesis committee members have also supported my work deeply. Harry Hemond brought to bear not only his extensive experience with field work and instrument design, but also critical assistance and equipment I needed to run the campaign on Upper Mystic Lake. Carolyn Ruppel's feedback made the research stronger, and she showed me the excitement of being part of a community of scientific collaborators. Charlie Harvey always offered a fresh research perspective and inspired me with his support for climate leadership at MIT.

This research would not have been possible without a long list of scientific collaborators. I am especially grateful for white board brainstorming sessions and field work adventures with Kyle Delwiche, whose critical thinking and encouragement helped me navigate the sometimes treacherous waters of the Sea of Doctorate. Other field work contributors at MIT include Aldrich Castillo, Ruby Fu, Dave Griffith, Fatima Hussain, Peter Kang, Hanan Karam, Amy Mueller, Matt Orosz, Jeff Rominger, Schuyler Senft-Grupp, Mathias Trojer, Dave Whittleston and Teresa Yamana. I've also been lucky to work with a few wonderful MIT undergraduates through the UROP program: Ju Chulakadabba, Jared Darby, Michelle Dutt, Hannah Wood. Mark Belanger and the Edgeton Machine Shop helped fabrication of the field and experimental equipment. The sonar calibration was made possible thanks to Jens Greinert and Peter Urban of GEOMAR and Carlo Lanzoni, Liam Pillsbury and Tom Weber of UNH. Research on Upper Mystic Lake was enabled by Coach Kenneth Legler and the Tufts Sailing Team, as well as Steve Hood and others at the Winchester Boat Club. The U.S. Geological Survey at Woods Hole supported the entire project, led by Carolyn Ruppel and John Pohlman and including Wayne Baldwin, Emile Bergeron, Dann Blackwood, Jon Borden, Bill Danforth, Marinna Martini, Ellyn Montgomery and Chuck Worley. I was also fortunate to have the consistent support and involvement of the sonar manufacturer, Imagenex Technology Corporation, and especially Doug Wilson and Steve Curnew. To these people and all the others who helped me to enter the wild world of field research, I am immensely grateful.

I was fortunate to be part of a number of delightful communities here at MIT. The Juanes group has grown from a small, elite club of numerical modelers to an institution within MIT that's also now renowned for its experimental prowess (and some dabbling in field work). It's been a privilege and a pleasure to work with all my lab mates, and I especially cherish the friendship of Peter Kang and Robin Zhao. The Parsons lab is a dynamic, diverse environment that combines the social aspects of shared space and mixed offices with the research advantages of interactions with a scientists from broad range of disciplines. The staff who do the thankless but critical support work made me feel like a part of a family, especially Sheila Frankel, Jim Long,

Vicki Murphy, Darlene Strother, Ruth Yiu, and Roberta Pizzinato.

The friends I've made there have become so close as to share addresses (Sean Clarke, Kelly Daumit, Mitul Luhar, Dan Prendergast, Jeff Rominger, Alison Takemura, and Robin Zhao) as well as soccer pitches and beer pitchers (John Macfarlane, Tony Parolari, Gaj Sivandran, Patricia Tcaciuc, Jessie Berta-Thompson, and Sarah Jane White, to name a few). My spirit has been nourished by countless outdoor adventures leading and learning with the MIT Outing Club, especially Jon Crowe and Michelle Moon, Nadine Müller-Dittmann, Anna de Regt and Erika Uyterhoeven. And it's been a thrill and an honor to work with the climate advocacy group Fossil Free MIT; I'm constantly awed by Ploy Achakulwisut, Patrick Brown, Pri Chatterjee, Stephanie Chin, Ioana Knopf, Jennifer Lauv, Nina Lytton, Daniel Mascoop, Jeremy Poindexter, Ben Rosen-Filardo, Geoffrey Supran, Tatjana Trebic, Eirik Trondsend, Britta Voss and all the rest. These various adventures have led to other meaningful friendships, with Craig Altemose, Ahmed Helal, Rouwenna Lamm, Justin Wright, and Elizabeth Youngblood among others I'm surely forgetting. Nora and Steve Esthimer, as well as Cynthia Esthimer and Lisa Whittemore, have allowed me to survive this past decade so far from my family.

Finally, I owe so much to my family for their love and encouragement from coast to coast. My parents, Nancy Haigwood and Carl Scandella, are my inspirations in science; my brothers Aiden and Nathan are role models in technology and expression; my Aunt Jan and Uncle Joe make Boston home away from home, and my Grandmothers Nan and Margo are the best cheerleaders anyone could hope for. I dedicate this thesis to my namesake grandfathers, Ben Scandella and Paul Haigwood, in the hopes that they're smiling down with pride.

This work was supported by the U.S. National Science Foundation (Award No. EAR-1045193), the U.S. Department of Energy (Grant No.'s DE-FC26-06NT43067, DE-AI26-05NT42496 and DE-FE0013999), the MIT Martin, Linden and Ippen fellowships, and the MIT UROP program.

This doctoral thesis has been examined by a Committee of the
Department of Civil and Environmental Engineering as follows:

Professor Harold F. Hemond .....
Chairman, Thesis Committee
Professor, Department of Civil and Environmental Engineering

Professor Ruben Juanes .....
Thesis Supervisor
Associate Professor,
Department of Civil and Environmental Engineering
and Department of Earth, Atmospheric and Planetary Sciences

Professor Charles Harvey .....
Member, Thesis Committee
Professor, Department of Civil and Environmental Engineering

Dr. Carolyn D. Ruppel .....
Member, Thesis Committee
Research Geophysicist, U.S. Geological Survey, and Visting Scientist,
MIT Department of Earth, Atmospheric and Planetary Sciences

Contents

Chapter 1

Introduction

1.1 Motivation

A major contemporary challenge is addressing global climate change. Global warming is driven primarily by increasing anthropogenic emissions of greenhouse gases (GHGs) like carbon dioxide (CO_2) and methane (CH_4) [*IPCC*, 2013], and limiting warming to the internationally-agreed target of 1.5–2° C requires implementing aggressive carbon mitigation strategies [*Pacala and Socolow*, 2004]. These strategies likely must include leaving a large majority of proven fossil fuel reserves untapped and rapidly transitioning to low-carbon energy generation [*Allen et al.*, 2009; *Meinshausen et al.*, 2009; *IPCC*, 2013; *McGlade and Ekins*, 2015; *Heede and Oreskes*, 2016]. However, further constraining the magnitude and time scale of the required decarbonization of the energy and transportation sectors, as well as refining the confidence and resolution of climate forecasts, requires better understanding of the climate response to emissions, including natural GHG sources and their climate feedbacks.

Methane is both an important fossil fuel resource and a potent greenhouse gas, capturing 28 times as much radiative energy as CO_2 per molecule over a century [*Ciais et al.*, 2013]. It is estimated that 50–60% of atmospheric methane emissions are anthropogenic, and this portion constitutes 20% of the radiative forcing from all long-lived greenhouse gases [*IPCC*, 2013; *Ciais et al.*, 2013]. The remaining emissions derive from natural sources, including wetlands, freshwaters, termites, and methane

hydrates. Accurately estimating the contribution from various methane emission sources is crucial to refining models of climate change because these sources each respond differently to shifts in climate.

Only recently have methane emissions from lakes begun to be included in methane budgets, partly in response to evidence that this source may be larger than originally estimated [*Bastviken et al.*, 2004; *Chen and Prinn*, 2006; *Walter et al.*, 2006; *Denman et al.*, 2007; *Bastviken et al.*, 2011; *Holgerson and Raymond*, 2016] and may constitute a positive feedback to climate change [*Walter et al.*, 2006; *van Huissteden et al.*, 2011; *Isaksen et al.*, 2011; *Greene et al.*, 2014; *Wik et al.*, 2014]. Significant uncertainty remains, as estimates suggest that freshwater methane emissions constitute between 2 and 31% of natural methane emissions [*Ciais et al.*, 2013; *Kirschke et al.*, 2013].

This thesis contributes to the effort of constraining methane emissions from lakes and other soft, submerged sediments in two ways. First, we develop methods development for measuring ebullitive gas fluxes over a wide range of spatial and temporal scales. The ability to measure ebullitive fluxes across a broad range of spatial and temporal scales allows estimation of the uncertainty associated with extrapolating measurements to larger scales. Second, we analyze the spatiotemporal variability to understand the relationship between distributed methane generation and the spatiotemporally-concentrated release of bubbles. The refinement of mechanistic models supports the eventual goal of integrated modeling of bubble generation, release and survival through the water column, which may contribute to future work to evaluate climate sensitivity of methane emissions from lakes.

Understanding the mechanisms controlling bubble growth and mobility in soft sediments is another primary motivation for this work, as the physics of multiphase flow in deformable porous media are complex and an active area of research. An original motivation was to understand how methane from dissociating hydrates might reach the seafloor through dynamic fractures [*Flemings et al.*, 2003; *Liu and Flemings*, 2007; *Scandella and Juanes*, 2011]. Vast quantities of methane are stored in subsea sediments as hydrate, and while some shallow hydrate deposits are vulnerable to dissociation forced by oceanic warming [*Archer*, 2007; *Archer et al.*, 2008; *Reagan and*

Moridis, 2007; *Westbrook et al.*, 2009; *Isaksen et al.*, 2011; *Ruppel*, 2011], the water depth of these appears sufficient to prevent the vast majority of liberated methane from reaching the atmosphere before dissolving [*Rehder et al.*, 2002; *Heeschen et al.*, 2003; *Leifer et al.*, 2006; *McGinnis et al.*, 2006; *Yapa et al.*, 2008; *Rehder et al.*, 2009].

1.2 Background

1.2.1 Methane measurement

Global methane emissions from lakes may be estimated using top-down (inverse) or bottom-up (upscaling or extrapolation) techniques. Inverse techniques may attribute the observed atmospheric accumulation to a limited number of sources, but lakes have been combined with wetlands in such work [*Chen and Prinn*, 2005, 2006] so are not attributed in top-down estimates [*Ciais et al.*, 2013]. Bottom-up techniques may be used to estimate emissions from industry, agriculture, and biomass burning by extrapolating well-understood chemical processes over well-constrained regions of application [*Denman et al.*, 2007]. Emissions from natural sources like lakes, however, are patchy in space and episodic in time, so extrapolation of measurements taken over short time periods or with little spatial coverage is likely to underestimate the strength of natural sources [*Wik et al.*, 2016].

Atmospheric methane emissions from lakes are often dominated by ebullition [*Martens and val Klump*, 1980; *Kuipphet and Martens*, 1982; *Crill et al.*, 1988; *Mattson and Likens*, 1990; *Keller and Stallard*, 1994; *Nakamura et al.*, 1999; *Bastviken et al.*, 2004; *Walter et al.*, 2006; *Delsontro et al.*, 2010; *Bastviken et al.*, 2011; *Maeck et al.*, 2013a] due to the buoyancy and high methane content of bubbles, which transport methane more efficiently than waters containing dissolved methane. Ebullitive emissions are particularly episodic and spatially heterogeneous, which complicates upscaling of flux estimates [*Greinert*, 2008; *Ostrovsky et al.*, 2008; *Greinert et al.*, 2010; *DelSontro et al.*, 2011; *Wik et al.*, 2011; *Maeck et al.*, 2013b; *Walter Anthony and Anthony*, 2013; *Wik et al.*, 2013; *Bayrakci et al.*, 2014; *DelSontro et al.*, 2015].

One of the objectives of the research presented here is to develop new methods for quantifying ebullition rates over multiple scales. A field-scale observation technique was developed by adapting a multibeam sonar to quantify spatially-resolved ebullitive fluxes over large area and long time period to further constrain upscaled fluxes. In addition, a laboratory-scale technique was developed to measure fluxes from incubated sediments with centimeter-scale resolution. The combination of these techniques allows us to relate behavior of individual bubble outlets with the spatiotemporal heterogeneity of methane venting at the scale of 20 m.

1.2.2 Bubble dissolution during rise

The magnitude of the atmospheric release depends on the strength of the methane source but is also mediated by the dissolution of bubbles during their rise through the water column. Methane is generated in anoxic lake sediments by microbially-mediated decomposition of organic matter [*Zinder*, 1993]. It may be transported to the lake surface via dissolved advection-diffusion, plant-mediated transport, and free-gas bubbling, called ebullition. From its origin in the sediments, some dissolved methane diffuses directly into the water column, but at high pore water concentrations it exsolves into gas bubbles that grow in and eventually escape from the sediments. During a bubble's rise to the surface, some portion of its methane dissolves into the surrounding water [*Rehder et al.*, 2002; *McGinnis et al.*, 2006; *Gong et al.*, 2009], and the dissolved methane may either be oxidized to carbon dioxide [*Rudd et al.*, 1974; *Nakamura et al.*, 1999] or be transported to the surface by turbulent mixing (often after a period of storage in the anoxic hypolimnion). The amount lost to dissolution depends on the initial size and release depth [*McGinnis et al.*, 2006], as well as the spatial and temporal concentration of gas release, because bubble plumes create upwelling currents and locally saturate the water with methane [*Leitch and Baines*, 1989; *Leifer et al.*, 2006; *Gong et al.*, 2009; *Wang et al.*, 2016]. Bubble dissolution may also depend on the mode of release because smaller bubbles dissolve faster [*McGinnis et al.*, 2006], and the bubble size distribution may depend on the rate of gas release [*Greinert and Nutzel*, 2004; *Vallebuona et al.*, 2005].

The dependence of bubble survival on such plume effects suggests that it is important to understand the the spatial and temporal concentration of ebullition in order to effectively model the relationship between methane generation in sediments and the atmospheric emissions. This dependence also presents a primary mechanism by which methane emissions from lakes could respond to climate change, for example via changes in precipitation patterns that influence hydrostatic triggering of ebullition [*Scandella et al.*, 2011; *Vallebuona et al.*, 2005]. A mechanistic model of methane release must then reproduce the spatiotemporal concentration of free-gas releases to correctly predict the fraction that escapes dissolution and oxidation and enters the atmosphere. Similarly, a measurement technique deployed at the sediment-water interface should have sufficient spatiotemporal resolution to detect the density of bubbles and predict their survival during rise to the air-water interface.

1.2.3 Episodicity of ebullition and hydrostatic pressure control

Ebullition is a highly episodic process, with temporal variations on the scale of seconds to seasons [*Boles et al.*, 2001; *Leifer and Boles*, 2005; *Varadharajan and Hemond*, 2012]. Over the scale of months, ebullition rates vary with the strength of the methane source, which often depends on seasonal cycles of organic matter deposition and sediment temperature [*Delsontro et al.*, 2010; *Wik et al.*, 2014; *Yvon-Durocher et al.*, 2014]. In the presence of a strong methane source, bubbles may reach a critical size to become mobilized on their own, but in many cases an external forcing operates more frequently and enables ebullition [*Maeck et al.*, 2013b]. Wind-driven shear has been observed to trigger ebullition [*Joyce and Jewell*, 2003], but the most commonly-observed effect is that drops in hydrostatic or atmospheric pressure trigger ebullition from methane-generating lake sediments [*Strayer and Tiedje*, 1978; *Yamamoto et al.*, 2009; *Scandella et al.*, 2011], peatlands [*Fechner-Levy and Hemond*, 1996; *Tokida et al.*, 2007] and marine sediments [*Martens and val Klump*, 1980; *Kuipphet and Martens*, 1982; *Chanton et al.*, 1989], possibly even in the presence of methane hydrates [*Torres et al.*, 2002].

In fine-grained sediments, the influence of hydrostatic pressure on ebullition may

be explained mechanistically as a response to changes in effective stress, $\sigma' = \sigma - P_f$, where P_f is the fluid pressure. For gas bubbles in shallow, water-saturated sediments with grains $\leq 10\mu$m in diameter, the sediment-water matrix acts as a continuum so that the fluid pressure controlling gas mobilization is the gas pressure, P_g [*Wheeler et al.*, 1990; *Sills et al.*, 1991; *Johnson et al.*, 2002; *Hamblin and Christiansen*, 2004; *Scandella*, 2010]. With falling hydrostatic pressure or rising gas pressure from exsolvation of dissolved methane, total stress σ is reduced, forcing gas-charged sediments into a more tensile effective stress state. The gas-filled cavities then dilate, at a critical stress that may be modeled assuming that the sediment-water matrix is elastic [*Algar et al.*, 2011a,b] or plastic [*Scandella et al.*, 2011]. The dilation may either occur fixed in place, leading to a saw-toothed pressure history with no long-term trend of rising pressure [*Johnson et al.*, 2002], or it may force open near-vertical conduits to the sediment's surface [*Boudreau et al.*, 2005; *Jain and Juanes*, 2009; *Scandella et al.*, 2011]. The fact that bubbles grow in a cornflake-shaped fracture pattern [*Boudreau et al.*, 2005], rather than as spherical bubbles, supports the idea that this mode of growth also allows for vertical mobility in soft sediments. Fracturing has also been implicated as a dominant mechanism for vertical gas transport in methane hydrate-bearing ocean sediments [*Flemings et al.*, 2003; *Liu and Flemings*, 2007; *Scandella and Juanes*, 2011].

To incorporate these observations in predicting the release of methane from lake sediments, we hypothesized that gas bubbles escape by dilating conduits to the sediment surface during periods of falling hydrostatic pressure as the gas bubbles overcome the confining stress from the sediments. This model of "breathing" dynamic conduits for gas release couples continuum-scale poromechanics theory with multiphase flow in porous media to predict the temporal signature of ebullition [*Scandella et al.*, 2011]. This 1-D model captures the accumulation of trapped gas in a vertical column of sediment and tracks the gas pressure and volume as a hydrostatic pressure forcing triggers plastic deformation of the sediment-water matrix surrounding gas cavities. When the effective stress reaches a depth-dependent tensile strength threshold, the gas forces open a conduit to the surface and escapes. The fundamental parameter of the model,

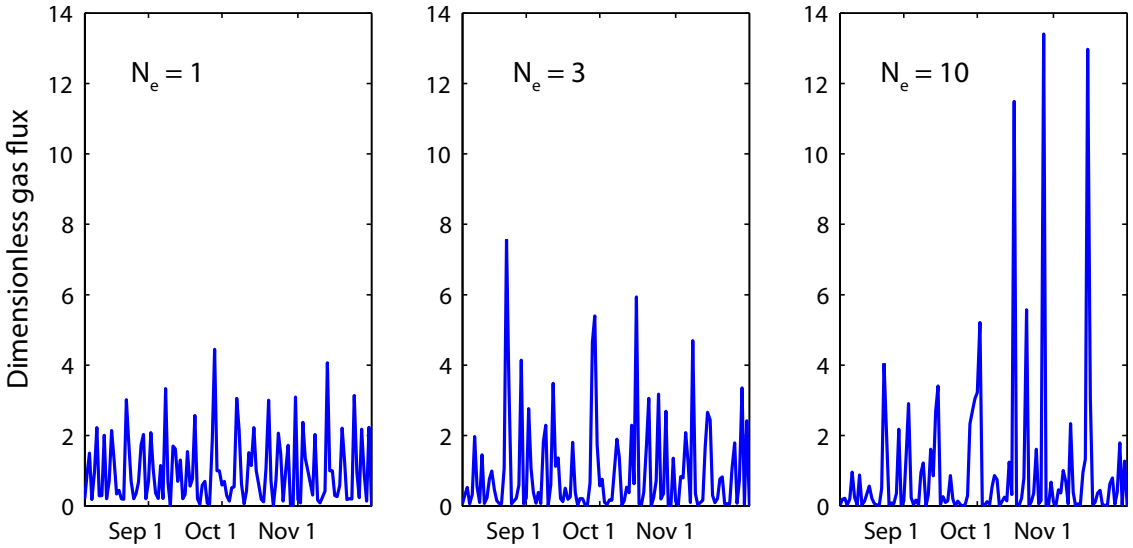

Figure 1-1: Sensitivity of dimensionless flux to ebullition number, for $N_e = 1, 3$, and 10, in response to the same measured hydrostatic signal shown in Fig. 1-2. The ebullition number is the dimensionless ratio of total sediment strength to hydrostatic variation forcing and is defined in equation (1.1). Larger values of N_e concentrate the gas flux into fewer, more powerful venting events. The best-fit value for the average of five traps from UML is $N_e \approx 5$.

called the ebullition number, N_e, reflects the balance between the vertical gradient in tensile strength of the mud and the characteristic magnitude of hydrostatic pressure changes:

$$N_e = \frac{h(d\sigma_T/dz + d\sigma_C/dz)}{\Delta P_h}, \tag{1.1}$$

where h is the model domain height, σ_T is the tensile strength and σ_C is the compressive strength of the sediment-water matrix, and ΔP_h is a characteristic hydrostatic pressure variation. Larger values of N_e require larger, rarer drops in hydrostatic pressure to release gas from the deepest sediments and thus drive more strongly episodic venting (Fig. 1-1). For a record of ebullition measured using floating bubble traps, the best-fit value was found to be $N_e \approx 5$ (Fig. 1-2) [*Scandella et al.*, 2011].

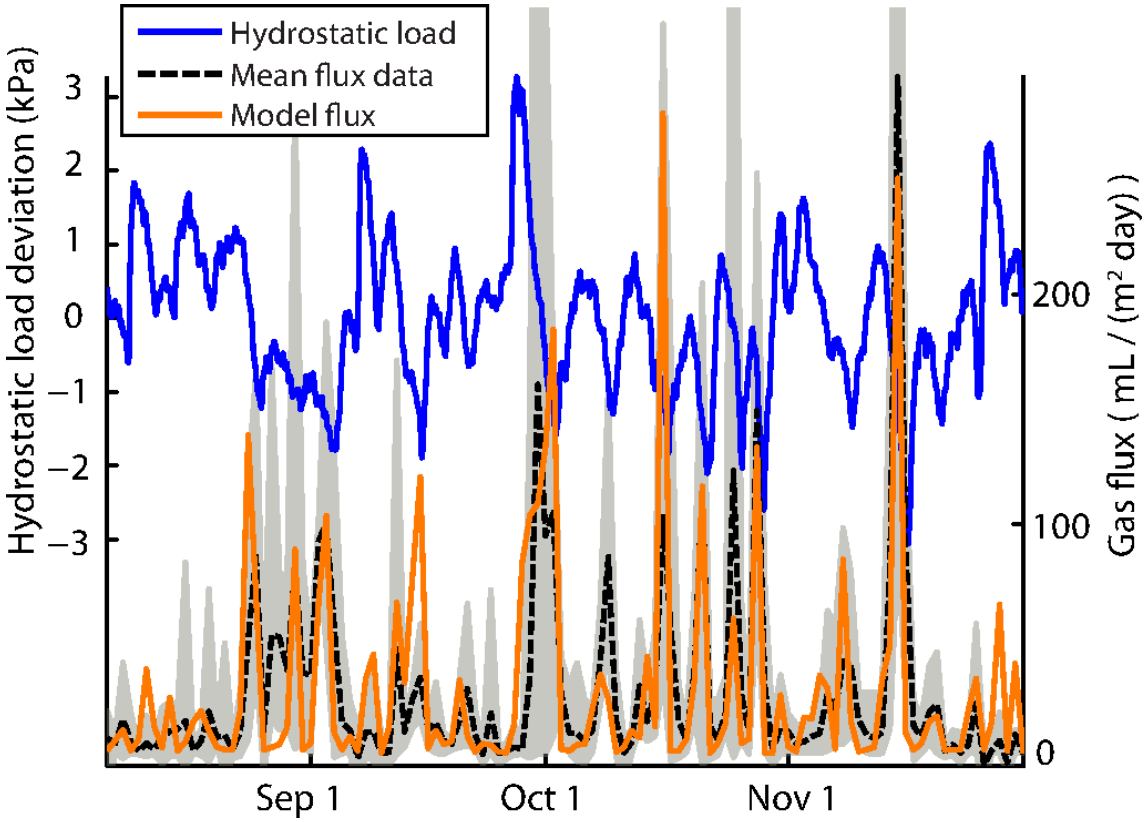

Figure 1-2: Best fit of model gas ebullition fluxes to data from Upper Mystic Lake [*Scandella et al.*, 2011]. The left axis and solid blue line show a time series of the hydrostatic load forcing, and the right axis shows the methane fluxes from the mean bubble trap data (black, dashed) and model (orange, solid). The gray shaded area indicates the range of flux values from the five traps; note that in four instances the range extends above the limit of the vertical axis up to a value of ~700 mL/m^2/day. The fluxes are binned daily, and the cumulative model release is constrained to match the data. The calibrated value of the ebullition number, $N_e \approx 5$, reflects that a hydrostatic pressure drop of about 5 standard deviations (5 kPa in this case) is required to evacuate the methane from the entire active generation depth, h (equation (3)). The single-parameter model accurately predicts the timing of large flux events and usually their magnitude, as well.

1.2.4 Spatial heterogeneity of methanogenesis and lateral transport

Ebullition has been observed to be spatially heterogeneous from the scale of centimeters to kilometers, and understanding the heterogeneity is critical to developing a conceptual model of the system, extrapolating measurements in space and estimating atmospheric emissions after bubble dissolution during rise. At the sub-meter scale, individual outlets show persistent activity [*Skarke et al.*, 2014]. At the meter scale, multi-day hydroacoustic observations in the estuarine Black Sea show discrete seeps clusters of diameter 1–5 m and spaced an average distance of 11 m apart [*Greinert*, 2008]. Lower-resolution hydroacoustic observations in the nearby Sea of Marama detected 10-m clusters of multi-day persistent venting that were spaced $\approx 10 - 50$ m apart [*Bayrakci et al.*, 2014]. In each of these two estuarine studies, the was inferred to be supplied from a deeper source and temporarily trapped beneath layers of low-permeability sediments. In arctic lakes, bubbles trapped in surface ice may be modeled as a Thomas clustering pattern, where clusters are dispersed completely randomly in space with average distance of 2–10 m and characteristic spreading distance of 0.8 m [*Walter Anthony and Anthony*, 2013]. In marine settings, persistent seeps have been observed with spacing $\approx 5 - 10$ m [*Wang et al.*, 2016]. At larger scales, ebullition rates vary with 10–100 m bathymetric and depositional features [*DelSontro et al.*, 2011; *Maeck et al.*, 2013a; *Walter Anthony and Anthony*, 2013; *DelSontro et al.*, 2015], and discrete plumes are detectable in marine settings even with hydroacoustic methods with typical resolution ≥ 10 m [*Westbrook et al.*, 2009; *Skarke et al.*, 2014; *Wang et al.*, 2016].

Persistent heterogeneity in ebullition may be driven by laterally-variable methane sources, which may be attributed to heterogeneous geology [*Hornbach et al.*, 2004; *Walter Anthony et al.*, 2012; *Skarke et al.*, 2014], sediment deposition patterns [*Bussmann et al.*, 2011; *DelSontro et al.*, 2011; *Maeck et al.*, 2013a; *Walter Anthony and Anthony*, 2013; *DelSontro et al.*, 2015], temperature [*Liikanen et al.*, 2002; *Yvon-Durocher et al.*, 2014] or oxygen availability [*Kelly and Chynoweth*, 1981; *Liikanen*

et al., 2002]. Groundwater flow may influence sediment deposition patterns or flush dissolved methane out of porewater before it reaches saturation and generates bubbles, and these could affect the spatial distribution of bubble generation. In addition, the close-proximity microbial consortia that link fermentation and methanogenesis occur in patches, and these patches may further concentrate generation [*Hoehler et al.*, 1994].

However, spatial variability in ebullition may also arise from transport-driven processes that play a role even in compositionally homogeneous sediments [*Kong et al.*, 2010]. Two general classes of transport processes could give rise to persistent heterogeneity in gas fluxes: dissolved methane transport towards bubble nucleation sites, and free-gas transport through sub-vertical conduits. Both processes are supported by the preferential re-occupation of existing bubble paths, which will be encouraged by a drop in tensile strength following bubble passage. However, the lateral distance over which each operates, and the timescale over which the re-use is expected to persist, depend on different factors, described below.

Dissolved methane transport within the pore water of UML sediments is expected to be driven primarily by diffusion, given the low permeability of the fine-grained sediments. Growth of bubbles is supported by diffusive methane transport because the inverse relationship between equilibrium capillary pressure and bubble radius makes tiny bubbles unstable and allows the pore water to become supersaturated with methane. The resulting concentration gradients drive diffusion towards existing bubbles [*Gardiner et al.*, 2003; *Algar and Boudreau*, 2009]. After a bubble escapes, the concentration will be relatively low in the vicinity of the vacated gas void, so in principle bubbles should not re-grow in the same location (assuming an excess of nucleation sites). However, if the tensile strength of the vacated void is significantly lower than that of the surrounding sediments, the energetic barrier to forming a new bubble there will also be lower, and a new bubble may begin to grow in the same place once the pore water concentration has rebounded sufficiently. The tendency to re-use nucleation sites (their persistence) should be supported by strong drops in σ_T and slow recovery compared with the timescale of diffusion over the spacing of trapped bubbles.

The spacing in turn will increase with slow rates of gas generation compared with the frequency of gas release (perhaps enabled by an external forcing), larger drops in σ_T compared with the energy (pressure) associated with supersaturation, which will depend on the methane solubility. For the diffusion coefficient of of methane in water (1.88×10^{-5} cm^2/s [*Witherspoon and Saraf*, 1965]), the length scale over which diffusion is expected to operate given the timescale for methane generation of ~ 1 month is $\sim 5 - 7$ cm, depending on the porosity (≈ 0.9) and tortuosity of the sediments [*Huttunen et al.*, 2006; *Varadharajan*, 2009].

Lateral free-gas transport is enabled by bubble migration through a network of sub-vertical conduits that we expect fan out in a roughly conical shape beneath each major outlet. Previous mechanistic modeling of bubble mobilization in the framework of linear elastic fracture mechanics [*Gardiner et al.*, 2003; *Boudreau et al.*, 2005; *Algar et al.*, 2011a,b] led to the speculation that bubbles tend to form in and follow the rise paths of previously-released bubbles due to partial healing of the fracture toughness (K_{1C}) of sediments [*Algar et al.*, 2011b]. We approach the mechanics from the perspective of plastic deformation, where the parameter setting the limit on effective stress under tension is the tensile strength, σ_T [*Scandella et al.*, 2011]. The mechanism of tensile strength reduction should support re-use of existing bubble conduits, diverting bubbles laterally to grow and rise towards existing outlets. Sub-vertical bubble rise has been observed in laboratory experiments in fine, uncompacted glass beads [*Kong et al.*, 2009] and gelatin [*Boudreau et al.*, 2005]. The re-use of conduits should be supported by large drops in σ_T relative to its absolute magnitude, as well as by the re-use of bubble nucleation sites.

While the spacing of outlets is expected to be related to the magnitude of the drop in tensile strength, the persistence of drops is expected to depend on the rate of recovery of tensile strength. We hypothesize that σ_T is temporarily reduced by bubble passage and recovers slowly with time until the next release. Previous research on soft, fine-grained sediments has revealed recovery of the yield stress over the scale of months [*Merckelbach et al.*, 2002]. Mechanistically, this strengthening is explained as a result of decreasing distances between particles of neighboring aggregates during

compaction, causing an increase in strength of van der Waals forces and hydrogen bonds [*Merckelbach*, 2000; *Merckelbach et al.*, 2002; *Holtz and Kovacs*, 2010]. Persistence of conduits is expected to depend on the timescales for recovery of σ_T, methane generation, and potentially an external forcing frequency. Both faster methane generation or more frequent external triggering should promote more frequent ebullition, and the faster of these two processes may be compared with the timescale for recovery of σ_T to determine whether conduits will typically heal or be re-opened frequently enough to persist.

In summary, the conceptual model motivating our work is that bubble passage through sediments supports subsequent re-use of a gas conduit by temporarily reducing the sediment cohesion. If pre-existing conduits are significantly more favorable than undisturbed sediments, gas will be collected towards an outlet from a larger area, and the major outlets will show more distant spacing. We hypothesized that major outlets would be spaced at least 5–10 cm apart and substantially persist over the scale of months due to slow healing of tensile strength.

1.3 Research objectives

The objectives of this research project are:

1. Develop a field-scale technique for quantifying spatially-resolved ebullition fluxes over a wide area and long deployment period with spatial resolution ≤ 0.5 m [*Scandella et al.*, 2016].

2. Develop a laboratory-scale technique to quantify ebullitive fluxes with spatial resolution of ≈ 1 cm.

3. Investigate the role of hydrostatic pressure in controlling ebullition, especially compared with a conduit dilation model of methane venting from lake sediments [*Scandella et al.*, 2011].

4. Refine the mechanistic, conceptual model of methane ebullition linking growth and mobility of individual bubbles with field-scale heterogeneity in ebullition.

5. Determine the degree of re-use of outlets, their persistence and spacing, and if possible, infer what transport processes give rise to such behavior.

Meeting these research objectives would provide important advances in both research methodologies and scientific understanding of natural methane fluxes.

Chapter 2

A multibeam sonar lander to quantify ebullitive gas fluxes

2.1 Introduction

Estimating the magnitude of gas flux from submerged sediments is challenging because ebullition events are episodic and spatially-localized. Ebullitive fluxes are sometimes measured using bubble traps deployed at discrete locations over an extended time period, but capturing hotspot ebullition or the episodicity of venting events can be challenging with this approach [*Walter et al.*, 2006; *Varadharajan and Hemond*, 2012; *Maeck et al.*, 2013b; *Walter Anthony and Anthony*, 2013; *Wik et al.*, 2013]. Hydroacoustic surveys from ships [*Ostrovsky et al.*, 2008; *Greinert et al.*, 2010; *DelSontro et al.*, 2011, 2015; *Skarke et al.*, 2014; *Weber et al.*, 2014] cover large areas but only at discrete times, and therefore cannot be used for continuously quantifying fluxes. Short- and long-term seafloor deployments of hydroacoustic sensors [*Greinert*, 2008; *Schneider von Deimling et al.*, 2011; *Bayrakci et al.*, 2014; *Wang et al.*, 2016] can detect ebullitive events at specific locations but require careful calibration to infer spatially-resolved fluxes. Here we extend the hydroacoustic approach to acquire long-term, high-resolution methane emission records from a lake bottom.

A horizontally-oriented multibeam sonar is capable of detecting the timing and location of bubbles rising through a wide fan (120–140°). Multibeam sonars are

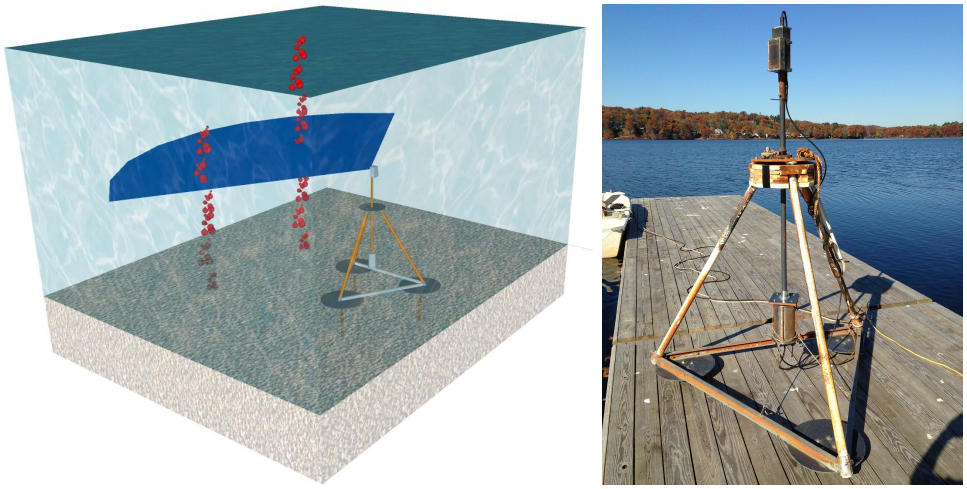

Figure 2-1: Left: Diagram showing streams of bubbles (red) rising through the horizontally-oriented multibeam sonar fan (blue, not to scale). Right: Photo of the deployment tripod before redeployment.

distinguished from single beam and split-beam sonars in their ability to resolve the distance *and direction* of multiple targets simultaneously using a phased array of transducers. While methods have been developed for estimating fluxes from single-beam sonars [*Nikolovska et al.*, 2008; *Ostrovsky et al.*, 2008; *Muyakshin and Sauter*, 2010; *Weber et al.*, 2014; *Veloso et al.*, 2015], such as those typically mounted on research vessels, the theory for estimating fluxes from multibeam sonars has not. The first published work claiming to estimate fluxes from a multibeam sonar presented a calibration that was unrelated to the data being analyzed, and the flow rate magnitudes were assigned by a human, "based on experience" [*Shakhova et al.*, 2014]. In this chapter we describe the theory for and implementation of the calibration of a horizontally-oriented Imagenex 837B Delta T multibeam profiling sonar to estimate gas flow rates and fluxes, and we present the design and deployment methods for a lake-bottom lander that permits acquisition of long-term, high-resolution methane emission records over a fixed, wide area (Fig. 2-1) [*Scandella et al.*, 2016].

2.2 Ebullitive flux estimation with a horizontally-oriented multibeam sonar

2.2.1 Backscatter measurement using the Imagenex 837B

The physical property of sonar targets that can be measured using sonar is the backscatter cross-section, the product of the cross-sectional area of the target with a dimensionless reflectivity. The theory presented below allows estimation of gas flow rates from the backscatter cross-section values reported by a multibeam sonar so should be applicable independent of a particular sonar unit or model. However, the the Imagenex 837B Delta T multibeam profiling sonar used in this study does not measure backscatter cross-section directly, so we first present the method used to calibrate it for that purpose.

The pressure wave amplitude of the sound received by a sonar unit is that of the source, diminished by spherical spreading and attenuation, and increased by the magnitude of the target causing the reflection. The received amplitude P_{rec} after travel to and from targets with backscatter cross-section σ_{bs} at distance R, with spherical spreading, is:

$$\left(\frac{P_{rec}}{P_0}\right)^2 = \left(\frac{P_{src}(\theta)}{P_0}\right)^2 \left(\frac{R}{R_0}\right)^{-4} 10^{-\frac{2\alpha R}{10}} \frac{\sigma_{bs}}{R_0^2}, \tag{2.1}$$

where $P_{src}(\theta)$ is the directionally-dependent amplitude of the source signal, P_0 and R_0 are reference pressure and length values, and α is a coefficient of acoustic attenuation in the water. The use of reference values facilitates handling the sonar equation in logarithmic form, though for the sake of clarity we will use SI units. Also note that σ is the variable traditionally used to represent both acoustic backscatter and mechanical stress; we use subscripts or superscripts for all versions of the variable to keep them distinct.

The Imagenex DeltaT reports an amplitude that is proportional to the received pressure in each pixel (beam for direction and sample for distance from the sonar

head):

$$(a_{\Delta T})^2 = \left(k_a \frac{P_{rec}(\theta)}{P_0}\right)^2 G^2 \left(\frac{R}{R_0}\right)^2 10^{\frac{2\alpha R}{10}}, \tag{2.2}$$

$$G = 10^{\frac{G_s}{20}} \left(\frac{G_d}{100}\right), \tag{2.3}$$

where k_a is an unknown proportionality constant and G is the user-defined gain on the signal. The user-defined gain G depends on 2 parameters, the hardware "StartGain" (G_s) and the software "DisplayGain" (G_d) that scales the data into the 8-bit dynamic range. The power of 2 in R/R_0 compensates for part of the geometric spreading and is applied as a time-varying gain (TVG) to the incoming signal. It is appropriate for quantifying the reflectivity of surface targets that extend past the incident area of the sonar pulse (which is proportional to R^2), as is the case for the sediment surface in a bathymetric survey. Since k_a is Imagenex proprietary information, we define $a_{rec} = k_a P_{rec}/P_0$ and $a_{src}(\theta) = k_a P_{src}(\theta)/P_0$. This way, Equations (2.1) and (2.2) can each be solved for a_{rec}:

$$a_{rec}^2 = a_{src}^2 \left(\frac{R}{R_0}\right)^{-4} 10^{\frac{-2\alpha R}{10}} \frac{\sigma_{bs}}{R_0^2} \tag{2.4}$$

$$= \left(\frac{a_{\Delta T}}{G}\right)^2 \left(\frac{R}{R_0}\right)^{-2} 10^{\frac{-2\alpha R}{10}}. \tag{2.5}$$

Setting these two equal and solving for σ_{bs} yields:

$$\sigma_{bs} = \left(\frac{a_{\Delta T} R}{a_{src}(\theta) G}\right)^2. \tag{2.6}$$

For the data reported here, $G_s = 20$ dB and $G_d = 3$ so that $G = 0.3$. The source amplitude $a_{src}(\theta)$ has two components: a base magnitude a_0 and directional dependence, or horizontal beam pattern, $B_h(\theta)$:

$$a_{src}(\theta) = a_0 B_h(\theta). \tag{2.7}$$

The horizontal beam pattern was estimated in a two-step process described below.

The base magnitude a_0 was then estimated using a standard 38.1 mm diameter tungsten-carbide calibration sphere in situ ($\sigma_{bs} = 1.19 \times 10^{-4}$ m^2 for $f = 260$ kHz). The sphere was raised and lowered through the sonar fan in a variety of locations (θ and R) to get a record of the maximum $a_{\Delta T}$. Equations (2.6) and (2.7) were then combined to solve for a_0, yielding estimates of $a_0 = (3.2 \pm 0.7) \times 10^5$ for the unit used in this study.

2.2.2 Theory: backscatter vs. flux for a multibeam sonar

Sonar is an effective tool for detecting gas bubbles in water because the large contrast in acoustic impedance (product of density and speed of sound) causes pressure waves—when emitted at an appropriate frequency—to reflect strongly off the surface of the bubble. However, estimating the volume within gas bubbles that are detected by sonar is challenging because the magnitude of the sonar signal (the backscatter cross-section, σ_{bs}), is roughly proportional to the total cross-sectional area of bubbles facing the sonar, not their volume. If the distribution of bubble sizes varies little compared with the number of bubbles insonified, the backscatter becomes proportional to the total bubble volume, and therefore the flux [*Muyakshin and Sauter*, 2010]. This "inverse" method has been demonstrated at marine ebullition sites using downward-looking, single-beam and split-beam echosounders used during ship-based surveys [*Muyakshin and Sauter*, 2010; *Weber et al.*, 2014; *Veloso et al.*, 2015]. Here we develop an inverse method for estimating gas fluxes using a fixed-location, horizontally-oriented, profiling multibeam sonar.

While multibeam sonars are typically used with the fan oriented vertically for bathymetric profiling, we used the fan in a horizontal orientation to detect bubbles as they rose through it (Fig. 2-1). A profiling multibeam sonar projects a pulse that is roughly planar and fan-shaped, and the received signal is processed to measure σ_{bs} as a function of both the distance from the sonar head (range) and the direction. A bubble stream rising through the sonar fan contributes to σ_{bs} in a spatially-compact collection of connected pixels. Each pixel, in turn, may insonify multiple bubbles because the fan-shaped pulse has a slight vertical extent (2.2° half-power).

The backscattering measured by the sonar may be expressed as an integral over the radius of bubbles and over the vertical dimension, z:

$$\sigma_{bs} = \int\int N(r,z)\sigma_{bs}(r)B_v^2(z)drdz, \tag{2.8}$$

where $N(r,z)$ is the number of bubbles per radial and vertical unit distance, and $\sigma_{bs}(r)$ is the backscatter from a single bubble of radius r, which may modeled assuming a spherical bubble [*Anderson*, 1950]. B_v is the vertical beam pattern that reflects the sensitivity of the multibeam sonar in the alongship direction.

While the vertical position of individual bubbles within the sonar fan cannot be detected by the sonar, the impact of the vertical beam pattern can be accounted for by averaging measurements over a timescale equivalent to the rise time through the sonar fan (0.2-4 s). Over this timescale, the elevation dependence of N may be neglected, so that the integrals may be separated:

$$\overline{\sigma}_{bs} \approx \int B_v^2(z)dz \int N(r)\sigma_{bs}(r)dr. \tag{2.9}$$

Because the profiling sonar has a relatively tight beam pattern (small ϕ), the relationship $z = R\tan(\phi)$ may be approximated as $z \approx R\phi$. Applying this change of variables:

$$\overline{\sigma}_{bs} \approx R\phi_e \int N(r)\sigma_{bs}(r)dr, \tag{2.10}$$

$$\phi_e = \int B_v^2(\phi)d\phi, \tag{2.11}$$

where ϕ_e is the equivalent beam angle: the angle equivalent to the vertical extent of the fan if the sensor had no sensitivity dropoff ($B_v = 1$). The vertical beam pattern $B_v^2(\phi)$ was measured for the Imagenex 837B during calibration to be Gaussian with half-power angle $\phi_0 = 2.2°$ (Fig. 2-2):

$$B_v^2(\phi) \approx \exp\left[-\ln(2)\left(\frac{\phi}{\phi_0/2}\right)^2\right], \tag{2.12}$$

and, thus, the equivalent beam angle takes the form

$$\phi_e \approx \frac{\phi_0}{2}\sqrt{\frac{\pi}{\ln(2)}}. \tag{2.13}$$

where the second equation is the solution of Equations (2.11) and (2.12).

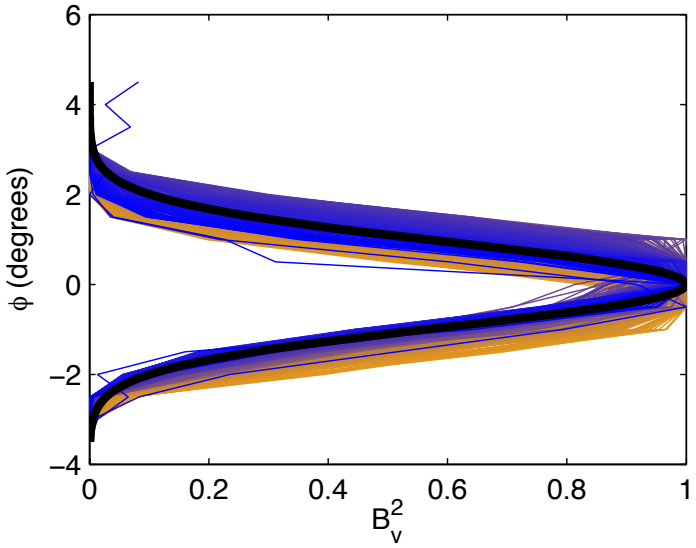

Figure 2-2: Vertical beam pattern, $B_v(\phi)$, for the Imagenex 837B, as measured in the ocean engineering tank at the UNH (colored lines), and with a Gaussian best-fit curve (black), with half-power angle $\phi_0 = 2.2°$ [Eq. (2.12)]. Colors on lines indicate the horizontal (athwartship) beam measured, from $-60°$ (orange) to $60°$ (blue).

The volumetric gas flow rate through a pixel may similarly be expressed as an integral over the bubble radius:

$$Q = \int N(r)V(r)u_{rise}(r)dr, \tag{2.14}$$

where u_{rise} is the vertical rise velocity of the bubble, which may be modeled [*Ostrovsky et al.*, 2008], and $V(r) = (4/3)\pi r^3$ is the volume of an assumed-spherical bubble. By combining Equations (2.10) and (2.14), we obtain:

$$Q \approx \frac{\overline{\sigma}_{bs}}{R\phi_e}\frac{\int N(r)V(r)u_{rise}(r)dr}{\int N(r)\sigma_{bs}(r)dr}. \tag{2.15}$$

When the bubble size distribution (BSD), $f(r)$, is relatively constant, the number of

bubbles may be expressed as the product of the overall bubble density N_0 and the BSD, $N(r) = N_0 f(r)$. Applying this approximation allows N_0 to cancel from the numerator and denominator, and a combined expression for the flow rate is:

$$Q \approx K\left(\frac{\overline{\sigma}_{bs}}{R}\right), \tag{2.16}$$

$$K = \frac{\int f(r)V(r)u_{rise}(r)dr}{\phi_e \int f(r)\sigma_{bs}(r)dr}. \tag{2.17}$$

The flow rate estimated by Eq. (2.16) is subject to temporal smoothing because $\overline{\sigma}_{bs}$ is measured over a timescale at least equivalent to the time a bubble takes to traverse the sonar fan. This smoothing does not impact estimates of the total volume because the smoothed flow rate is integrated over time. This equation permits theoretical calculation of the coefficient K for an arbitrary BSD. This may be compared with the coefficients used for the inverse method in single-beam and split-beam sonar units [*Muyakshin and Sauter*, 2010; *Veloso et al.*, 2015].

Due to the high spatial resolution of the Imagenex 837B at the 20 m maximum range setting, bubble streams typically activate a cluster of 2-20 connected pixels, depending on the flow rate and distance from the sonar head. Of interest for our analysis is the total flow rate from a bubble stream, so Eq. (2.16) was applied to the sum of connected pixels that were active above a threshold of minimum flow rate:

$$Q_{tot} \approx K' \sum \left(\frac{\overline{\sigma}_{bs}}{R}\right), \tag{2.18}$$

$$K' = \frac{K}{f_{overlap}}, \tag{2.19}$$

where $f_{overlap}$ is the degree of overlap between neighboring pixels and is measured empirically. As an alternative, one could analyze the maximum backscatter value from within the cluster of pixels, but such a measurement would be more sensitive to the horizontal beam pattern within each beam (Fig. 2-7) and would neglect the contribution of bubble streams active simultaneously and within a few pixel widths.

Fixed bubble size distribution assumption

The approximation of a constant bubble size distribution (BSD) is most appropriate when the bubble plume is dense enough that the variations in the backscatter derive primarily from changes in the density of bubbles rather than their size. The ebullition events in UML are typically sparse, with only 1-20 bubbles per event, so that variations in the instantaneous backscatter may be primarily due to changes in bubble size and vertical position of the bubbles within the sonar fan. However, the use of 5-second temporal averaging to estimate the flow rate both accounts for the impact of the vertical beam pattern and increases the number of bubbles sampled for a given measurement, making the approximation of constant BSD more appropriate.

Some single-beam and split-beam sonar units independently report both the backscatter cross-section and the distribution of backscattering values from individual bubbles [*Ostrovsky et al.*, 2008; *DelSontro et al.*, 2015] that allow simultaneous estimation of the BSD and flow rate. However, such detail is typically not available from multibeam sonar units like the one used in our study. The sheer amount of data that would be generated by such a system presents and obstacle, but with growing computer power and storage this barrier may be surmounted in the future.

Multiple scatter reflections

When multiple nearby bubbles are insonified, the received sonar signal amplitude may be composed of not only the direct backscatter from each of the bubbles, but also the multiple-scatter signal that bounces between multiple bubbles. The relative intensity of a multi-scatter signal depends on the scattering from each target and the distance between them. To estimate the importance of this effect, consider two identical bubbles separated from each other by distance D and from the sonar head by range R. The scattering from a gas bubble may be up to 10 times that of the backscattering for $kr < 10$, depending on their orientation relative to the sonar [*Medwin and Clay*,

1998], so the scattering cross-section from the multi-scatter signal (σ_{multi}) is:

$$\sigma_{multi} \leq \frac{10\sigma_{bs}^2}{4\pi D^2}, \tag{2.20}$$

$$\overline{\sigma}_{ms} = \frac{\sigma_{multi}}{\sigma_{bs}} \leq \frac{10\gamma}{4}\left(\frac{r}{D}\right)^2, \tag{2.21}$$

where γ is the scattering normalized by the cross-sectional area. For bubbles in the size range of $a \in [0.5, 5]$ mm, $\gamma \approx 0.1$ [*Medwin and Clay*, 1998] so that for inter-bubble distance $D > 5$ mm, $\overline{\sigma}_{ms} \leq 10^{-2}$. If $Q = Vu/D$, where V is the bubble volume for bubbles rising in a homogeneous vertical stream, then we can define $\overline{\sigma}_{ms}$ as a function of Q and r:

$$D = \frac{Vu}{Q} = \frac{4ur^3}{3Q}, \tag{2.22}$$

$$\overline{\sigma}_{ms} \leq \frac{5\gamma}{2}\left(\frac{3Q}{4\pi u r^2}\right)^2. \tag{2.23}$$

This allows us to define iso-lines of $\overline{\sigma}_{ms}$ in the space of Q and r, a lower bound for Q required to make multi-scatter signals detectible at a given tolerance $\overline{\sigma}_{ms}$,

$$Q \geq \sqrt{\frac{2\pi\overline{\sigma}_{ms}}{5\gamma}}\frac{4\pi u r^2}{3}. \tag{2.24}$$

Thus, the flow rate threshold at a given tolerance for multi-scatter signals increases with the square of the bubble radius, and high-flow bubble streams composed of small bubbles are the most conducive to multi-scatter (Fig. 2-3). For the range of bubble sizes and flow rates predominantly observed in the lake, multi-scatter signals are expected to contribute typically less than 1% of the total sonar signal and only rarely up to 10%, so their influence is neglected.

2.2.3 Calibration experiment

The sonar was calibrated to estimate the volumetric flow rate of bubble streams rising through its observation area of ≈330 m^2. The calibration was performed on a unit of the same model in the Ocean Engineering tank at UNH by injecting bubbles at a

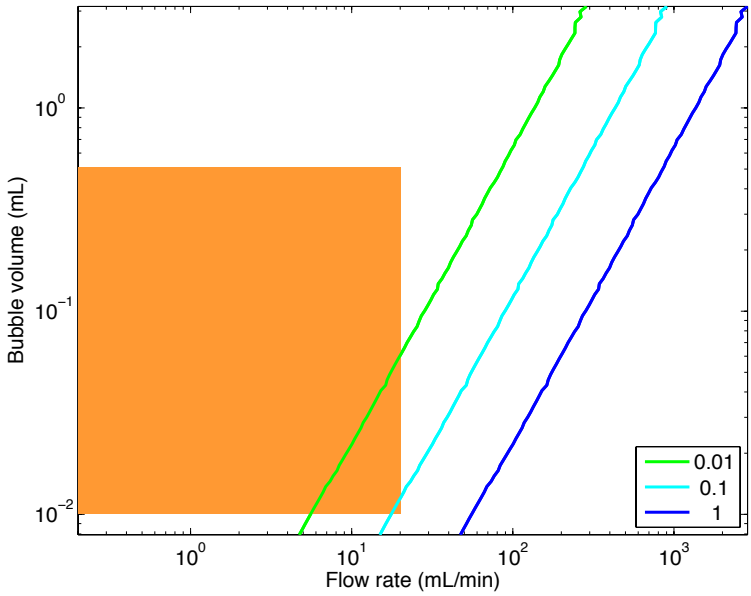

Figure 2-3: Normalized multiple-scatter reflection magnitude $\overline{\sigma}_{ms}$ (isolines in legend) as a function of flow rate and bubble volume. The shaded orange region shows the range of bubble sizes and flow rates expected to be encountered, from the BSD [*Delwiche et al.*, 2015] and from the limits on mean flow rate for distinguishing bubbles from anchor lines. In most cases we expect multi-scatter reflections to contribute less than 1% of the signal, and only above 10% for the cases of highest flow rates with smallest bubbles. These estimates are conservative because of the assumption of optimal arrangement of bubbles relative to the sonar to yield maximum scattering [*Medwin and Clay*, 1998].

constant flow rate and bubble size distribution from beneath the sonar fan. The bubble sizes were measured independently using a camera in a waterproof housing, and the rate of bubble release was monitored with a passive hydrophone. The spatially-summed, time-averaged backscatter $\overline{\sigma}_{bs}$ measured by the sonar scaled linearly with the flow rate Q at a given bubble size (Equation (2.18) and Fig. 2-4). The calibration was carried out with bubbles of 3 different size classes ranging from 1.1–2.5 mm in radius.

The dependence on flow rate and bubble size matched predictions from an analytical model of the expected sonar response to a constant bubble stream rising through a horizontally-oriented multibeam sonar. The expected response from a bubble stream with a wide but constant bubble size distribution was calculated by adapting a method that was developed for single and split-beam sonar [*Muyakshin and Sauter*, 2010;

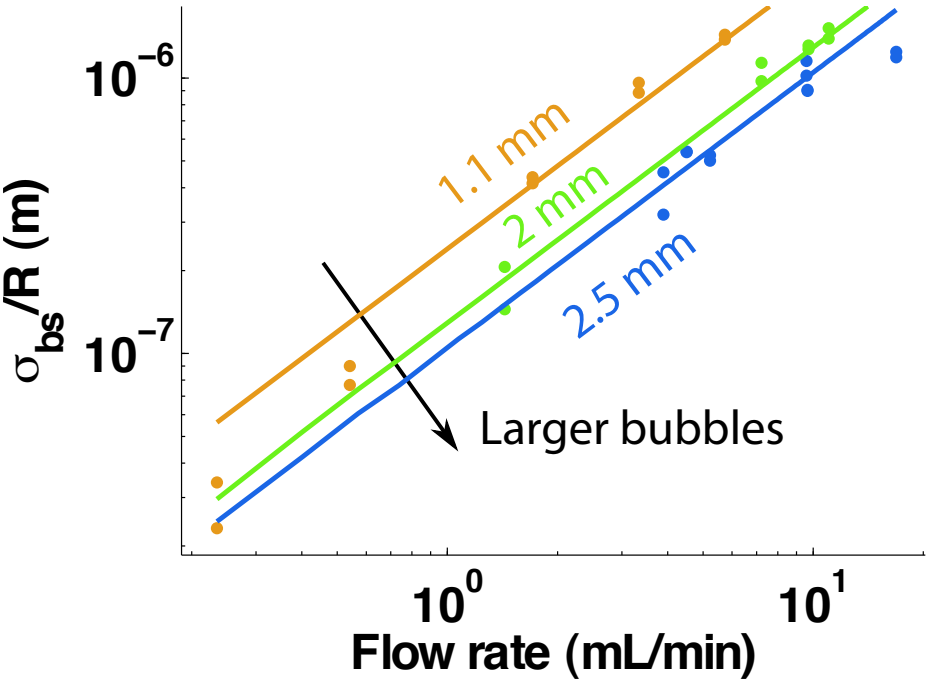

Figure 2-4: Calibration curves over 2 orders of magnitude in gas flow rate and for 3 different bubble size classes. Data points represent the time-averaged sonar response to streams of a given flowrate, and lines indicate modeled responses for each bubble class (radius in mm).

Veloso et al., 2015], assuming a constant bubble size distribution measured in UML with an optical bubble sizer [*Delwiche et al.*, 2015] and assuming that plumes are too sparse to be influenced significantly by multiple scatter reflections. The modeled calibration coefficient was calculated for each of the 3 bubble size classes, and the modeled response best fit the data when $f_{overlap} = 1.4$ (Equation (2.19)).

Bubble image analysis

In addition to passive acoustic methods, bubble photographs were used to estimate the bubble sizes. The observation area was back lit with a powerful underwater light behind a 1/4-inch translucent plastic diffuser panel. Individual images were taken every second for at least 1 minute during the calibration tests, and the bubbles were identified and sized automatically using MATLAB. Bubbles were identified by a best-fit ellipse on a group of nearby pixels that correspond to edges in intensity in the red channel. Edge pixels were identified using the Canny method, which identifies pixels

in a gradient with magnitude above a given threshold. We used lower and upper thresholds of 0.0002 and 0.005, respectively, and a Gaussian filter with width of 1 pixel. Edge pixels were grouped with their neighbors using the density-based scan algorithm [*Daszykowski et al.*, 2001]. For these pixel groups, best-fit ellipses were identified using MATLAB's `regionprops` function, and the radii were shrunk by 20% to match the images [*Thomanek et al.*, 2010] (Fig. 2.2.3). Bubble volumes were estimated assuming that the bubbles were oblate spheroids so that $V = \frac{4}{3}\pi r_{\max}^2 r_{\min}$, where $r_{\max}$ and $r_{\min}$ are the respective major and minor axes of an ellipse. Bubbles smaller than 0.5 mm in radius were rejected from the automated processing algorithm, to avoid spuriously treating image noise as bubbles.

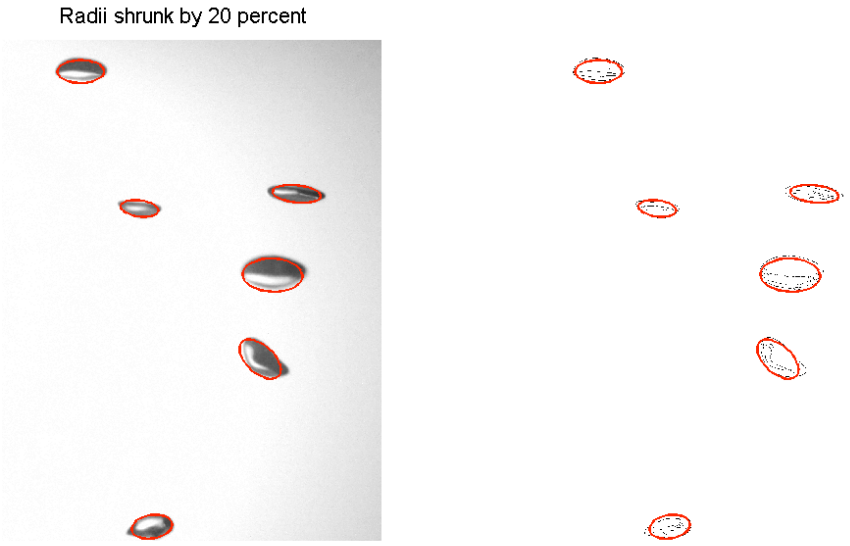

Figure 2-5: Automatic bubble identification from calibration images. Left: grayscale image with identified ellipses superimposed in red. Right: edge pixels with the same ellipses. In both cases, the radii are reduced by 20% from those identified using MATLAB's `regionprops` tool.

2.2.4 Spatial and temporal resolution

The sonar data were acquired using an Imagenex 837B multibeam profiling sonar, which detects acoustic targets with high spatial and temporal resolution over a roughly planar observation area, a fan of ≈120° by ≈2° (only the central 100° were

considered reliable enough for analysis). The pulse repetition rate was approximately 6 Hz so that bubbles at 1 and 20 m range were insonified by 1 and 30 consecutive pings, respectively. The locations of the detected bubbles are accurate to < 0.5 m because the distance resolution was 0.18 m, and the angular resolution of 1° corresponds to at most 0.4 m at the maximum range of 20 m. The horizontal orientation of the unit was set using a gimbal and measured to remain within $\approx$0.2° of horizontal with an onboard pitch-roll-heading sensor.

2.2.5 Identification of ebullition events

The combination of the vertical (alongship) beamwidth of the sonar fan, lateral resolution, beam overlap, and instrumental noise made identification of individual bubbles unreliable, given that multiple bubbles could arrive clustered together in space. Instead, the sonar signals were combined in space (described above) to estimate the flow rate and delimited in space and time to identify ebullition events.

After the raw data were smoothed with a 5-second moving average filter and coarsened to 1-second resolution, they were thresholded to identify connected groups of pixels contributing a minimum flow rate, 0.03 mL/min. Ebullition events, comprising a series of bubbles released in rapid succession from the same location, were identified from the time series of flow rates from these active groups as periods of nonzero activity with breaks of no more than 2 s. The volume of gas estimated by the sonar was adjusted to STP.

Classification of events

Events were identified from the sonar data in a way appropriate for detecting and quantifying ebullition, although other targets can manifest themselves as bubble events. The bottom of UML is a fairly quiescent zone, with slow seich-driven current on the order of 5 cm/s and oxygen levels too low to support aerobic biota like fish. However, strong sonar returns were caused by ropes and chains connecting buoys to anchors. These targets can be clearly distinguished from bubbles by their per-

sistence and slow lateral drift, which can be observed directly in animations of the sonar signal. We implemented an automated workflow, which classified the events using thresholds on their duration, total volume released, and intensity (mean and maximum flow rate). The values of these thresholds were chosen to as to achieve high rates of correct identification of both bubbles and anchors.

The values of these thresholds were chosen to as to achieve high rates of correct identification of both bubbles and anchors. The period of April 1-2, 2012 showed particularly strong anchor activity and was reviewed carefully to identify all the anchor signals so that they could be characterized, using the following procedure:

1. Plot maps of daily flux, similar to Fig. 3-5.
2. Visually identify localized spatial maxima, and for each:
3. Plot the time series in the spatial region for that day.
4. Identify time periods of enhanced activity, and for each:
5. Watch animation of those periods on the DeltaT.exe program that plots the raw .837 data
6. Look for persistence and lateral drag to characterize as anchor.

For each anchor deployment, a span of range, direction and time was delineated that encompassed the anchor signal with minimal excess. Any events occurring within the spatiotemporal span of an identified anchor was identified as an anchor, and this was reasonable because the anchors clearly dominated these spans. Anchor lines typically manifested as more persistent and intense events than ebullition, and in cases where the distributions were distinct, appropriate thresholds were obvious. For example, anchor-derived events frequently created simulated total volumes of over 100 mL, while no ebullition events released as much in that period, so that 100 mL used as the threshold. A threshold for the maximum instantaneous flow rate, 350 mL/min, was chosen in the same manner. The mean flowrate and duration showed significant overlap between the bubbles and non-bubbles, however, so thresholds were identified

so as to achieve high rates of correct identification of both bubbles and anchors (Supplemental Figure 2-6).

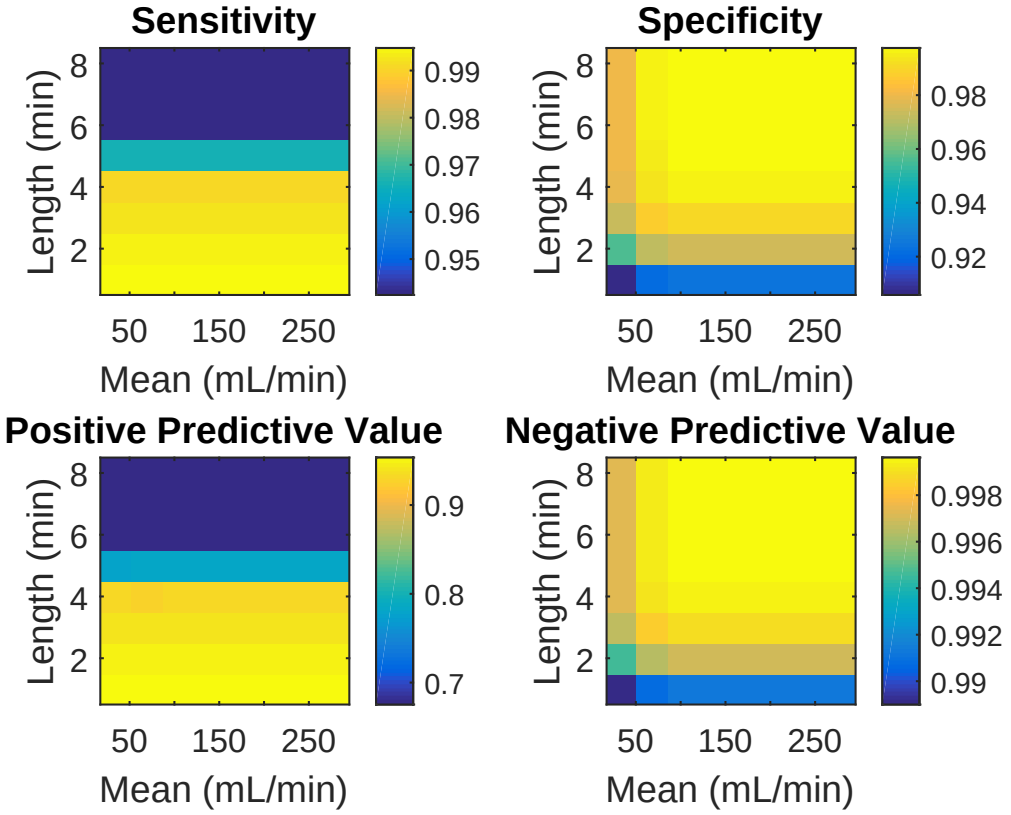

Figure 2-6: Sensitivity, specificity, positive and negative predictive value of bubble classification method for a range of thresholds on the maximum duration and mean flow rate of events. The sensitivity is the fraction of gas volume from bubbles correctly identified, and the specificity is the fraction of simulated volume from anchors correctly identified. The positive predictive value (PPV) is the fraction of the volume identified as bubbles that comes from bubbles, and the negative predictive value is the fraction of volume identified as anchors that comes from anchors. There was no global maximum for all four measures, but the thresholds of 3 min and 100 mL/min maintained the sensitivity and specificity above 99% with the PPV at 94%.

Rates of correct bubble classification were quantified using the metrics of sensitivity, specificity, and positive and negative predictive values, which are typically used to evaluate methods for disease detection. Each event was classified as ebullition or not, both from the manual identification described above (considered truth) and from the automatic identification using the thresholds being evaluated. Rather than count-

ing the number of correct or incorrect identifications, the metrics were estimated by the sum of the volume released during events, to account for the strong episodicity observed.

The sensitivity of a set of thresholds is the fraction of bubble volume that is correctly identified as bubbles, and the specificity is the fraction of anchor "volume" correctly identified. There was a strong trade-off between sensitivity and selectivity with the duration threshold, but the combination of 3 min duration and 100 mL/min mean flowrate maintained both at above 99%. The positive predictive value (PPV) is the fraction of volume identified as bubbles that actually comes from bubbles, and this value was lower at 94% because the total volume of simulated gas from anchors was much higher than the bubble volume during the two days analyzed. Thus, this is a likely conservative estimate of the PPV over the entire deployment period. On the other hand, subsequent periods could theoretically include longer or more intense ebullition events, and these would be spuriously classified as anchors and reduce the sensitivity of the event classification method. Future research could be performed in refining the method for distinguishing bubbles from secondary targets, for example by detecting slow lateral drift characteristic of many anchor lines.

2.2.6 Directional sensitivity

Every sonar unit exhibits directionality dependence in the strength of the sonar returns. To correct for this dependence, we normalized the data with a beam pattern found through a combination of detailed calibration and tuning to eliminate the remaining large-scale pattern. The beam pattern of an Imagenex 837B sonar unit was measured in the ocean engineering tank at the University of New Hampshire (UNH) using a 38.1 mm diameter tungsten-carbide calibration sphere, using a rotating pole to turn the sonar head horizontally (athwartship) and a motorized spool and sensor to raise and lower the sphere vertically (alongship). Tests were carried out at 4 and 8 m, though the 8 m test was less reliable due to interactions with the wall in one direction. The high-resolution 4-m test shows a roughly Gaussian shape with a central peak and high-frequency oscillations that correspond to the sensitivity within each

beam (Fig. 2-7, left).

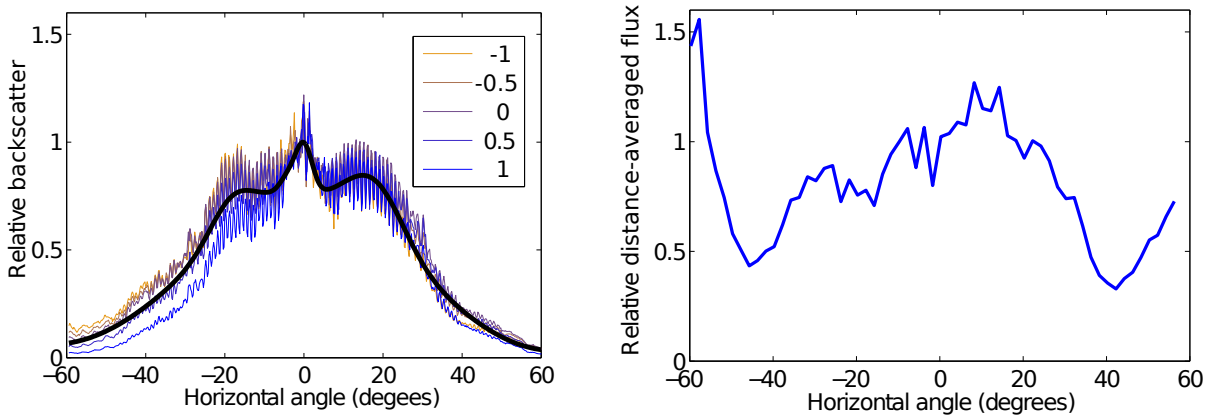

Figure 2-7: Left: beam pattern from a calibration sphere shows a roughly Gaussian shape. The variability in backscatter across each 1-degree beam corresponds to the sensitivity within each beam. Each line represents the pattern at a different elevation angle (legend in degrees). The black line superimposed is the calibration-sphere beam pattern. Right: average flux values as a function of direction (2° resolution) from the April 2012 data corrected with the uncorrected beam pattern (left subfigure), normalized to the value in the central beams.

When corrected with the calibration-sphere beam pattern intensity, the resulting long-term ebullitive flux data still showed a recognizable residual directional dependence (Fig. 2-7, right). The symmetry and temporal consistency of the residual directional dependence indicates that it more likely arises from the measurement system than from an actual spatial pattern of ebullition heterogeneity. This suggests that the beam pattern measured with the calibration sphere did not fully account for the field measurements at UML. This discrepancy may be due to the nearby walls in the tank impacting the measured signal, although the beam pattern measurements were carried out at a closer range than any wall reflections. The discrepancy may also arise from differences between the immobile sphere used for calibration and rising bubble targets detected in the lake. Motion of the bubbles may decorrelate the sonar pulse in time, spreading the sonar signal over neighboring beams and reducing the magnitude of the flow rate estimate. This effect is expected to play a larger role in the outer beams. Ultimately, to address this issue, the residual directional dependence of the flux record was used to correct the beam pattern.

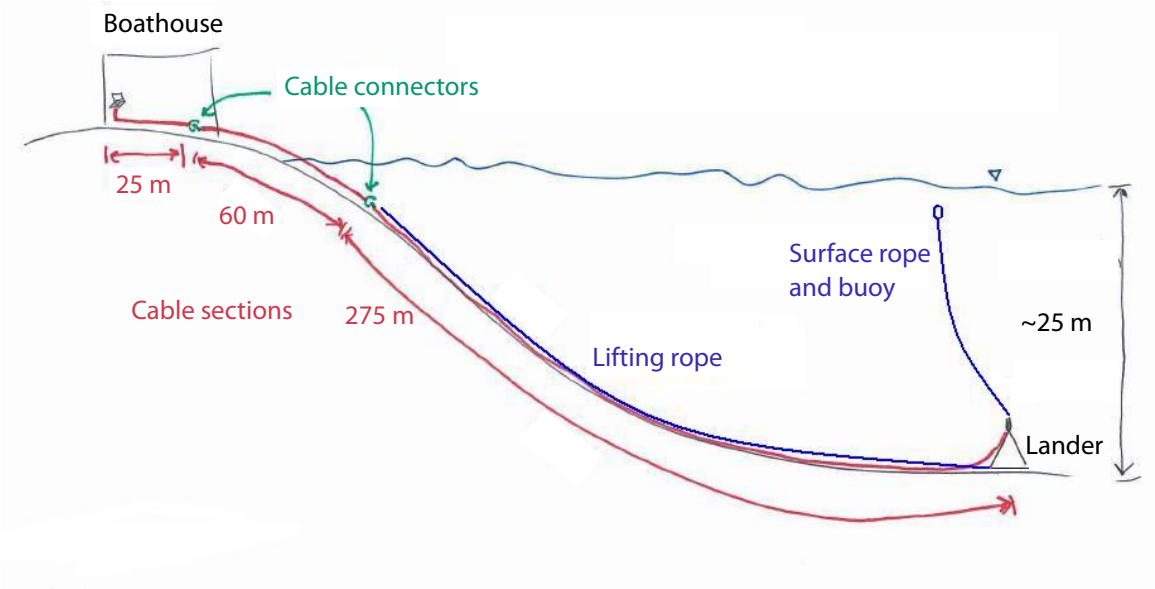

Figure 2-8: Profile schematic of the layout of cables and lander relative to the shore connection. Breakaway connections (green) were placed in locations designed to prevent human interference from damaging the equipment on shore or underwater. Not to scale.

2.3 Design and deployment of the sonar tripod

2.3.1 Remote power, communications and cabling

Due to the long desired deployment period and necessity to leave the lander undisturbed, batteries were considered impractical for powering the sonar, which draws up to 5 W of power. Dataloggers would have similarly been impractical given that the unit generated data at a rate of approximately 5 GB/day, though advances in storage technology may allow this method to be feasible in the future for medium-term deployments. Instead, the power, computer control and data storage were provided from shore via a cable laid along the bottom of the lake to the sonar unit (Fig. 2-8).

Controlling the unit from shore greatly simplified the design but also added security considerations. The shore power and storage for the control computer and communications equipment was provided courtesy of the Tufts sailing team, in their boathouse just East of the Mystic Lakes dam. The sailing boathouse docks are also used by the public for swimming and fishing, so it was important to secure the system to prevent someone from damaging the equipment by pulling on the cable. To

address this concern, the cable was deployed in segments of lengths 25, 60 and 275 m so that only the central 60-m segment that was exposed outside the boathouse and above water was connected to the end-segments with breakaway connectors (wrapped with tape instead of threaded with the provided screw fittings) that would disconnect given a strong yank. However, none of these connections were broken during the deployments presented in this work.

The Imagenex 837B DeltaT is controlled using an ethernet connection, but that protocol is limited to 100 ft, much shorter than the $\approx$ 1200 ft (360 m) distance from the shore to the lander deployment location. To overcome this hurdle, communications were routed through an ethernet extender (Patton 2168A), which was purchased pre-configured and housed in underwater and topside containers from Imagenex. The extended ethernet data connection was carried over a twisted pair of wires, along with a second pair of wires that carried the power through the neoprene-covered cable to the sonar. The 16-gage wires had lower resistance (13 ohm/km) than needed given the permissible resistance of $\approx$ 17 ohm during normal operation, but it was important to allow the 12 A inrush current needed to trigger initiation of the sonar transducer [*Spence*, 2016].

2.3.2 Lander design

The lake-bottom lander was designed to hold the sonar unit in a fixed location with horizontal orientation over the scale of months. The tetrahedral frame provided stability while leaving freedom for a central pipe to orient itself vertically on a gimbal, ensuring that the sonar unit remained level. The orientation was measured with an onboard pitch, roll and heading sensor, with typical variation of up to 0.2° due to currents with speed $\sim$ 1 m/min. The force ensuring that the unit remained vertical was provided by the ethernet communications bottle mounted at the bottom of the central pipe, with excess mass (relative to the mass of its volume in water) of 5.7 kg, compared with only 1.1 kg from the sonar head at the top of the pipe. The range of motion of the central pipe and gimbal ensured that the unit would self-level even if the tripod base settled at an angle of up to 20° from horizontal.

The lander form and underwater excess mass were designed to keep the tetrahedral frame stationary. To prevent the unit from settling too far into the mud, the excess mass of the sonar equipment and tripod (approx 21 kg) was offset using 3.9 L of closed-cell styrofoam, which was machined to fit underneath the top plate and within the legs of the tripod, providing approximately 12 and 2.3 kg of buoyancy, respectively. This brought the theoretical excess mass of the unit as a whole to 6 kg. Vertical and lateral displacement was also reduced by the addition of circular pads 41 cm in diameter that created suction with the sediment and vertical pipes 61 cm in length.

While the cabling system was designed to prevent accidental damage to the equipment from a human on shore, multiple features of the lander were also designed to prevent damage from activity on the lake while also providing redundant options to recover the lander. In particular, recreational boating activity is common on UML from March through November depending on weather and ice conditions. Multiple sailing teams practice on the lake and regularly shift the locations of marker buoys used to define race courses, and these buoys employ a variety of anchor systems that could damage the exposed sonar transducer or snag the data cable.

The first strategy used to minimize interference with the lander was to avoid advertising its location. While it had a recovery buoy attached to a harness for lifting the sonar from above (Fig. 2-9, left), the buoy was kept ≈ 0.25 m below the water surface. This presented a challenge during recovery, even though GPS coordinates allowed location within ≤ 10 m, as the buoy was not easily visible from the surface during periods of high water on the lake. In case any of (a) the buoy could not be located, (b) the tripod became so strongly suctioned into the mud that lifting it by the main harness was impractical, or (c) the data cable became snagged, the tripod was designed to be lifted by its data cable. To protect the sonar equipment and cable, the cable was attached with slack to a 3/8 in diameter Dacron rope tied to a bottom corner of the tetrahedron. Lifting by this rope would allow one to pry the tripod off the bottom with less force than pulling by the central harness. In case the rope failed, the cable was attached to the same corner with a wire strain-relief cable grip (Fig. 2-9, right).

Figure 2-9: Left: photograph of the lander suspended by its top harness from the back of a boat, before being towed slowly underwater to its deployment location. Right: photograph of a base corner of the tripod before deployment, showing both rope and data cable strain-relief loops attached to a PVC leg of the tripod. These were critical in preventing damage to the sonar when the tripod was accidentally lifted by the data cable when an anchor snagged it. Beneath those is visible the quick-release pin holding the PVC leg into the speed rail aluminum corner fitting, one edge of the aluminum triangular base, and a round PVC pad to prevent significant settling into the mud.

The corner-lifting scenario was employed once by members of the Tufts sailing team, who had caught an anchor on the data cable. On 10/9/12, beginning at 20:24 UTC (16:24 local time), the pitch-roll-heading sensor recorded erratic behavior, while the sonar signal began to show strong, spatially-coherent returns consistent with the fan's intersection with the sediment-water interface and then the air-water interface. For a period of about 1 minute, the sonar signal showed no returns, consistent with the head's being removed from the water. Subsequently the signal returned and eventually settled back into its normal, unobstructed horizontal view of the water column. This interpretation is consistent with the account of events provided by the sailing coach and suggests that the lander was moved by less than 10 m due to the constraint of the cable still on the lake bottom. No evidence of a change in operation was detected following this event, and no physical evidence of damage was apparent when the unit was recovered on 7/17/13.

The shore cable may have contributed to an episode where the sonar transducer was damaged. At 02:28 UTC on 5/30/13 (22:28 on 5/29/13 local time), the sonar unit suddenly disconnected from the shore computer and would not respond to attempts to reconnect. Upon recovery of the unit, it was unresponsive and sent to the manufacturers for service. The technicians discovered that 2 circuit boards, for communications and power, had both been damaged by an apparent power overload and required replacement (Fig. B-2). The timing of the disconnection is coincident with a thunderstorm that occurred between 22:22 and 23:23 on 5/29/3 local time, with lightning observed from the weather observatory at Boston Logan International Airport. A hypothesis for the cause of damage to the sonar is that lightning struck the lake itself, and the cable provided a low-resistance pathway through the fresh water to ground on shore. However, the cable itself showed no evidence of damage.

The metals used to construct the lander were designed to prevent galvanic corrosion of critical components. The sonar transducer had an anodized aluminum case. Bolts and strain-relief cable grip were all 316 stainless steel. The speed rail fittings and base triangle were made of aluminum and thus showed the greatest degree of galvanic corrosion, but these parts were thick enough to tolerate significant corrosion

without failure.

2.3.3 Deployment and recovery methods

Given the constraint of a small deployment watercraft, the optimal method for deployment of the lander on UML was to tow the lander underwater into position and lower it from its top harness, then to lay the cable along the bottom on the way back to shore. The lander may be transported in pieces and constructed on shore, then slid into the water. A suggested procedure for construction and entry into the water is:

1. Assemble base, including circular pads but not vertical piles
2. Install legs and foam floatation onto top plate
3. Position legs-and-top tripod over the base and attach legs onto base with pins
4. Install central pipe into gimbal
5. Attach ethernet communications bottle onto its bracket, then fit that onto bottom of the central pipe
6. Install sonar transducer onto top of pipe
7. Connect communications cables and strain-relief mesh
8. Tie on upper harness
9. Tie on temporary ropes to constrain motion of central pipe
10. Lay tripod on one side at dock edge and install vertical piles
11. Remove temporary ropes and slide the tripod into the water.

Once the tripod is in the water, it may be safely towed at $sim1$ m/s. The process of lowering the tripod into place may take 1–5 min depending on deployment depth and how quickly the rope-reinforced cable may be un-spooled. It is highly recommended

to deploy and recover the cable from a freely-turning spool to avoid tangling it. Therefore, under windy conditions it may be advisable to first place an anchor and buoy near the desired deployment location before towing the lander into position. Once the lander is on the bottom, the rope may be unspooled as the deployment watercraft slowly proceeds back to shore.

Recovery of the sonar was challenging, both because the tripod was not easily visible from the surface and because the process of re-spooling the cable is time consuming. Therefore, especially in conditions of high winds, it is advisable to re-spool the cable, working from the shore towards the lander, before raising the lander. The strength of the tape-wrapped breakaway connections was sufficient to raise the cable with slow, steady force without breaking the connection. In case the connection did break and the longest section of cable became isolated with the sonar underwater, it is advisable first to locate the subsurface buoy and attach a surface-visible buoy to it.

2.4 Discussion

The multibeam sonar lander described here enables multi-season, spatially-resolved observation of ebullition over a wide area of submerged sediments. The detailed calibration allows estimation of gas flow rates during ebullition events, given a measured or assumed distribution of bubble sizes. The system was designed for a maximum range of 20 m, appropriate for assessing behavior with high spatial resolution (≈ 0.5 m), but the sonar is capable of collecting data at a maximum range of up to 100 m. Others have used the Imagenex 837B on the 100 m maximum range setting to detect bubbles [*Roemer et al.*, 2015], although without the objective of quantifying gas fluxes. Deployment of a lake-bottom lander with such long range would require some consideration of the bathymetry, and a taller tripod or tilted orientation, to avoid substantially intersection the bottom with the sonar fan.

The requirement for re-normalizing the directional sensitivity of the sonar based on the long-term average flux suggests different behavior of rising bubbles vs. stationary

calibration spheres. The different directional sensitivity over subsequent deployments may also indicate slowly-changing mechanical properties of the transducer face (Section 5.2.1). A high priority for future deployments should be placed on understanding the origin of this directional dependence so that it can be compensated for without the ad-hoc solution presented above.

In principle the sonar lander could be deployed in other settings, including marine settings. The Imagenex 837B has been sold in units rated to 300, 1000, 2000 and 6000 m water depth. Marine deployments add significant complexity for long deployments due to the impracticality of providing power, control and data storage over a cable, except when one is already present [*Roemer et al.*, 2015]. In addition, strong currents would likely cause the gimbal system to shift orientation significantly, complicating data interpretation. To the extent that marine seeps may release gas at higher flow rates, the ability to quantify ebullition will be limited due to multi-scatter signals that increase in intensity with bubble density (Section 2.2.6). This contribution becomes non-negligible for flow rates between 10 and 100 mL/min, depending on the bubble sizes (Fig. 2-3).

Chapter 3

Field-scale spatiotemporal variability observed with a lake-bottom sonar lander

3.1 Introduction

Emissions from submerged sediments in lakes, rivers, wetlands and oceans contribute to atmospheric methane, but the nature and magnitude of the release remain uncertain. Owing to their buoyancy and high methane content, bubbles emitted from the sediment transport methane more efficiently than waters containing dissolved methane, and field studies suggest that ebullition is often the dominant mode of methane transfer to the atmosphere [*Martens and val Klump*, 1980; *Kuipphet and Martens*, 1982; *Crill et al.*, 1988; *Mattson and Likens*, 1990; *Keller and Stallard*, 1994; *Nakamura et al.*, 1999; *Bastviken et al.*, 2004; *Walter et al.*, 2006; *Delsontro et al.*, 2010; *Bastviken et al.*, 2011; *Maeck et al.*, 2013a]. Ebullitive emissions are episodic and spatially heterogeneous, which complicates upscaling of flux estimates [*Greinert*, 2008; *Ostrovsky et al.*, 2008; *Greinert et al.*, 2010; *DelSontro et al.*, 2011; *Wik et al.*, 2011; *Maeck et al.*, 2013b; *Walter Anthony and Anthony*, 2013; *Wik et al.*, 2013; *Bayrakci et al.*, 2014; *DelSontro et al.*, 2015].

The episodicity of methane venting may be driven by either the methane source or an external forcing, depending on which operates on a faster timescale [*Maeck et al.*, 2013b]. For example, drops in hydrostatic or atmospheric pressure trigger ebullition from methane-generating lake sediments [*Scandella et al.*, 2011] and marine sediments [*Martens and val Klump*, 1980; *Kuipphet and Martens*, 1982; *Chanton et al.*, 1989], possibly even in the presence of methane hydrates [*Torres et al.*, 2002]. Spatial heterogeneity in methane venting often manifests as hyperactive vents or vent clusters, sometimes referred to as hotspots [*Walter et al.*, 2006; *Wik et al.*, 2011; *DelSontro et al.*, 2015]. These focused release points may be associated with enhanced microbial methanogenesis [*Ostrovsky et al.*, 2008; *DelSontro et al.*, 2011; *Maeck et al.*, 2013a; *Wik et al.*, 2013], sediment morphological features like pockmarks [*Bussmann et al.*, 2011], a geologic source [*Walter Anthony et al.*, 2012], dissociating gas hydrates [*Westbrook et al.*, 2009; *Berndt et al.*, 2014; *Skarke et al.*, 2014], or rapidly degrading permafrost [*Shakhova et al.*, 2014]. The persistence of gas vents and the spacing and variability between them can potentially be used to distinguish the mechanisms controlling ebullition [*Greinert*, 2008; *Wik et al.*, 2011], but observations of these critical parameters are sparse and inconclusive.

Here, the spatial structure, persistence, and variability in the intensity of methane venting are analyzed using a high-resolution multibeam sonar record acquired at the bottom of a lake during multiple deployments over a 9-month period. We confirm that ebullition is strongly episodic, with distinct regimes of high- and low-flux largely controlled by changes in hydrostatic pressure. Our analysis shows that the spatial pattern of ebullition becomes homogeneous at the sonar's resolution over timescales of hours (for high-flux periods) or days (for low-flux periods), demonstrating that bubble conduits are ephemeral rather than persistent, and suggesting that long-term, lake-wide ebullition dynamics may be modeled without resolving the fine-scale spatial structure of venting [*Scandella et al.*, 2016].

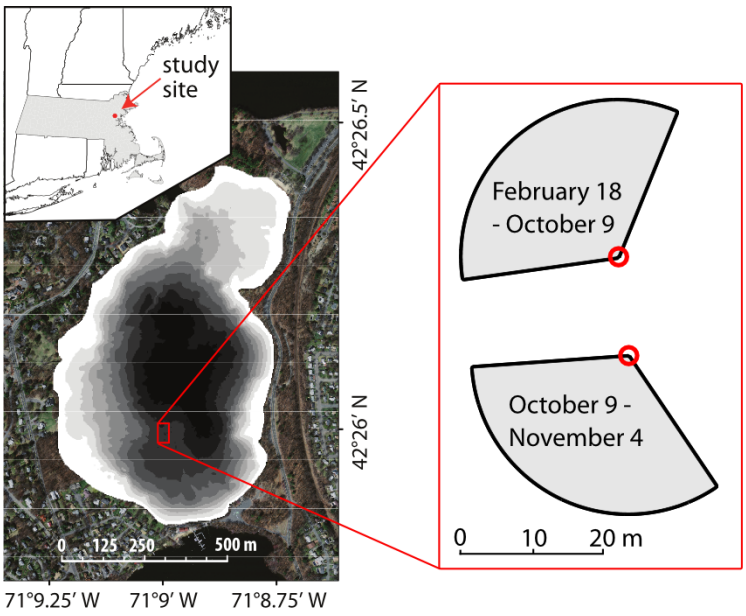

Figure 3-1: Location of Upper Mystic Lake (inset, Massachusetts, USA shaded) and bathymetry at 2.5-m shaded intervals superposed on an aerial photomosaic. Red square indicates the region bounding the deployment locations. Zoom right: map showing the relative locations and orientations of the 2 deployment locations where the data were collected in 2012.

3.2 Deployment locations and time periods

An Imagenex 837B DeltaT 260 kHz rotating multibeam sonar was deployed on a benthic lander in the deepwater basin (18-19 m) of Upper Mystic Lake (UML), an eutrophic kettle lake north of Boston, MA (Fig. 3-1). The sonar surveyed in a horizontal plane $\approx$ 1.5 m above the lake's bottom and $\approx 8-9$ m below the depth of observed thermoclines to collect data over a 9-month period in a $\approx$ 330 m^2 area. The sediments within this region are organic-rich $(20-40\%)$ [*Spliethoff and Hemond*, 1996] and remain anoxic and at roughly constant temperature beneath the $4-6°$ C hypolimnetic water [*Varadharajan*, 2009]. The previously-measured sediment accumulation rate of 0.5 cm/yr is expected to be homogeneous within the basin due to relatively flat bathymetry, and freeze cores from within the basin show strikingly similar depth profiles of arsenic concentration [*Spliethoff and Hemond*, 1996]. Over the scale of the lake, deposition rates are expected to be faster near the periphery and the northern end, where water flows in from a forebay. An identical sonar was calibrated

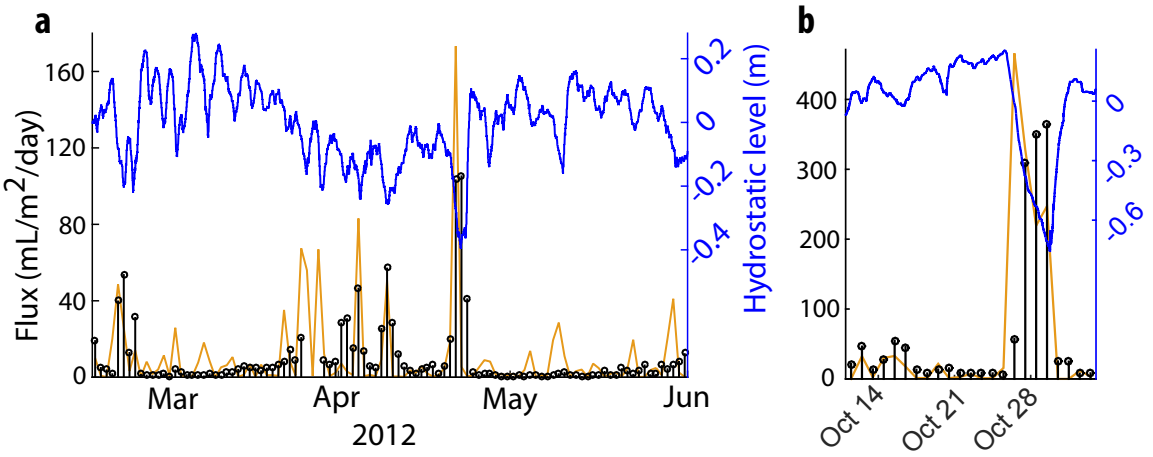

Figure 3-2: Time series of daily, spatially-averaged fluxes (black bars) from **a,** Feb 10 through May 31, 2012 shows that enhanced fluxes are triggered by hydrostatic pressure drops (blue line). The episodicity of this triggering can be reproduced using a mechanistic numerical model of gas release through dynamic conduits (orange line). **b,** Time series from October 2012, when a hydrostatic pressure drop of 1 m beginning on Oct 26 triggered massive venting (note the different axis scales) at a different location from the data presented in subfig. a (Fig. 3-1).

in a 1300 m^3 freshwater tank at the University of New Hampshire to convert the sonar signals into estimates of the instantaneous flow rate from bubble streams (Fig. 2-4), which were then integrated to calculate the flux associated with ebullition episodes.

3.3 Results

3.3.1 Episodicity of methane venting

Episodicity observed in spatially-averaged daily flux from the sonar data confirms that strong venting episodes can be triggered by drops in hydrostatic pressure (Fig. 2a), although the negative correlation of ebullition rate with hydrostatic pressure and its rate of change (R^2 = 0.5 and 0.1, respectively) is weak, primarily because not all hydrostatic pressure drops trigger ebullition episodes. For example, the releases in late February and late April 2012 are both followed by month-long periods of relative quiescence, despite several $\approx$ 0.3 m hydrostatic drops that had earlier been enough to trigger large methane releases. The duration of these quiescent periods reflects

the time for sediments to recharge the trapped bubbles to a size large enough to be susceptible to mobilization by hydrostatic triggering.

Hydrostatic triggering and a conduit dilation model

Hydrostatic triggering of ebullition may be explained mechanistically as a response to changes in effective stress. With falling hydrostatic pressure, total stress is reduced, forcing gas-charged sediments into a more tensile effective stress state. At a critical stress, gas-filled cavities then dilate near-vertical conduits to the sediment's surface [*Boudreau et al.*, 2005; *Jain and Juanes*, 2009], and the critical stress may be modeled assuming that the sediment-water matrix is elastic [*Algar et al.*, 2011a,b] or plastic [*Scandella et al.*, 2011]. The timing and relative magnitude of many of the peak ebullition events can be reproduced using a numerical model [*Scandella et al.*, 2011] that captures this process and that is tuned with another UML dataset (Fig. 3-2). The tuning parameter, the ebullition number, controls the episodicity of methane fluxes and reflects the balance between the tensile strength of the sediment-water matrix and the characteristic hydrostatic pressure variations. The model can capture the features of most large ebullition events, although it does not fully reproduce the long quiescent periods during March and May 2012 (Fig. 3-2).

The episodicity of spatially-averaged fluxes was reproduced with a numerical, mechanistic model of methane gas transport through dynamic conduits that dilate in response to changes in effective stress [*Scandella et al.*, 2011]. This 1-D model captures the accumulation of trapped gas in a vertical column of sediment and tracks the gas pressure and volume as a hydrostatic pressure forcing triggers plastic deformation of the sediment-water matrix surrounding gas cavities. When the effective stress reaches a depth-dependent tensile strength threshold, the gas forces open a conduit to the surface and escapes. The fundamental parameter of the model, called the ebullition number, N_e, reflects the balance between the vertical gradient in tensile strength of the mud and the characteristic magnitude of hydrostatic pressure changes. Larger values of N_e require larger, rarer drops in hydrostatic pressure to release gas from the deepest sediments and thus drive more strongly episodic venting. In this study, the

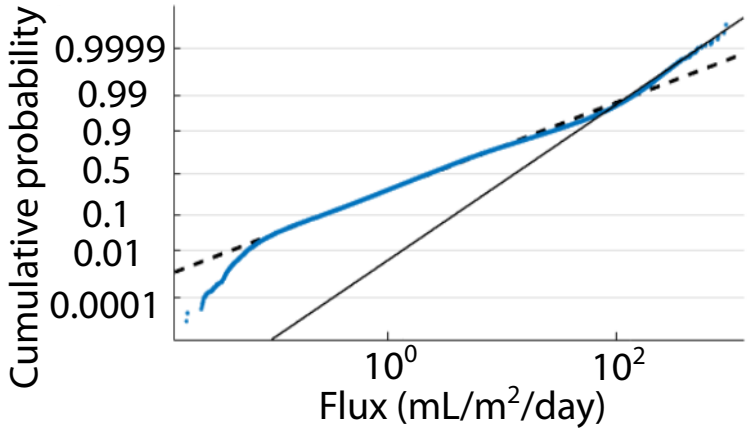

Figure 3-3: Cumulative distribution of 1-minute spatially-averaged flux values shows three distinct lognormal regimes, which each appear as lines of constant slope on the given axes.

best-fit value of $N_e = 5$ was the same as in a previous study on UML that quantified ebullition with floating bubble traps [*Scandella et al.*, 2011].

Distribution of flux magnitudes

The high temporal resolution, together with the large areal coverage and long duration of the sonar record, allows for a more detailed analysis of ebullition dynamics that had previously been possible with bubble-trap methods. High-frequency flux measurements (binned at 1 min) show that approximately 98% of the flux measurements follows a lognormal distribution over three orders of magnitude (0.1–100 mL/m^2/day), with parameters log-mean $\mu = 0.62$ and log-standard deviation $\sigma = 1.8$ (Fig. 3-3). Smaller and larger flux measurements are fit by lognormal models with smaller variance, $\sigma = 0.5$ and 1.0, respectively.

Lognormally distributed measurements typically arise from processes controlled by the product of independent factors, which in this setting may include the bubble mobilization rate over the observation area and heterogeneity in conductivity of dynamic gas escape pathways. A flux distribution composed of multiple lognormal regimes was also observed at natural hydrocarbon seeps in a marine setting, although in that study the high-flux regime constituted 13% of the flux measurements, com-

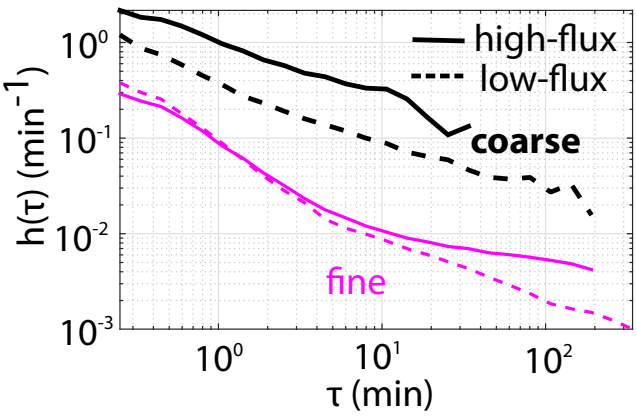

Figure 3-4: The hazard function h decays as a power law with inter-arrival time τ for coarse (64 m^2, black) and fine (0.25 m^2, red) pixels during high-flux (solid lines) and low-flux (dashed lines) periods.

pared with $\sim 1\%$ here [*Clark et al.*, 2010].

Temporal clustering of ebullition events

Further insight into processes controlling ebullition is furnished by the distribution of inter-arrival times between bubble release events—'events' are bubble-release sequences that persist with breaks no longer than 2 s (given 5-s moving-average filtering). Distributions of inter-arrival times may be analyzed using the hazard function,

$$h(\tau) = \frac{f(\tau)}{1 - F(\tau)}, \tag{3.1}$$

where $f(\tau)$ is the probability density function (PDF) of inter-arrival times τ, and $F(\tau)$ is the cumulative density function (CDF) [*Stapelberg*, 2009]. $h(\tau)$ quantifies the probability of an event occurring conditioned on a given amount of time having passed since the last event. For a Poisson process, events are independent and have uniform probability, corresponding to constant h since the events have no memory of previous arrivals. For a Weibull process—a model often used in reliability engineering to model component failures—the hazard function is a power law, $h(\tau) = (\beta/\lambda)(\tau/\lambda)^{\beta-1}$, where β and λ are the shape and scale parameters, respectively. A decreasing power law ($\beta < 1$) corresponds to strong temporal clustering, while an increasing power law

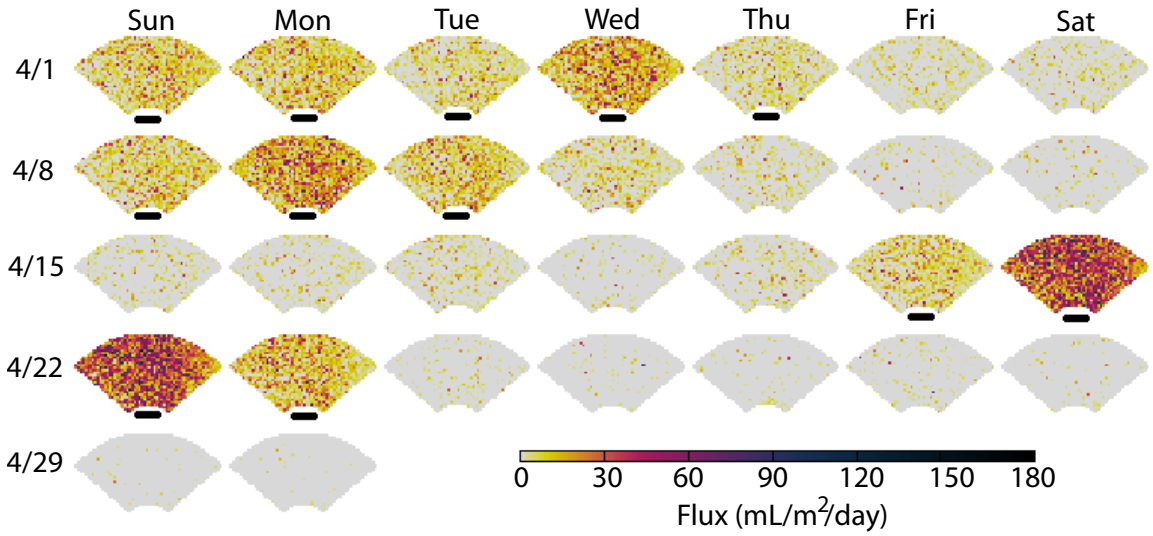

Figure 3-5: This calendar representation of daily sonar-detected gas venting in April 2012 shows the spatial variability of methane fluxes across the sonar detection area. Days with higher than average flux are underlined.

($\beta > 1$) is associated with more regularly periodic arrivals [*Stapelberg*, 2009].

In UML, ebullition events are characterized by decaying power laws. For events collected from a 64-m^2 averaging area, the decay in both high- and low-flux regimes is well fit by $\beta \approx 0.4$, which reflects mild temporal clustering (Fig. 2d). At the fine-scale resolution of the sonar (0.25 m^2), $h(\tau)$ shows two distinct regimes characterized by different power-law scalings. For short-term inter-arrival times ($\tau < 5$ min), the decay has a slope less than -1, indicating stronger short-term clustering than possible with a Weibull process, which requires $\beta > 0$. The power-law regime does not extend over all τ but instead transitions to a regime of more gradual decay over long inter-arrival times ($\tau > 5$ min), consistent with re-establishment of sediment cohesion and healing of vent conduits. Over long τ, the high-flux regime shows even more gradual decay in $h(\tau)$ than the low-flux regime, implying a larger role for independent arrivals.

3.3.2 Spatial heterogeneity in methane venting

The spatial structure of methane venting is found to depend on the overall flux regime (high- vs. low-flux). Daily gas flux maps during high-flux periods reveal gas release from densely-spaced outlets, while the low-flux periods are associated with sparser

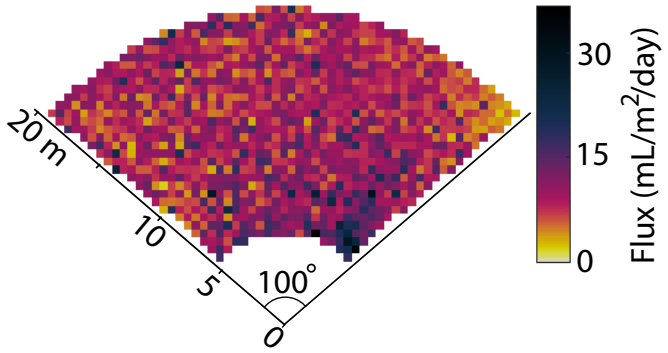

Figure 3-6: Average flux map from March–May 2012.

venting (Fig. 3-5). The ubiquity of venting across the observation area during high-flux periods may reflect the relative homogeneity of methanogenesis, whose controlling parameters (sediment accumulation and temperature) are fairly homogeneous above the meter scale in the deepwater basin [*Spliethoff and Hemond*, 1996].

During high-flux periods, ebullition events occur in clusters of enhanced activity, although, over time, events appear throughout the field of observation. While some locations vent gas at over 3 times the spatiotemporal mean flux of 10 mL/m^2/day (Fig. 3-6), these contribute only 1% of the total flux, suggesting a minimal role for hot spots. Instead, gas appears to be released through independent, near-vertical conduits or conduit networks linked to outlets, where the scale of lateral transport or significant heterogeneity in sediment properties is less than the resolution of the sonar, 0.5 m. Such a laterally-dense network of release pathways should develop in sediments that generate methane throughout their bulk. In this case, transport from the sediment matrix towards release pathways would be diffusion-limited to a distance on the scale of centimeters in the days to weeks between ebullition events. The outlet and conduit spacing may also be controlled by heterogeneity in the chemistry and mechanics of the sediments, though our results show that such heterogeneity does not give rise to persistent outlets spaced more than 0.5 m apart.

A spatial clustering analysis of the observed methane-flux signal yields additional

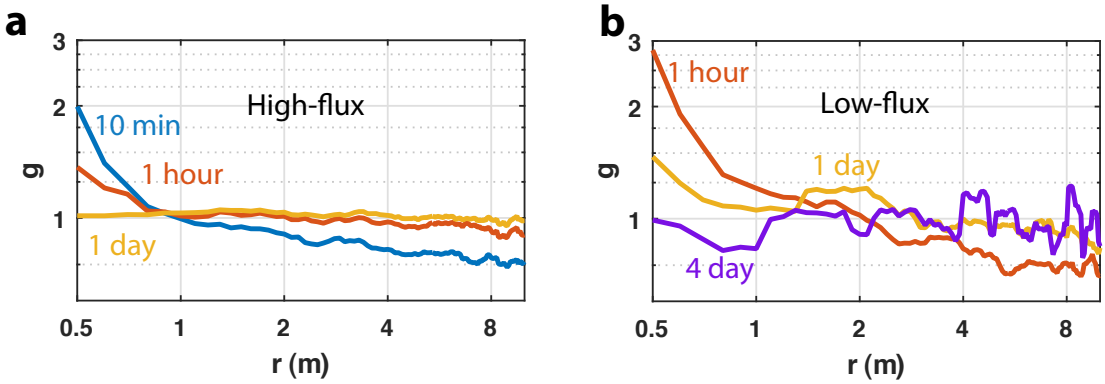

Figure 3-7: Radial distribution function (RDF), $g(r)$, for high-flux (**a**) and low-flux (**b**) periods during Spring 2012.

clues about the system's self-organization. Our analysis is based on the radial distribution function (RDF), $g(r)$, which detects clustering as a function of inter-point distance r [*Illian et al.*, 2008] (see Methods and SI). The analysis yields $g > 1$ for short-range ($r < 1$ m) events over short time periods (10 min and 1 hr samples), indicating a high areal density of events relative to a completely spatially random (CSR) process. The short-range clustering is balanced by long-range spacing ($g < 1$ for $r > 1$ m). This signature of short-range clustering and long-range spacing was strongest for 10-min samples and became progressively weaker for longer duration samples, eventually decaying to a homogeneous RDF ($g(r) \approx 1$) over daily samples (Fig. 3-7). This clustering signature indicates that gas is vented from nearby, distinct outlets within a short period of time (see Appendix A).

Compared with the high-flux regime, low-flux periods show both stronger variability and longer persistence in the structure of the heterogeneity. For a given observation duration, the coefficient of variation (CV) across space is more than twice the CV from high-flux periods (Fig. 3-8). The spatial structure of this variability is evident in the RDF, which exhibits short-range spatial clustering that is similar to the clustering observed during high-flux periods, except that it extends to $r \leq 2$ m and persists over timescales as long as one day (Fig. 3-7).

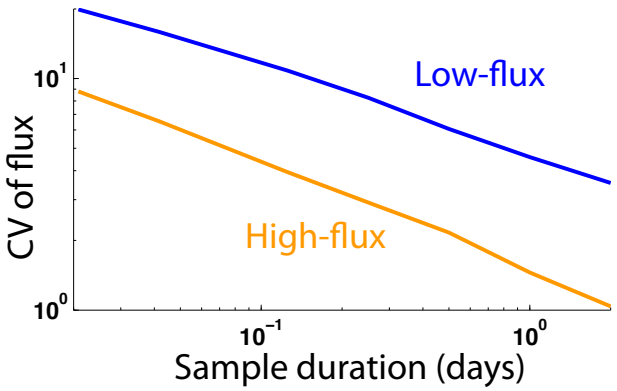

Figure 3-8: Spatial coefficient of variation (CV) between flux measurements on a grid with resolution of 0.5 m, averaged over samples of duration 1-24 hr collected during Spring 2012.

Combined spatiotemporal clustering

The ephemeral nature of spatial clustering evidenced by the RDF is consistent with the spatial localization of short-term temporal clustering observed in $h(\tau)$ and is likely associated with the same process. Ebullition events may trigger "aftershock" events by mechanically disturbing nearby sediments that contain critically-stressed gas pockets. Due to the compliance of the sediments and the small magnitude of deformation associated with bubble passage, this mechanism would likely require that trapped bubbles be spaced only a few centimeters apart, which is a reasonable assumption given the limited distance over which diffusion could source methane to a bubble.

The decay of clustering over progressively longer periods indicates that individual outlet clusters are active for a short time but do not persist to dominate the long-term flux pattern. Instead, independent outlets or clusters subsequently become active at intermediate, independent locations until the domain is filled with emission sites approximating a CSR pattern. The clustering pattern in the RDF decays faster during high-flux periods, suggesting that higher fluxes arise primarily from more frequent initiation of spatially-independent events. The spatial independence of new arrivals over long time periods is consistent with the conceptual model that long-term, large-scale fluxes are driven by hydrostatic pressure drops, which act equally over the

sediment surface to liberate trapped gas.

3.3.3 Uncertainty analysis

Flux measurements

The uncertainty associated with flux measurements is estimated to be ∼70% and is primarily derived from variability and uncertainty in the bubble size distribution (BSD), although the uncertainty in bubble rise speed, source amplitude, beam pattern and instrument noise were considered. The flux may be expressed as:

$$q = cK \sum_{i=1}^{n_{event}} \sum_{j=1}^{n_{ping}} \left(\frac{\overline{\sigma}_{bs}}{R} \right) \tag{3.2}$$

$$= \frac{cK}{a_0} \sum_{i=1}^{n_{event}} \sum_{j=1}^{n_{ping}} \left(\frac{a_{\Delta TR}}{B_h(\theta) G} \right), \tag{3.3}$$

$$c = \frac{\Delta t_{ping}}{\Delta t_{sample} A}, \tag{3.4}$$

where K is the calibration coefficient (L/day/m), Δt_{ping} is the time between pings, n_{ping} is the number of pings in a given event, and Δt_{sample} and A are the duration and observation area of the sample over which the flux is calculated from the sum of n_{event} events. The backscattering is calculated using the instrument-reported sonar amplitude, $a_{\Delta T}$, and the source level amplitude a_0.

The product $n_{ping} \times n_{event}$ is large for most flux estimates presented in this work, and the averaging over so many measurements makes the contribution from instrument noise negligible. However, the parameters K, a_0 and $B_h(\theta)$ all have significant uncertainty. Each is independent and contributes multiplicatively to q, so the relative uncertainty in q can be estimated using propagation of uncertainty:

$$\frac{\mathrm{var}(q)}{q^2} \approx \frac{\mathrm{var}(K)}{K^2} + \frac{\mathrm{var}(a_0)}{a_0^2} + \frac{\mathrm{var}(B_h)}{B_h^2}. \tag{3.5}$$

The uncertainty associated with the calibration coefficient K derives from 3 sources: uncertainty in the bubble rise speed u_{rise}, uncertainty in the long-term BSD, and

short-term variations in the BSD (Eq. (2.17)).

A number of models for bubble rise speed have been developed, and the nature of the bubble interface ("clean" vs. "dirty") can cause discrepancies of up to $\approx 40\%$. However, in a study of marine gas fluxes using the same inverse hydroacoustic method, the relative error between 7 different models contributed only 15% relative uncertainty in K and Q [*Veloso et al.*, 2015]. Plumes of rising bubbles may create upwelling velocities that allow bubbles to rise faster than the terminal velocity of an individual bubble. However, for the relatively low flow rates observed in UML ($Q \leq 20$ mL/min), upwelling velocities are observed to be limited to 2 cm/s, less than 10% of the terminal velocity [*Leifer*, 2010]. Thus, we estimate a combined relative uncertainty of 18% for the rise velocity.

The uncertainty in the long-term BSD may be estimated as $\approx 23\%$ using the relative difference in calibration coefficients calculated using BSDs from UML [*Delwiche et al.*, 2015] and Lake Kinneret [*Ostrovsky et al.*, 2008]. The final source of uncertainty in K is from short-term variations in the BSD, over timescales larger than the 5-second averaging period used to measure $\overline{\sigma}_{bs}$. We estimate that BSD varies from the long-term mean by up to $\sim$50% in the radius. If these factors have a multiplicative effect, then the combined relative uncertainty is $\sqrt{\text{var}(K)}/K \approx 58\%$.

The relative uncertainty in a_0 is estimated to be $\approx 22\%$ from the variability in values measured across the sonar fan in UML. The relative uncertainty in $B_h(\theta)$ is estimated to be $\approx 36\%$, from the coefficient of variance in the flux-derived correction to the beam pattern (Fig. 2-7, right) across θ. Using these values in Eq. (3.5), we find a combined relative uncertainty of $\sqrt{\text{var}(q)}/q \approx 70\%$. Over long time periods, the large number of bubbles samples will converge towards the system-wide BSD and reduce the uncertainty in K, the primary contributor to the overall uncertainty. However, because of the inverse relationship between K and r, this convergence in BSD does not guarantee that the flux estimates will converge on the long-term average if there is significant variability in the apparent BSD.

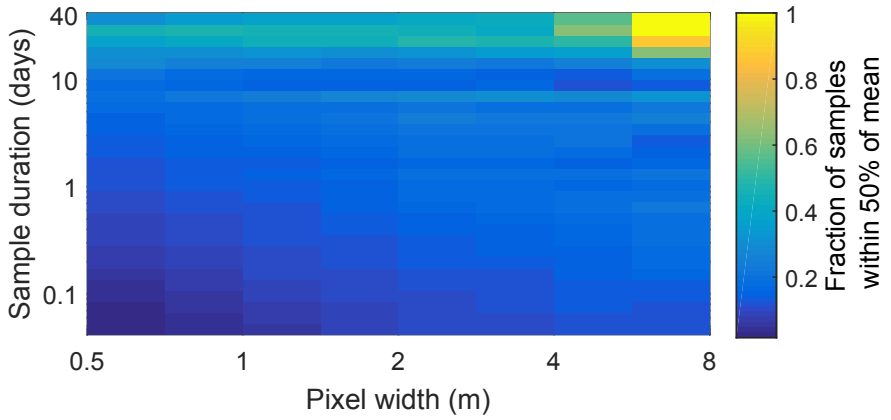

Figure 3-9: Spatiotemporal variability as a function of scale of measurement. Color scale represent the fraction of subsamples of the data from February 18–June 1, 2012 that fall within ±50% of the long-term, global average flux value, as a function of the spatial extent for gridding of fluxes (0.5-8 m) and duration (1 hr-40 days). Samples shorter than 1 day in duration or with a spatial scale on the order of 1 m (as with most bubble traps) are less than 50% likely to measure a sample within ±50% of the long-term mean. Only multi-week samples with spatial scale over 5 m always fell within ±50%.

Impact of upscaling results in space and time

The combined spatial and temporal resolution and coverage of the dataset presented here allows estimation of the uncertainty associated with upscaling data in space and time. Ebullitive fluxes are sometimes measured using bubble traps deployed at discrete locations over an extended time period [*Walter et al.*, 2006; *Varadharajan and Hemond*, 2012; *Maeck et al.*, 2013b; *Walter Anthony and Anthony*, 2013; *Wik et al.*, 2013], but extrapolating these measurements in space is almost certain to underestimate the spatial average [*DelSontro et al.*, 2015; *Wik et al.*, 2016]. Hydroacoustic surveys from ships [*Ostrovsky et al.*, 2008; *Greinert et al.*, 2010; *DelSontro et al.*, 2011, 2015; *Skarke et al.*, 2014; *Weber et al.*, 2014] cover large areas but only at discrete times, so extrapolating flux estimates in time may not represent the long-term average behavior. Here, we demonstrate the uncertainty introduced by showing the degree to which sub-samples of the data represent the average flux estimate over the first sonar deployment.

The flux estimates from the deployment from February 18–June 1, 2012 were

subsampled uniformly in space and time (gridded in space and time) at different spatial and temporal scales, and the fraction of subsamples that fell within ±50% of the long-term, global mean flux of 7 mg/m^2/day are shown in Fig. 3-9. The fraction of samples in the interval generally increases with larger spatial and temporal scales, reflecting the rate at which larger-scale, longer-duration observations become more likely to represent the overall mean. Some slight non-monotonicity in the trend may be attributed to time periods where the sensor was inactive. The long-duration (40 day) samples converge to 1 in the limit as the spatial scale increases to 8 m, but for finer spatial resolution significant heterogeneity remains. Similarly, the 8-m samples still show significant temporal variability for samples shorter than 10 days. These results are in agreement with a resampling study of trap-based methods, which found that a deployment period of 39 days and a set of at least 11 0.25-m^2 bubble traps was required to obtain estimates within ±20% of the upscaled flux with 95% confidence [*Wik et al.*, 2016].

3.4 Discussion

In summary, the high spatial and temporal resolution afforded by the sonar data allows discernment of discrete ebullitive episodes and vent locations, and the long deployments permit analyses over months' long periods. Our analysis shows that specific methane vents in UML do not repeatedly dominate fluxes during ebullitive episodes; instead, vents are frequently forming and closing off throughout the homogeneous sediments that make up the seep field in the lake's deep basin. This finding challenges the idea that sediment vents, once established, will continue to be the preferential loci over the scale of meters. While these results may not directly apply to settings with more heterogeneous geology [*Hornbach et al.*, 2004; *Walter Anthony et al.*, 2012; *Skarke et al.*, 2014] or patterns of sediment deposition [*Bussmann et al.*, 2011; *DelSontro et al.*, 2011; *Maeck et al.*, 2013a; *DelSontro et al.*, 2015] or erosion [*Paull et al.*, 2005; *Naudts et al.*, 2006], they suggest that the acquisition of longer and more spatially comprehensive datasets on ebullition events in such settings may

better constrain the relative importance of hotspot vs. distributed methane emissions from submerged sediments for both local and global flux estimates.

Chapter 4

Laboratory-scale spatiotemporal variability in an incubation experiment

4.1 Introduction

The sonar analysis presented in Chapter 3 shows that spatial clustering of ebullition is ephemeral at the scale of meters. However, the fact that venting becomes homogeneous at large scales over a day does not necessarily imply that finer spatial structure is destroyed. The field results set an upper bound on the spatial scale of lateral transport that could supply methane from a distributed source to a discrete outlet, 0.5 m. This finding is consistent with physical reasoning that diffusion operates over centimeters over the weeks between large ebullition events and that lateral traverse of bubbles through soft sediments is limited by buoyancy. However, the field work did not preclude the existence of persistent outlets spaced closer than 0.5 m. To investigate that possibility, and to test the mechanism of hydrostatic triggering of ebullition, we conducted a laboratory-scale experiment incubating reconstituted sediments to observe the locations and timing of gas release over a period of 10 months, presented in this chapter.

The conceptual model motivating our work is that bubble passage through sediments supports subsequent re-use of a gas conduit by temporarily reducing the sediment cohesion. Previous mechanistic modeling of bubble mobilization in the framework of linear elastic fracture mechanics [*Gardiner et al.*, 2003; *Boudreau et al.*, 2005; *Algar et al.*, 2011a,b] led to the speculation that bubbles tend to form in and follow the rise paths of previously-released bubbles due to partial healing of the fracture toughness (K_{IC}) of sediments [*Algar et al.*, 2011b]. We approach the mechanics from the perspective of plastic deformation, where the parameter setting the limit on effective stress under tension is the tensile strength, σ_T [*Scandella et al.*, 2011]. The mechanism of tensile strength reduction should support re-use of existing bubble conduits, diverting bubbles laterally to grow and rise towards existing outlets. Sub-vertical bubble rise has been observed in laboratory experiments in fine, uncompacted glass beads [*Kong et al.*, 2009] and gelatin [*Boudreau et al.*, 2005]. One way to evaluate the role of the strength reduction effect is to ask: over what spatial scale does this reduced cohesion cause conduits to be re-used in the context of laterally-homogeneous methanogenesis? If pre-existing conduits are significantly more favorable than undisturbed sediments, gas will be collected towards an outlet from a larger area, and the major outlets will show more distant spacing.

While the spacing of outlets is expected to be related to the magnitude of the drop in tensile strength, the persistence of drops is expected to depend on the rate of recovery of tensile strength. We hypothesize that σ_T is temporarily reduced by bubble passage and recovers slowly with time until the next release. Previous research on soft, fine-grained sediments has revealed recovery of the yield stress over the scale of months [*Merckelbach et al.*, 2002]. Mechanistically, this strengthening is explained as a result of decreasing distances between particles of neighboring aggregates during compaction, causing an increase in strength of van der Waals forces and hydrogen bonds [*Merckelbach*, 2000; *Merckelbach et al.*, 2002; *Holtz and Kovacs*, 2010]. If tensile strength recovers slowly relative to the timescale of gas generation, as suggested by previous studies, then outlets may be expected to be re-used over multiple cycles of gas generation and release, to persist over weeks or months.

Previous studies have investigated the flow paths from a point gas injection source to the sediment surface and found that bubbles escape at distant outlets due to sub-vertical migration during rise through migrating air channels [*Kong et al.*, 2009] in an expanding, parabolically-shaped "fluidized zone" [*Varas et al.*, 2011; *Ramos et al.*, 2015]. The width of a bubble release channel network increases with time, though that process appears to reach a steady state over the scale of minutes to hours and again occurs with gas supplied through a needle [*Kong et al.*, 2009, 2010]. While the fluidized zone increases in area over time, the majority of gas flow remains focused through a central channel [*Ramos et al.*, 2015]. These experiments involved significant simplifications relative to natural lake sediments: a needle injection source at constant flowrates, larger grains (diameter > 200 μm, vs. clay platelets of order $0.1 - 10$ μm), and no cohesion. Given these sparse observations, it was unclear what morphology of the conduit network would arise in the context of laterally-distributed methane, and how that morphology would develop over time. We hypothesized that the combination of tensile strength reduction and slow strength recovery would lead to outlets spaced at least 5–10 cm apart and that persisted in activity over the scale of weeks to months.

To observe this effect and attribute it to methane transport, it was important to remove the confounding influence of heterogeneity in methanogenesis. Methane generation rates are primarily controlled by temperature [*Liikanen et al.*, 2002; *Price and Sowers*, 2004; *Yvon-Durocher et al.*, 2014], but the availability of labile organic matter is another constraint. To address these issues, we carried out our investigation on sediments that were reconstituted with water, mixed, and run through a peristaltic pump to break up clumps of concentrated organic carbon.

A number of experiments have investigated how air injection at a point can enhance porewater exchange [*Klein*, 2006; *Yuan et al.*, 2007], create surface features [*Varas et al.*, 2009], and create bubbles whose size depends on the injection rate and grain size [*Greinert and Nutzel*, 2004; *Meier et al.*, 2011]. However, no studies have observed the spatial distribution of bubble release points from incubated natural sediments. *Comas and Wright* [2012] observed bubbles released from methane-generating peat with a downward-looking camera both *in situ* and in a

laboratory sample, but their focus was on quantifying the temporal variability in ebullition, rather than understanding the spatial component of interest here. Interestingly, that study found a positive correlation between atmospheric pressure and the ebullitive flux, compared with the majority of studies, which find that ebullition is triggered by falling atmospheric pressure [*Mattson and Likens*, 1990; *Fechner-Levy and Hemond*, 1996; *Tokida et al.*, 2007; *Scandella et al.*, 2011; *Varadharajan and Hemond*, 2012; *Yvon-Durocher et al.*, 2014], among other factors. In these experiments, we incubate sediments from UML and observe the spacing and persistence of bubble release points, while demonstrating that massive ebullition can be triggered by imposing drops in the hydrostatic pressure.

4.2 Methods

4.2.1 Physical apparatus and initiation

The physical apparatus was designed to incubate natural sediments while permitting manipulation of the water level, visualization of the time and lateral location of bubble release from sediments, and collection of the emitted gas (Figure 4-1). The sediments were held in an acrylic tank with external dimensions $46 \times 46 \times 51$ cm ($18 \times 18 \times 20$ inches) and wall thickness of 6.35 mm ($\frac{1}{4}$ inch). An aluminum frame was mounted around the mid-line of the tank in order to constrain its expansion with pressurization and to mount the light strips for imaging.

The tank was filled with slurried sediments and water in order to allow it to settle in an initially-homogeneous state. Sediments and hypolimnetic water were collected using an Ekman dredge from the deepwater basin of UML at 20 m water depth (43.4330 N, 71.1495 W), adjacent to the deployment locations of the sonar lander described in Section 3.2. Approximately 77 L of dredged, watery sediments and 15 L of hypolimnetic water were slurried in a 55-gallon drum using a paint-mixing drill bit for 5 minutes, with the top of the drum sealed around the drill bit and headspace purged with nitrogen gas to minimize oxygenation. The reconstituted sediments

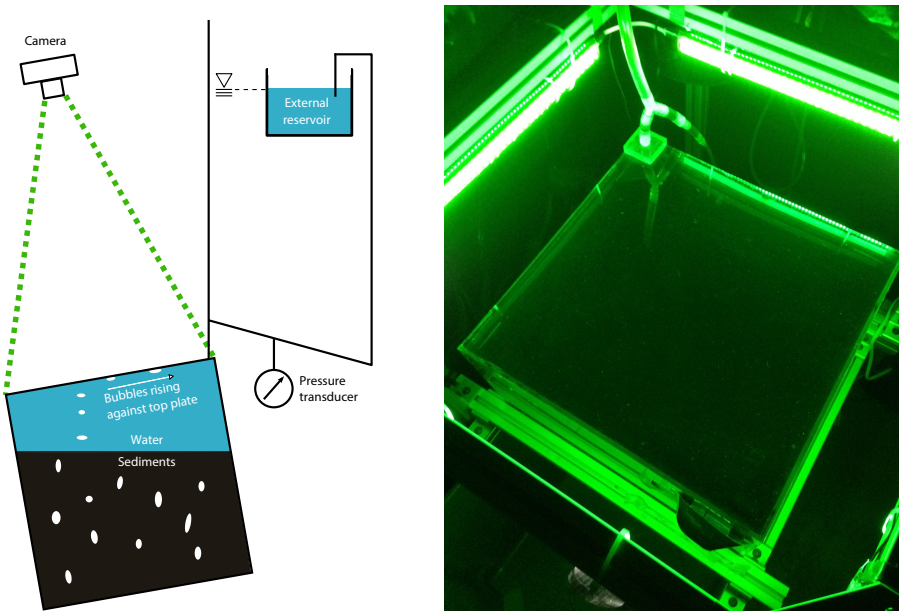

Figure 4-1: Left: diagram of the mud incubation setup. The tank was filled with sediments and water so that bubbles were generated by microbial methanogenesis. Upon escaping from the sediments, bubbles rose through the water onto the top plate, along which they slid to the upper corner, where they escaped through an outlet tube that was large enough (3/8 inch internal diameter) to permit them to rise into the outlet column for collection (when the outlet was closed at the top and filled with water) or venting to a fume hood. The water level was maintained above the top of the tank with an external reservoir, and the pressure was measured with a transducer attached to the plumbing. Right: image of the tank setup from an oblique view above. Light was provided by 4 LED light strips covered with green filters to inhibit photosynthesis, and the tank was restrained at mid-height with an aluminum frame of 80/20. The outlet tube is visible at the upslope corner.

were then transferred into the tank using a peristaltic pump over 8 hr, which further pulverized any remaining small clumps of mud. Approximately 10 g of larger solid material (mainly leaves and sticks) were removed during this process. While the sediments appeared to remain suspended during the filling process, the direction of the inlet tube was varied periodically to avoid preferentially loading any region of the tank or scouring away early-deposited sediments.

After the tank was filled, the sediments were allowed to settle and incubate at laboratory temperature (20-22°C) for 6 months prior to the experiments presented here. During that time, the sediments generated and released more than 3 L of gas. The level of the sediments was 26 cm above the bottom of the tank after filling, and it compacted to 24 cm within 1 month and 22 cm after 17 months.

The water level was maintained above the top of the tank using an external reservoir, and the pressure could be dropped to trigger ebullition by raising and lowering the reservoir. The rate of change of water level was limited to ~ 1 cm/min to avoid creating significant fluid flow into or out of the tank, which expanded and contracted by ≈ 12 mL per cm change in water level. Gas bubbles released from the sediments would rise through the overlying water, spread against the top plate, and slide towards the upslope corner due to a 9° tilt in the tank, in order to maintain a mostly bubble-free surface to detect subsequent arrivals. From the upslope corner, bubbles would rise through an outlet tube, in which they could be collected or vented into a fume hood.

The water level was recorded at 20 Hz using a Honeywell pressure transducer (24PCAF6D) and Dataq analog-digital converter, and the barometric pressure was recorded using a Solinst Levelogger at 5-minute intervals. The tank was lit from above on all sides with 8 LED light strips (2700K color temperature, 18 inches long, 5.9 W each), which were covered by green filters to inhibit photosynthesis. The system was housed in a darkroom to keep out external light for the sake of consistent imaging and inhibition of photosynthesis. Images were captured using an Allied Vision Technologies "Pike" scientific camera, mounted with a 25 mm f/1.4 lens. The camera was oriented horizontally, with the image reflected off of a tilted mirror, to

accommodate the narrow angle of view of the lens within the height of the room. The tilt of the camera and mirror were set with a frame of aluminum 80/20®. The camera was controlled using MATLAB to acquire images 3 times per second, with a resolution of 1200×960 pixels and 8-bit greyscale depth.

4.2.2 Image processing

Bubbles were identified automatically from images of the top of the tank in order to estimate their location and time of release, as well as their volume. Due to the mild slope and partial-wetting of the acrylic tank surface, small bubbles tended to become immobilized against the tank top so that a population many small bubbles appeared in any given image. The areal density and wide range of sizes of bubbles, random pixel noise from the camera, and relatively low resolution (0.04 mm) made it impossible to segment the individual images reliably. This fact, combined with the large population of bubbles that would have to be matched between successive images, made traditional particle-tracking algorithms impractical for analyzing the images.

However, because only location and time of bubble arrival against the top plate were of scientific interest, tracking the motion of bubbles towards the outlet was strictly unnecessary. Instead, we found that new arrivals could reliably be detected and distinguished from bubble motion by analyzing differences between successive images. Bubbles appeared as bright patches, so arrival of a bubble caused the brightness to increase, and disappearance of a bubble caused the brightness to decrease. The patches of increase and decrease in brightness were typically very sparse and distinguishable from the noise for bubbles larger than 2 mm in diameter. They were therefore readily identified using a clustering algorithm. In the case of bubble motion, a downslope decrease in brightness (disappearance) could be matched with an upslope increase in brightness (arrival), if the transition obeyed physically-based limitations on its speed, direction of motion, and fractional change in area.

The method proceeded as follows and is illustrated in Fig. 4-2:

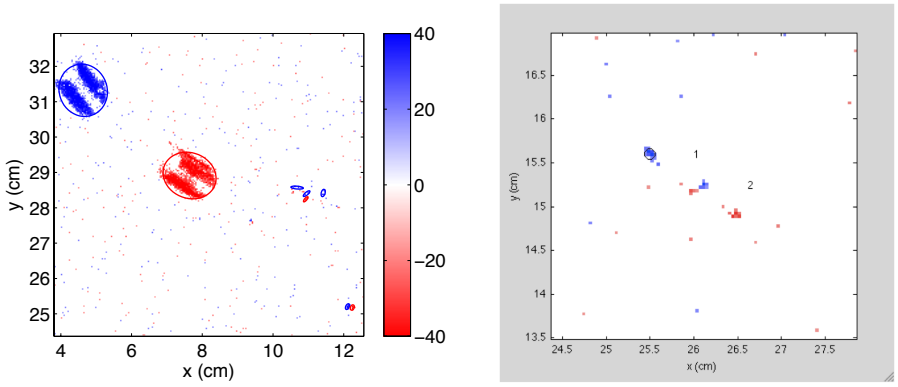

Figure 4-2: Left: Example of segmented image differences, with increases in brightness in blue and decreases in brightness in red. Clusters of pixels were identified with the DBSCAN algorithm [*Daszykowski et al.*, 2001], and the best-fit ellipse for each cluster was used to estimate the bubble area. Right: example of a situation where matching of bubbles is challenging because 2 bubbles may travel in parallel with relatively small speed (≈ 3 cm/s), so that the circled blue increase in brightness could reasonably be matched with the cluster of red pixels below the number 2. To minimize spurious assignment of new bubble arrivals, increases in brightness were only classified as new arrivals if they could not be matched with any decreases in brightness over the four previous images.

1. Subtract successive images to detect increases or decreases in brightness.

2. Separate increases in brightness (appearances) from decreases (disappearances), and for each:

3. Threshold the difference to find active pixels. For the setup described here, a threshold of 20 (out of 255 for 8-bit images) was used.

4. Identify bubbles by clustering using density-based scanning (DBSCAN, [*Daszykowski et al.*, 2001]), clusters of at least 5 pixels within a maximum separation of 3 pixels between any two. For the spatial resolution of 0.4 mm used here, this set a minimum detectable bubble diameter of ≈ 1 mm.

5. For each identified cluster, classify it as a new bubble arrival or motion of an existing bubble.

Bubbles were classified as new arrivals only if there were no disappearances downslope with consistent speed, direction, speed perpendicular to the upslope direction,

and fractional change in area. Differences over 4 successive observations ($\approx$ 1.3 sec) were searched to find potential motion matches. The determination of whether a pair of opposite-polarity changes could feasibly represent bubble motion was determined with a scoring system based on physically-based aspects of the putative motion (speed, direction, cross-slope speed, and fractional change in area). The scoring parameters were tuned empirically using a training data set of 1014 manually-classified changes (31 new arrivals).

Spatial precision

The accuracy of the location estimates is impacted by both the effectiveness of the image segmentation and the rate at which images were acquired. Bubbles rise vertically through the open water and then quickly transition to lateral (typically upslope) motion, so the location of a bubble in the first image where it is detected may be displaced in the upslope direction from the outlet location. Large bubbles also often appeared just before touching the tank top, as a faint bright spot in images (for example, this occurred for 66% of the largest 58 bubbles in Experiment 1). The locations of these below-tank-top bright spots are unaffected by the upslope migration so better represent the bubble outlet location than bubbles that had already hit the top and potentially proceeded upslope some distance before being imaged. The below-tank-top locations still do not perfectly represent bubble outlets because because bubbles larger than 4 mm in diameter rise in a wobble pattern with displacement on the order 1 cm [*Zeng and Cai*, 2014], but the error introduced by the wobble is isotropic. As a result, the locations of faint below-tank-top locations were compared against the locations of the first arrival against the tank top plate, for the largest 58 bubbles detected during Experiment 1, in order to estimate the magnitude of the error up-slope migration. The magnitude was found to be 2 ± 1 cm (mean$\pm$1 standard deviation, max 5.6 cm), and this represents an upper bound on the error because the sub-tank-top images were automatically identified as the original bubble location for 40% of these largest bubbles. This magnitude is comparable to the 1-cm resolution of the method and small enough that distinct hot-spots are still discernible.

Estimation of bubble volume from area

The volume of individual gas bubbles was estimated assuming that bubbles assume a static shape against the top plate. Bubbles with contact area smaller than the capillary length ($\kappa^{-1} = \sqrt{\gamma/\Delta\rho g}$)) take the shape of a spherical cap, and larger bubbles spread into a pancake shape with thickness $h = \frac{2}{\kappa}\sin\left(\frac{(\pi-\theta)}{2}\right)$ [*Queré*, 2005]. When the Bond number, $\mathrm{Bo} = (r\kappa)^2$, is in the range of 1 and for $\theta > 60°$, the bubble shape may be approximated as an ellipsoidal cap [*Lubarda and Talke*, 2011]. For an interfacial tension of 70 mN/m between methane and water [*Schmidt et al.*, 2007] and contact angle of 70 degrees for air and water on an acrylic surface [*Osti et al.*, 2009], it was found that the ellipsoidal model represented the bubble area-volume relationship not only in the transition between large and small bubbles, but also in the limits (Figure 4-3). Therefore, the ellipsoidal model was used to estimate all bubble volumes.

Because bubbles did not assume their equilibrium shape instantly, and because bubbles were sometimes imaged even before they hit the top, the initial bubble area tended to underestimate the equilibrium area. To compensate for this effect, the area of a bubble was measured using the last image that was matched by bubble motion with the initial arrival.

4.2.3 Validation against volume collection

A validation experiment was conducted in which the volume of gas released was estimated using both the automated image analysis and by collecting the gas that escaped from the tank. Gas was collected at the top of a water-filled tube and stored in glass syringes within 24 hr of release from the mud. Gas samples volumes were measured using glass syringes, and the chemical composition was analyzed on a F&M gas chromatograph with a Molecular Sieve 5a column and a thermal conductivity detector. Methane standards of 0%, 10%, 50% and 100% were used for calibration, and the standards fit a calibration line with $R^2 \geq 0.9968$ (Fig. 4-4).

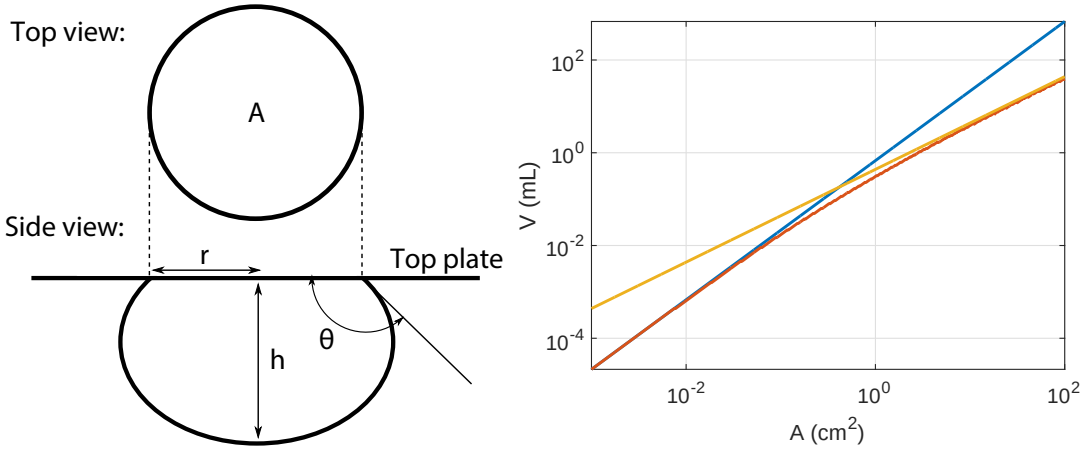

Figure 4-3: Left: diagram showing relationship between apparent bubble area A against the top plate (from above) and its height h, radius r and contact angle θ (from the side). Right: models showing bubble volume vs. apparent area for spherical caps (blue), ellipsoidal caps (red), and paddles (yellow). The ellipsoidal cap model was used for all bubble sizes in this study because it asymptotes to the two other models in the limit of large and small bubble sizes observed in the tank.

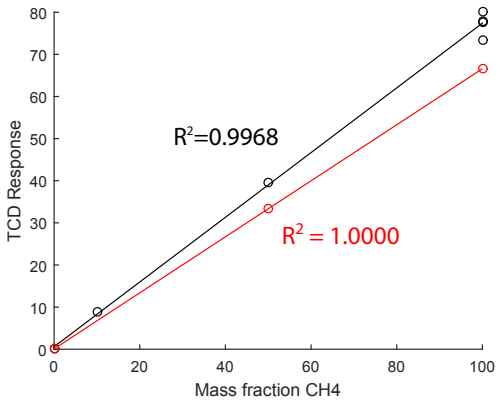

Figure 4-4: Calibration data for gas chromatograph thermal conductivity detector (TCD) used to analyze methane content of gas collected from the incubation tank. Two separated calibration runs were used to account for instrument drift over the $\approx$ 2 hour analysis period. 0% methane standards were used for both calibrations.

Table 4.1: Summary of imposed water level perturbations for the 5 experiments: durations and magnitudes of increase and decrease in water level (W.L.), as well as R^2 of flux vs. hydrostatic pressure (with the sign of R). For a time series showing the relative timing and duration of experiments, see Fig. 4-23

Exp. #	Dur. (days)	W.L. inc. (cm)	W.L. dec. (cm)	R^2
1	17	64	60	(-) 0.02
2	15	0	68	(+) 0.004
3	7	0	0	(-) 0.32
4	4	0	67	(+) 0.23
5	14	0	0	(-) 0.34

Estimation of fluxes

Bubble arrivals were binned into fluxes on a regular spatial grid and at regular intervals in time. The image collection system was occasionally non-operational, and for time intervals where the system was non-operational for less than 50% of the time, the flux was extrapolated in time to cover the entire interval. When the non-operation was longer than 50% of the time interval, the data were not used in calculating the flux.

The spatial distribution of ebullition was expected to be influenced by the edges, due to the tilted orientation of the tank and the influence of walls. Thus, data from within 4 cm of any edge of the tank were not analyzed, and data were only plotted from coordinates 4–41 cm in both directions.

4.3 Results

The methods presented above allowed a wide variety of observations about the nature of ebullition from natural, reconstituted sediments. Below we present chemical analysis of the released gas, evaluation of the accuracy of the image analysis method, estimation of the bubble size distribution, and characterization of the temporal and spatial variability in methane fluxes. Ebullition was observed during 5 experiments that were conducted over a period of 10 months between May 2015 and February 2016 (Fig. 4-23) and lasting between 4 and 17 days (Table 4.1).

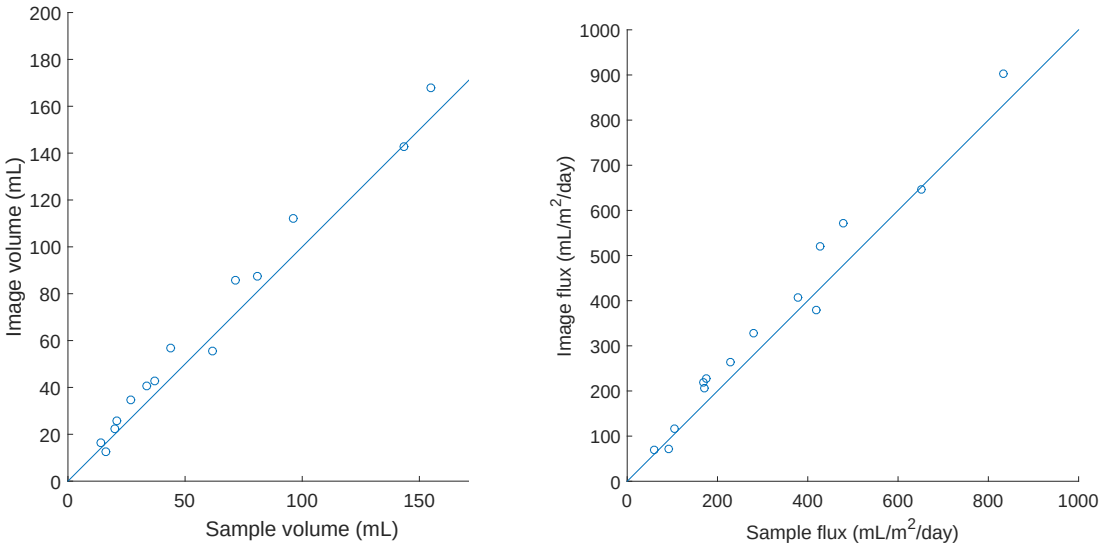

Figure 4-5: Comparison of gas fluxes measured with sampling of gas and image analysis shows strong predictive ability, with $R^2 = 0.983$ and 0.975 for correlations between sampled volumes (left) and fluxes (right). The shown 1:1 line is close to the slopes of best-fit lines, which were 1.04 and 1.05, respectively.

4.3.1 Gas content and flux magnitudes

Gas content

Gas samples from Experiment 5 were $83 \pm 5\%$ methane by mass ($n = 7$ after rejecting one sample with total components more than 100%). The oxygen concentrations were $0.6 \pm 0.7\%$ and are expected to have entered the bubbles via minor leakage in the collection tube or during gas sampling and storage. The nitrogen concentrations were $8 \pm 4\%$ and may have exsolved into the gas phase from the water in the collection tube, which was sparged with nitrogen to remove oxygen.

Flux validation results

The volume of gas released during Experiment 5 was collected over 14 time periods periods of duration 6-42 hours, and the volumes collected matched those estimated by image analysis within $20 \pm 10\%$ (mean relative absolute error $\pm$ 1 standard deviation). The best-fit line had a slope of 1.04 and $R^2 = 0.983$, showing that the image analysis method is unbiased (Fig. 4-5). For the fluxes, the best-fit line had a slope of 1.05 and $R^2 = 0.975$.

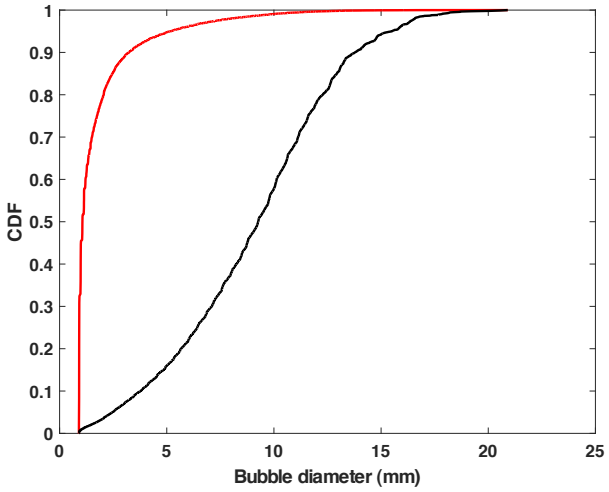

Figure 4-6: CDF of bubble diameters (red line) shows a population predominance of small bubbles bubbles, with those less than 2 mm comprising 79% of the bubbles by number. The small bubbles have minor impact on volume-weighted CDF (black line), constituting 3.3% of the total volume released.

Bubble size distributions

The distribution of bubble sizes estimated using the ellipsoidal cap method yields a distribution dominated numerically by bubbles smaller than 2 mm in diameter (Fig. 4-6). Although these bubbles constitute 79% of the bubbles by number, they contribute only 3.3% of the total volume released. The frequency of such small bubbles is large compared with other estimates of the BSD in UML, which found $< 1\%$ smaller than 2 mm in diameter [*Delwiche et al.*, 2015]. Part of that discrepancy may be attributed to a lower detection limit for bubble sizes for the instrument used in that study, as bubbles smaller than 2 mm in diameter were not tested in the calibration of the device.

The difference between our results and those found in the field may be attributed to bias in the method used for analysis of image from the incubation experiment. Small bubbles are over-represented in the image analysis because moving bubbles smaller than 3-4 pixels (1.1-1.5 mm) in diameter are much more likely to be mis-identified as first arrivals. This happens when one of a matched pair of changes associated with motion (downslope disappearance and upslope appearance) is not detected, usually

because it has too few pixels with magnitude larger than the threshold for noise rejection. The probability of non-detection is much higher for bubbles comprising few pixels compared with the minimum cluster size (5). To enhance the likelihood of finding a later match, bubbles were matched across up to 4 successive images.

4.3.2 Episodicity of methane venting

Hydrostatic control of ebullition

The 5 experiments reported here were conducted under different conditions of hydrostatic pressure control: Experiments numbers 1, 2 and 4 were forced by large drops in hydrostatic pressure, 1 included a period of raised hydrostatic pressure, and Experiments 3 and 5 were left to respond to barometric pressure variations (Table 4.1).

Experiment 1 was carried out in 3 phases of water level control: an initial period of low water level until May 7, 15, an intermediate period of raised water level until May 10, 15, and a final period with low water level again (Fig. 4-7). Prior to the experiment, the water level had been lowered by 45 cm on May 1, 15, and in the week before that the level was cycled down and up by 38 cm. These perturbations were large and frequent relative to those observed in the water level of Upper Mystic Lake [*Scandella et al.*, 2011]. While the pre-experimental ebullition was not observed with the video system, a rough estimate based on the change in volume of the contents of the tank suggests that $\sim$ 600 mL of gas was released during the 12-day period preceding Experiment 1, corresponding to a flux of $\sim$ 0.03 mL/m2/day, which was typical for low-flux periods from the tank.

During the initial phase, the flux remained relatively low, rising only to about 0.2 mL/cm^2/day. After the water level was raised by 64 cm, the flux dropped below 0.01 mL/cm2/day within 1 day and remained that low until the water level was dropped again on 5/10. With the resumption of low-pressure conditions, the flux immediately jumped back up to above 0.1 mL/cm2/day and peaked to above 0.4 ml/cm2/day on 5/11/15. For the remainder of the experiment, the water level was maintained while barometric pressure variations caused the pressure to dip by

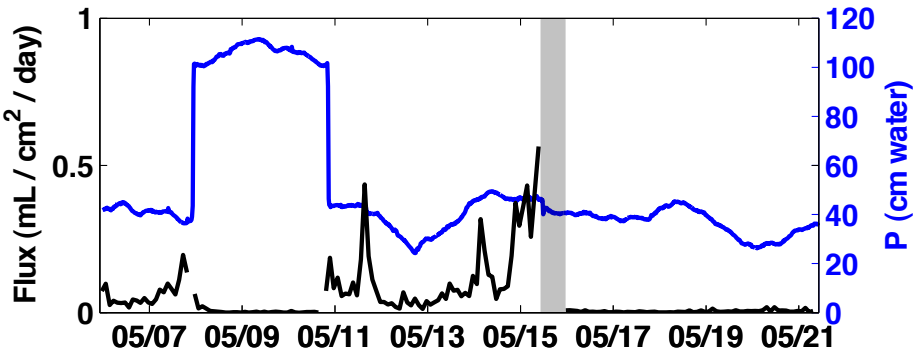

Figure 4-7: Time series of flux and hydrostatic pressure for Experiment 1. The gray bar from 12 PM–11 PM on May 15 represents a period when the data were unusable because suspended sediment became attached to the regions on the top of the tank and occluded the view of arriving bubbles.

$\approx$ 20 cm on 5/12–13 and again from 5/19–21. Following the initial peak on 5/11, the flux grew gradually from 5/13–15, culminating in an ebullition event that was so vigorous that it suspended sediments that became temporarily adhered to the top of the tank and significantly occluded the camera's view of rising bubbles. The period from 11:39 AM to 11:00 PM on 5/15 was excluded from the data analysis because the images could not be reliably analyzed to identify the arrival location and time of bubbles. Following this period of intense activity and after the sediment had detached from the tank top, the flux was maintained at below 0.1 mL/cm2/day for the remainder of the experiment, even during the pressure drop from 5/19–21.

Experiment 2 was driven by a 68 cm drop in water level on 6/17, following a 27-day period where the water level was maintained at a high level intended to inhibit ebullition while sediments recharged their gas contents (Fig. 4-8). After the water level was lowered, it was maintained for the remainder of the experiment so that pressure changes reflect barometric changes, which were of magnitude $\approx$ 20 cm. The gas flux peaked within 2 hours of the drop in hydrostatic pressure and then decayed to the background rate over the following 3 days. For the remainder of the experiment, the gas flux remained below 0.25 mL/cm2/day but showed minor peaks during 3 periods of low hydrostatic pressure.

Experiment 3 was carried out at a constant water level and following an extended

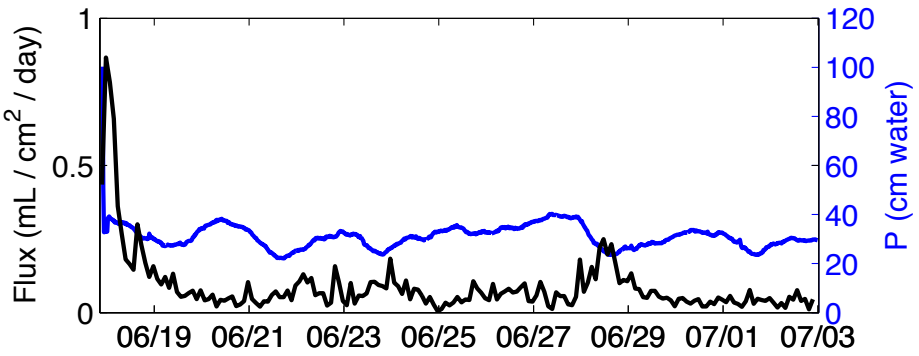

Figure 4-8: Time series of flux and hydrostatic pressure for Experiment 2.

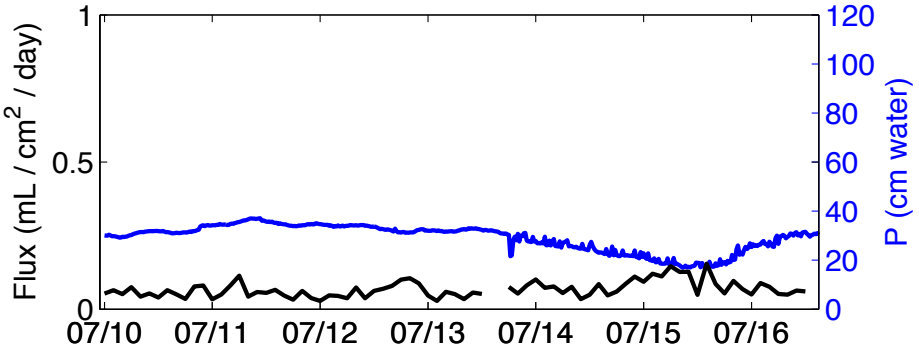

Figure 4-9: Time series of flux and hydrostatic pressure for Experiment 3.

period at that same level imposed during Experiment 2 (Fig. 4-9). The gas flux remained below 0.25 mL/cm2/day but showed a consistent, slow increase over a multi-day drop in hydrostatic pressure from 7/13–7/15 and then a decrease as the hydrostatic pressure rose again.

Experiment 4 was carried out under similar conditions to Experiment 2, beginning with a 67-cm drop in water level and then leaving the level constant for the remainder of the experiment (Fig. 4-10). The gas flux peaked at 0.7 mL/cm2/day immediately and decayed over the following day to a roughly constant level $\approx$ 0.1 mL/cm2/day.

Experiment 5, like Experiment 3, was carried out at a constant water level and following an extended period at that same level (Fig. 4-11). The barometrically-driven pressure variations were of a larger magnitude (50 cm vs 20), but the magnitude of the fluxes showed a similar response to Experiments 2 and 3, peaking at 0.2 mL/cm^2/day at the lowest hydrostatic pressures.

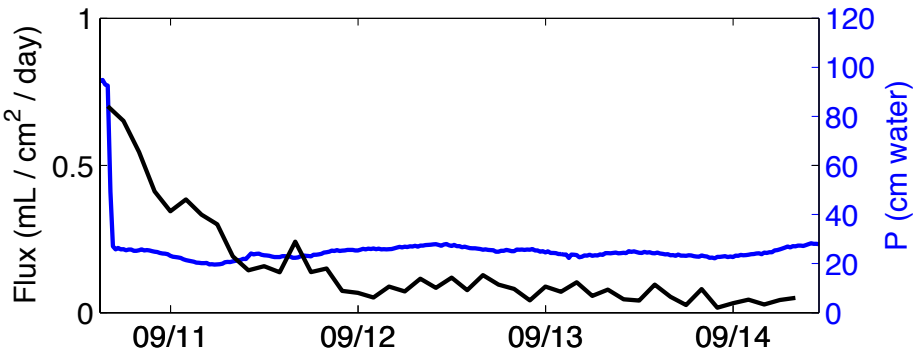

Figure 4-10: Time series of flux and hydrostatic pressure for Experiment 4.

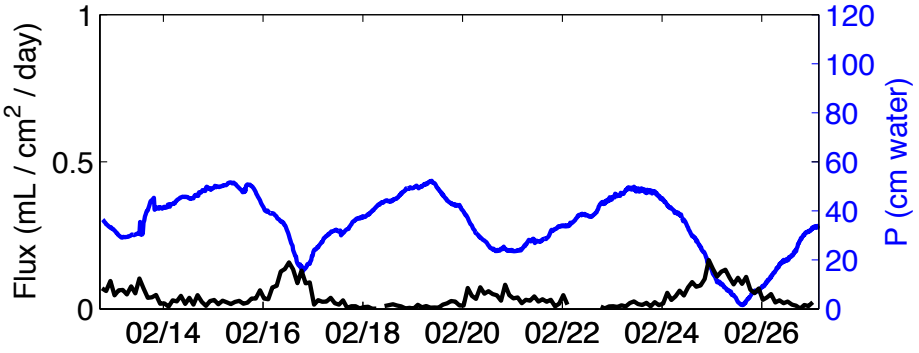

Figure 4-11: Time series of flux and hydrostatic pressure for Experiment 5.

Temporal clustering

The temporal relationship between successive bubble releases can be characterized by the distribution of inter-arrival times, τ. Events that occur independently in time may be modeled as a Poisson process, and temporal clustering or regularity may be detected as deviations of the PDF $f(\tau)$ from that expected from a Poisson process. Especially useful for making this comparison is the hazard function, $h(\tau)$, which quantifies the probability of an event occurring, conditioned on a given amount of time having passed since the last event:

$$h(\tau) = \frac{f(\tau)}{1 - F(\tau)}, \tag{4.1}$$

where $F(\tau)$ is the cumulative density function (CDF) [*Stapelberg*, 2009]. For a Poisson process, events are independent and have uniform probability, corresponding to con-

stant h since the events have no memory of previous arrivals. For a Weibull process—a model often used in reliability engineering to model component failures—the hazard function is a power law, $h(\tau) = (\beta/\lambda)(\tau/\lambda)^{\beta-1}$, where β and λ are the shape and scale parameters, respectively. A decreasing power law ($\beta < 1$) corresponds to strong temporal clustering, while an increasing power law ($\beta > 1$) is associated with more regularly periodic arrivals [*Stapelberg*, 2009].

For the analysis presented here, each bubble's contribution to h is weighted by its volume, so that $h(\tau)$ properly represents the rate of volume flow per the volume not yet released after τ (see Appendix A). This was important for the analysis of this experiment because the method of matching image changes to identify bubble motion (as opposed to arrival of a new bubble) was poor for bubbles smaller than ≈ 1.1 mm (or 3 pixels) in diameter, so small, moving bubbles could create the appearance of more frequent arrivals. Analysis of the BSD showed that these bubbles constituted over 50% of the bubbles by number but less than 3% by volume (Fig. 4-6), so weighting each bubble's contribution to h by its volume minimized the impact of any artifacts on the statistics.

For the combination of all experiments, $h(\tau)$ for 3-cm pixels shows power-law decay with slope -0.4 ± 0.1, consistent with a Weibull process with $\beta = 0.6 \pm 0.1$ (Fig. 4-12). For coarse pixels (the entire area), h also decays as a power law with slope -0.4 for $\tau < 2$ min and then decays more rapidly.

Comparing the hazard function between the 5 experiments yields some insight into the relationship between hydrostatic triggering and temporal clustering (Fig. 4-13). Experiments 1, 2, 4, and 5 are qualitatively similar, except for a dip in the hazard for coarse pixels in Experiment 1 from $\approx$ 5–15 min, indicating that temporal clustering tended to occur over inter-arrival times shorter than 5 minutes over the entire tank area. This does not suggest that the duration of temporal clusters was limited to 5 minutes but instead suggests that some process primarily tended to cause subsequent ebullition within that timeframe. Because Experiment 1 was the only one to display periods of prolonged quiescence, it is tempting to attribute this result to that influence, but the quiescent periods likely contributed only a small portion of

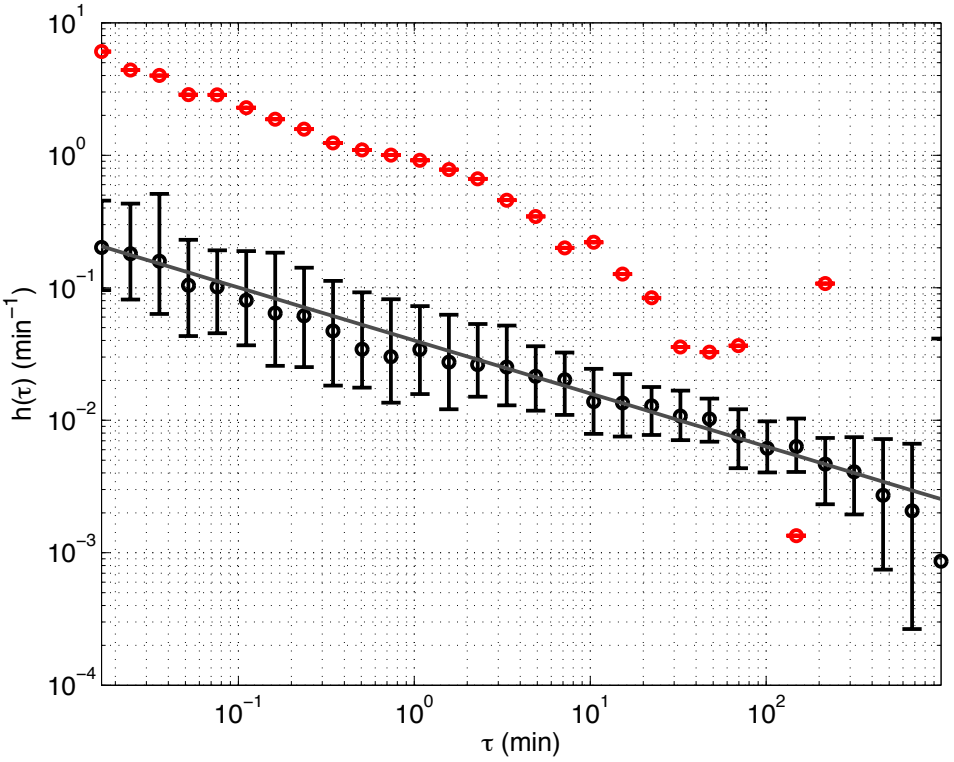

Figure 4-12: Hazard function over all experiments at 2 different spatial resolutions (3 cm, black and 37 cm, red). For the fine-resolution pixels, $h(\tau)$ shows power-law decay with a slope of -0.4 (gray line). Within the interquartile range across pixels (black bars), the decay can be fit by a power law of slopes between -0.3 and -0.5 (not shown). This decay is consistent with temporal clustering from a Weibull process, with $\beta = 0.6 \pm 0.1$. For the coarse-resolution data (over the entire viewing area), h shows power-law decay with a similar slope for $\tau \leq 2$ min, and then it decays faster. The larger magnitude is due to the increased rate of arrival over the larger observation area. The large oscillations for $\tau \geq 100$ min is due to the small number of measured inter-arrival times longer than that at the scale of the entire tank; in other words, the tank was rarely totally inactive for more than an hour.

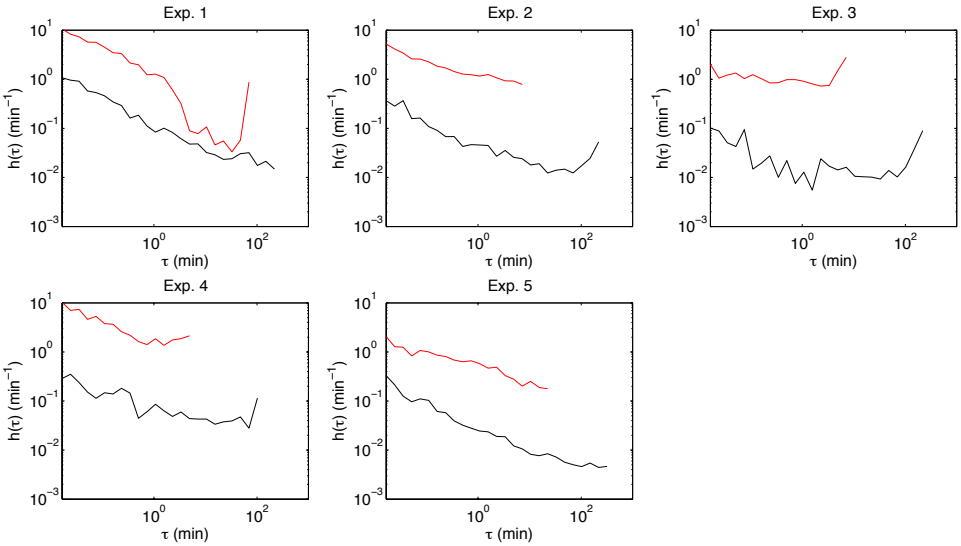

Figure 4-13: Hazard function for Experiments 1 through 5, reading left to right, top then bottom as subfigures. Red lines for the entire observation area and black lines for 3-cm pixels.

the bubble volume and represented very long τ. The rebound of h around $\tau = 60$ min suggests relative regularity of arrivals at this timescale.

Compared with Experiment 1, Experiment 2 shows slightly shallower decay in its coarse h, indicating a slightly stronger role for independent arrivals over dependent triggering. Experiment 3 shows near-Poisson behavior of the coarse pixel, and for fine pixels with $\tau \geq 1$ min, suggesting that the bubble releases were relatively independent and not self-sustaining. This may be related to the depletion of the stored gas during Experiment 2. However, Experiment 4 also displayed shallower decay in h for both coarse and fine pixels for $\tau \geq 1$ min, and that experiment was carried out without a preceding experiment that would deplete it, and it showed a strong flux response to the hydrostatic pressure drop.

The maximum observable τ is limited by the duration of the uninterrupted periods of image collection, whose histogram reflects the fact that only 17 periods lasted longer than 1 day (Fig. 4-14). The imaging was interrupted by sample collection, cleaning of the imaging surface, switching hard drives for recording images, or any change in light away from the tank indicating the darkroom had been opened. Future

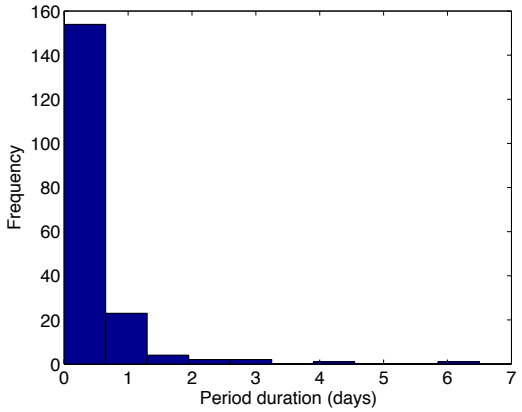

Figure 4-14: Histogram of durations of continuous periods of image collection shows that the majority of periods lasted < 1 day.

experimental design efforts should aim to minimize these breaks in data collection, to enable analysis of long inter-arrival times.

4.3.3 Spatial heterogeneity of methane venting

Gridded flux maps

The spatial distribution of fluxes varied significantly among experiments. For Experiments 1 and 2, the composite flux map over the experiment shows approximately 10 clusters of connected pixels with the highest fluxes, each spanning 2–5 pixels in diameter (Fig. 4-15). Experiment 3 shows a few pixels with high flux, but they do not exhibit the degree of connection and spatial order evident in the first 2 experiments. Experiment 4 also shows connected clusters with high fluxes, but they are much more numerous and more densely-spaced. Experiment 5 shows lower fluxes overall and much more spatial homogeneity, though some of that appearance arises from the use of the same color scale for all subfigures.

Within each experiment, the spatial pattern of ebullition showed variability over the scale of days. Within a given day for Experiments 1 and 2, the spatial pattern was dominated by 5–10 clusters of connected pixels, each 2–5 cm in diameter (Figs. 4-16 and 4-17). During Experiment 1, there is repeated use of multiple outlets ~ 5 cm up and left from the center of the tank, as well as repeated use of an outlet in the

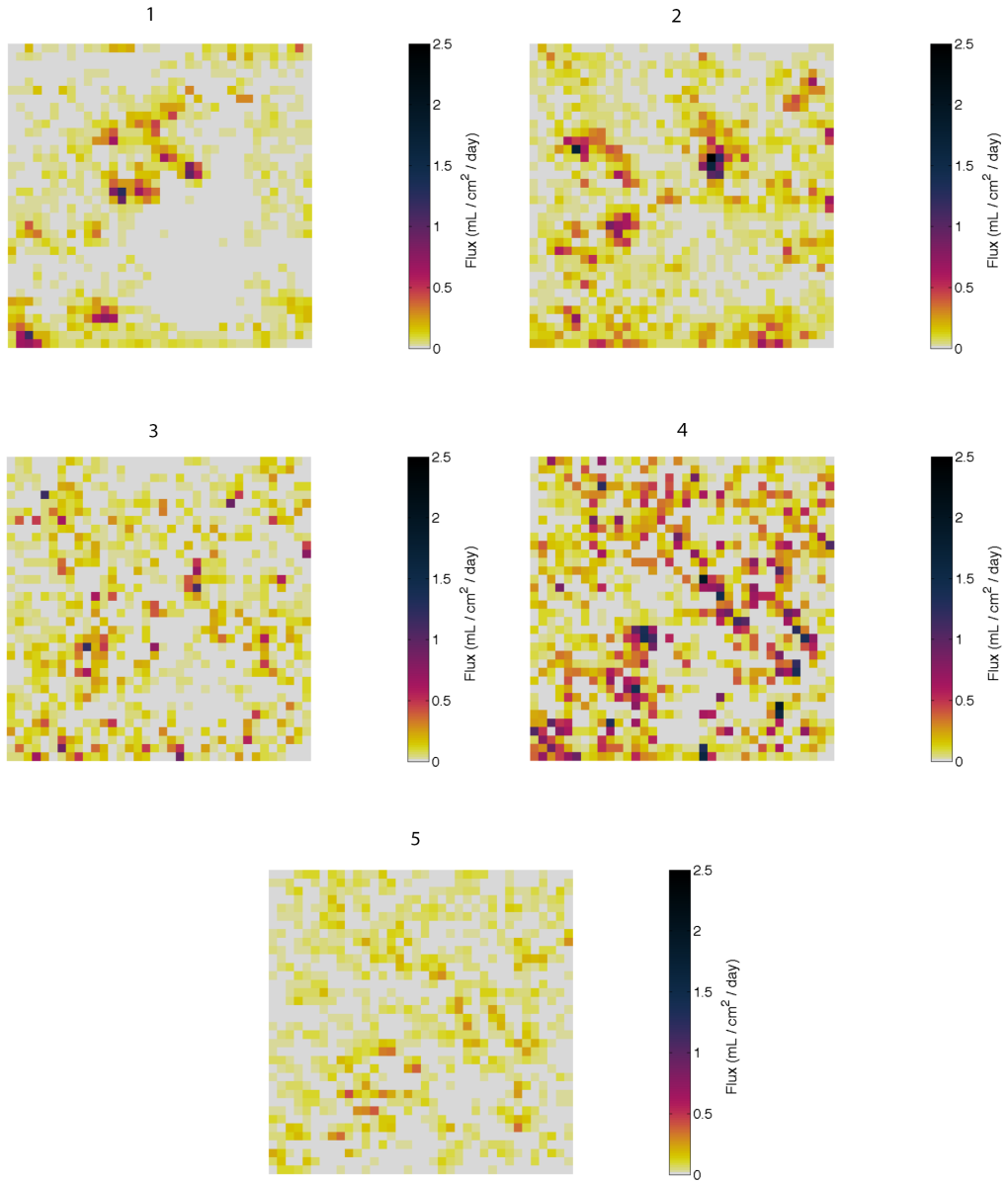

Figure 4-15: Composite flux maps from each of the 5 experiments.

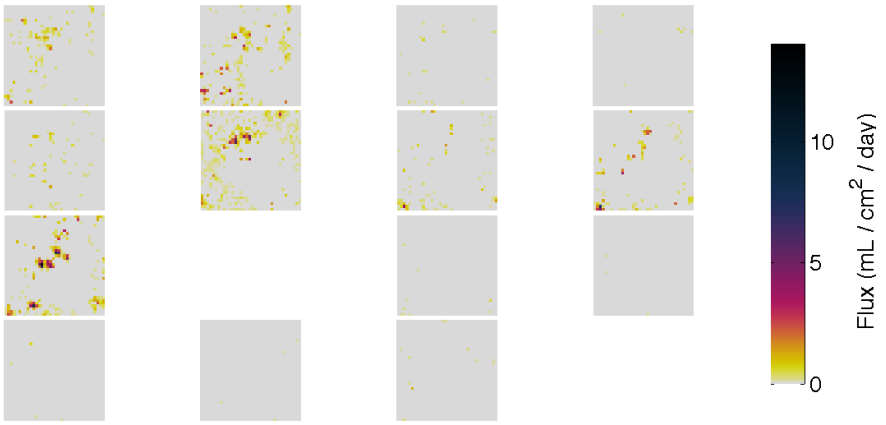

Figure 4-16: Calendar of daily ebullitive flux maps from Experiment 1, from May 5–21, 2015. Each square is 37 cm on a side with resolution of 1 cm. Day-long samples do not start at midnight and are not shown if the images were being collected during $< 50\%$ of the period.

bottom-left corner. During Experiment 2, the outlet just up and to the right of the center becomes active on day 1 and is re-used on days 5–8 and 9–11. The rest of the outlets appear to go dormant after the initial high-flux period.

For Experiments 3, 4, and 5, the daily venting was more spatially-distributed, with 20–100 clusters of active pixels contributing most of the flux (which was $<$ 6 mL/cm2/day, small compared with the up to 25 mL/cm2/day within the active pixels during Experiments 1 and 2) (Figs. 4-18, 4-19 and 4-20). It is difficult to ascertain re-use of such dense, small features across days from this calendar view, so we analyze the spatial clustering and its persistence statistically with the radial distribution function.

Spatial clustering

We analyze the size, intensity, spacing and persistence of spatial clusters using the radial distribution function (RDF), which quantifies the degree of spatial concentration of events at a given distance from other events, relative to a completely spatially random (CSR) process. Values of $g(r) > 1$ indicate spatial clustering at inter-point distance r, while values $g < 1$ indicate spacing or regularity, a lower-than-expected density of points at range r. The results from all 5 experiments show short-range

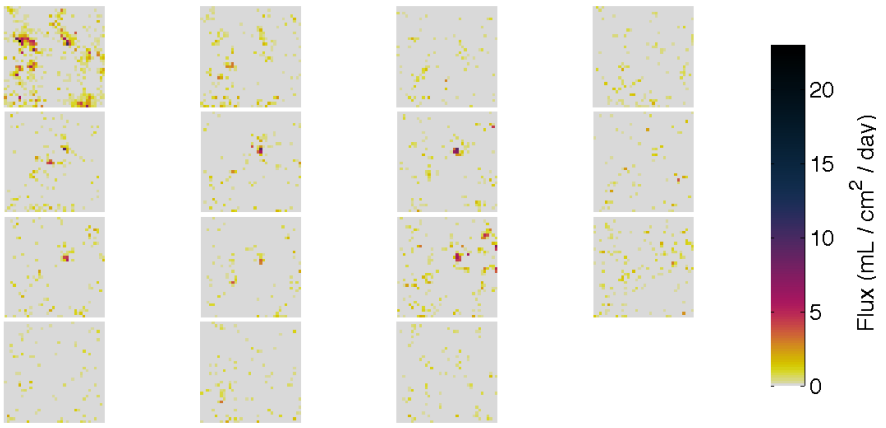

Figure 4-17: Calendar of daily ebullitive flux maps from Experiment 2, from June 17–July 3, 2015. Each square is 37 cm on a side with resolution of 1 cm. Day-long samples do not start at midnight and are not shown if the images were being collected during $< 50\%$ of the period.

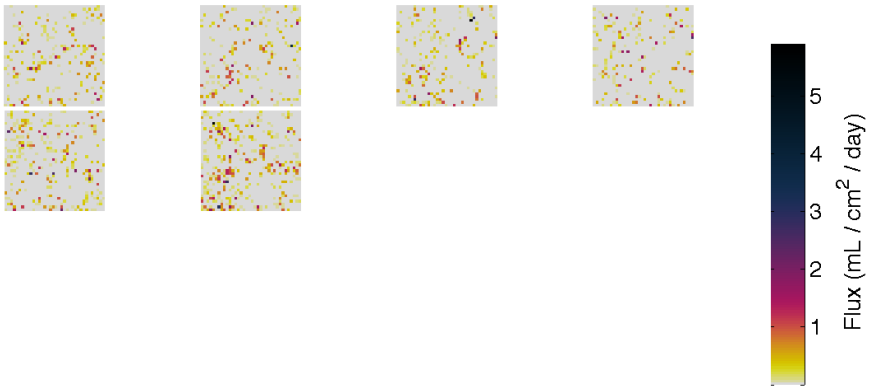

Figure 4-18: Calendar of daily ebullitive flux maps from Experiment 3, July 10–16, 2015. Each square is 37 cm on a side with resolution of 1 cm. Day-long samples do not start at midnight and are not shown if the images were being collected during $< 50\%$ of the period.

Figure 4-19: Calendar of daily ebullitive flux maps from Experiment 4, September 10–14, 2015. Each square is 37 cm on a side with resolution of 1 cm. Day-long samples do not start at midnight and are not shown if the images were being collected during $< 50\%$ of the period.

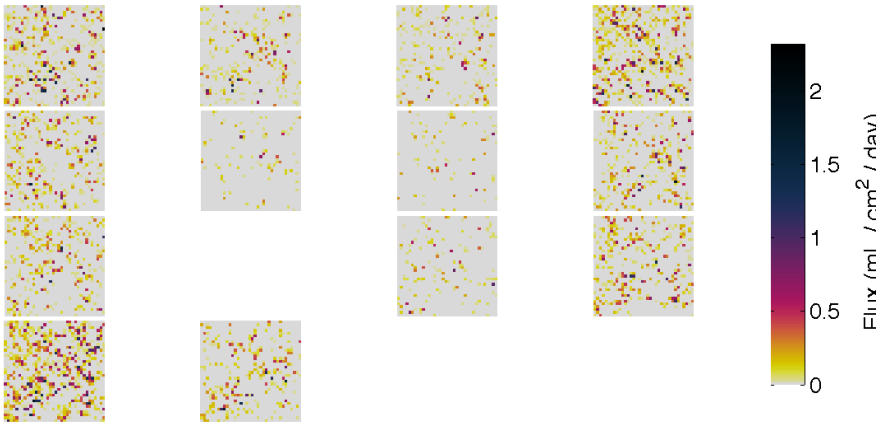

Figure 4-20: Calendar of daily ebullitive flux maps from Experiment 5, February 12–27, 2016. Each square is 37 cm on a side with resolution of 1 cm. Day-long samples do not start at midnight and are not shown if the images were being collected during $< 50\%$ of the period.

clustering and long-range spacing, though they differ in the distance of crossover between clustering and spacing and the timescale over which the spatial signal decays (Fig. 4-21).

Experiments 1 and 2 show strong short-range clustering, although the clusters are larger in size in Exp. 2 ($g > 1$ for $r \leq 6$ for 15-minute samples in Exp. 1 and for $r < 3$ over the same duration in Exp. 2). Beyond that range, both show spacing of activity with $g < 1$. For progressively longer-duration samples, the strength of clustering and spacing decay roughly monotonically, except that the size of the clusters increases with time up to 10 cm in Exp. 1 and 7 cm in Exp. 2. Even over 2 days, the spatial clusters still remain strong with $g > 3$ at $r = 1$ cm, and this is consistent with the visible role of clusters in the composite maps for these Experiments (Fig. 4-15).

Experiments 3–5 also show short-range clustering and long-range spacing over short duration samples, but the crossover range is shorter and roughly constant, and the strength of the spatial signature decays more completely with longer samples. The crossover range for 15-minute samples is between 2.5 and 4 cm, and with longer samples it does not appear to increase significantly (except in Experiment 5, where it may rise to 6 cm). The shorter crossover distance between clustering and spacing in the RDF for Experiments 3–5 than for Experiments 1 and 2 is consistent with the qualitative observation of a more significant role for large, distant outlets in the first 2 experiments (Fig. 4-15). The RDF also decays towards 1 over longer samples, with $0.9 < g < 2$ for samples longer than 1 day.

Another tool for investigating the fine-resolution spatiotemporal relationship between bubbling events is the spatio-temporal radial distribution function (ST-RDF). This statistic extends the concept of the RDF $g(r)$ into time with the introduction of time lags u between events, so that $g(r, u)$ is the amount of activity within the ring of radius r around an event and following it by time lag u. The metric is computationally intensive to estimate over long-duration samples required to investigate large u, but for short times it can confirm the presence of spatiotemporal clustering more precisely than using the RDF over short time intervals.

For Experiment 1, the ST-RDF showed clustering typically strongest for $r \leq$

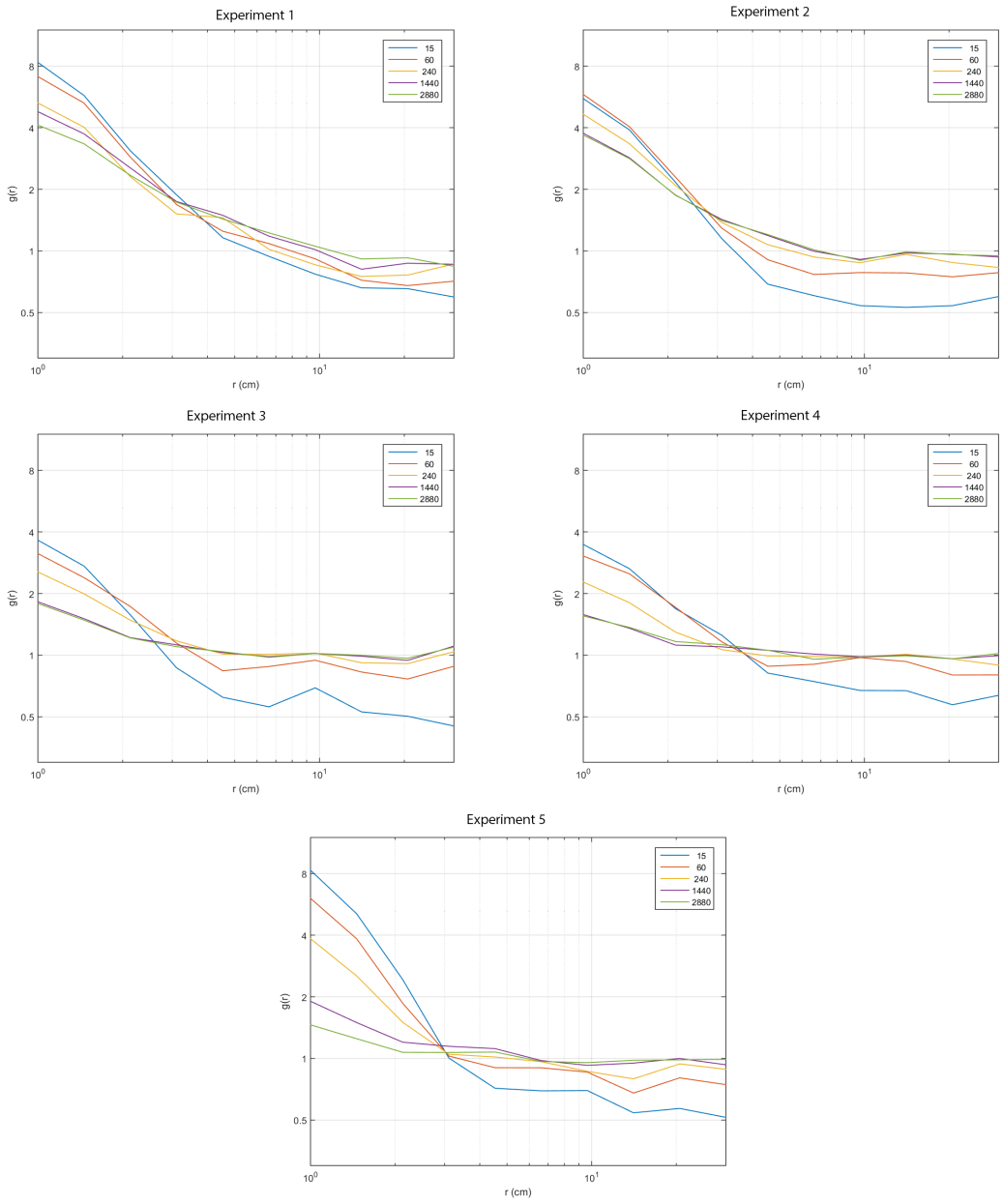

Figure 4-21: Radial distribution functions for Experiments 1–5.

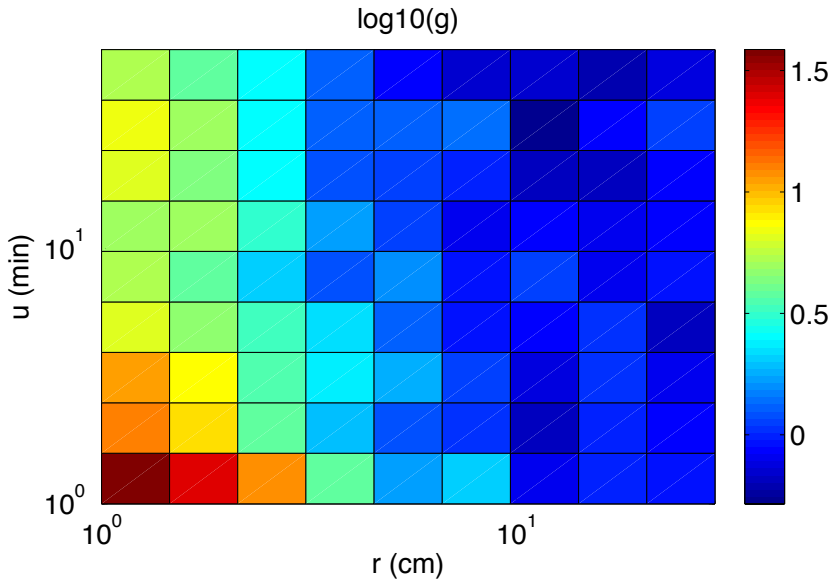

Figure 4-22: Spatiotemporal RDF for Experiment 1. Note the logarithmic color scale. The strong spatiotemporal clustering for $r \leq 3$ cm and $\tau \leq 2$ min suggests that ebullition episodes are often compact in space and time, although significant activity within a spatial cluster can persist even following breaks of at least 2 hours. Other experiments showed qualitatively similar behavior.

3 cm and $\tau \leq 2$ min (Fig. 4-22). The spatial scale matches the observed RDF for Experiment 1, but the temporal scale is much smaller than that of the RDF for temporally-combined samples up to 1 day. The fact that the spatial clustering appears to dissipate faster indicates that most of the activity happens within a relatively short amount of time, even though the presence of the spatial clusters continues to dominate for long after. In a sense, the ST-RDF indicates the timescale of clustered activity, while the comparison of RDFs for samples of different durations (Fig. 4-21) indicates the timescale for de-clustering, when the clustered signal becomes overwhelmed by other events.

The patterns of ebullition may be simplified and compared between experiments by automatically defining the major active outlets for each experiment, then plotting these outlets for all experiments on the same axes (Fig. 4-23). Outlets were defined as clusters of adjacent pixels each with flux above the 95^{th} percentile of activity for that experiment. The map shows some locations of apparently enhanced activity, and the RDF confirms that the mild short-range spatial clustering is nonetheless significant

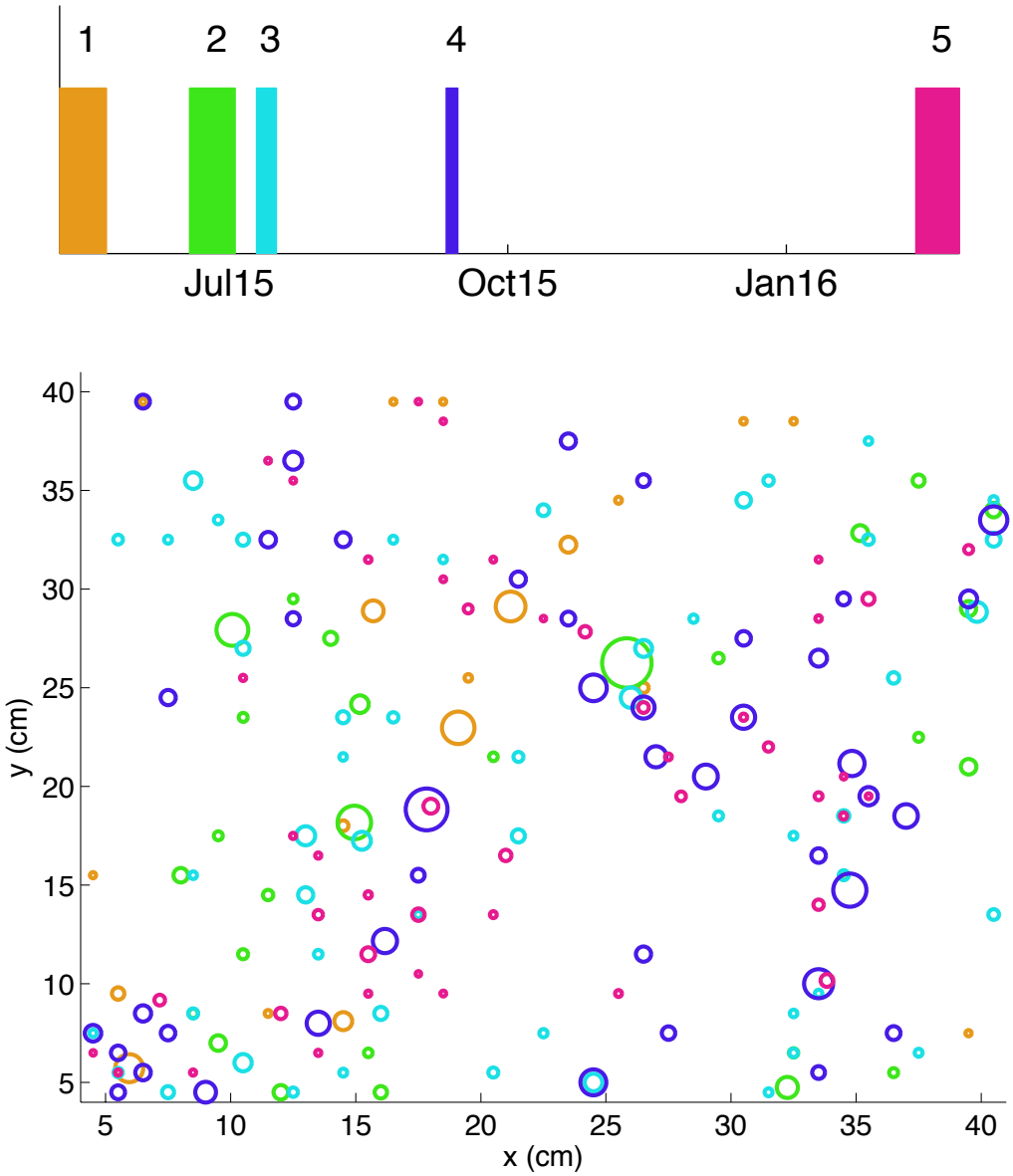

Figure 4-23: Top: time series of experimental observations. Bottom: Map showing locations of hot-spot outlets from all Experiments. The area of each circle is proportional to the mean flow rate through that outlet over its respective experiment, and the color of each circle reflects the experiment during it occurred, corresponding to the top subfigure.

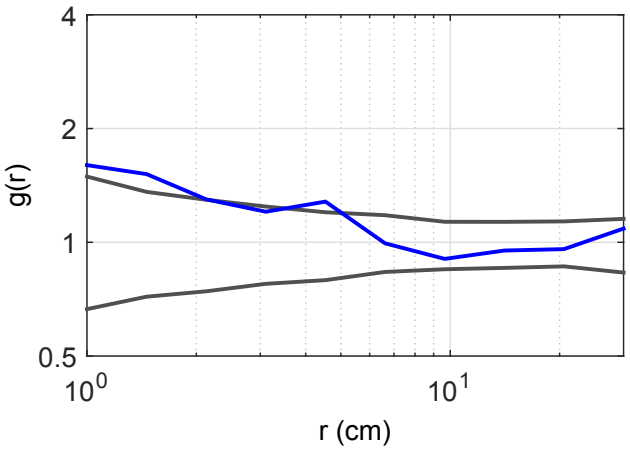

Figure 4-24: RDF of major outlets over all experiments (blue) shows mild short-range clustering ($g > 1$ for $r \leq 6$ cm). Some regions appear to host enhanced activity, such as $(x = 26, y = 26)$ and $(x = 6, y = 6)$. The spatial clustering that characterizes this activity is significant relative to 95% confidence bounds for a CSR process (gray) for $r < 2$ cm and $r \approx 4$ cm, meaning that the clustering likely arises from a non-CSR process. The CSR process was simulated with 500 Monte Carlo replicates, and the grey lines represent the 2.5^{th} and 97.5^{th} percentiles.

for $r < 2$ cm and $r \approx 4$ cm when compared with the 95% confidence bounds for a CSR process (Fig. 4-24, CSR simulated with 500 Monte Carlo replicates [*Wiegand and Moloney*, 2014]). Therefore, major outlets show mild but significant re-use over the scale of months.

Discretization of the major outlets for each experiment also enables further characterization of the experiments (Table 4.2). Consistent with the qualitative observation from the composite flux maps (Fig. 4-15), Experiments 1 and 2 had significantly fewer outlets and therefore larger effective spacing between the outlets than the later 3 experiments. The outlets still released a similar fraction of the total gas flux ($\geq 34\%$) compared with the overall range (27–39%).

Table 4.2: Summary of the role of major outlets identified for each of the 5 experiments, including the number of outlets, the equivalent spacing between them, and the fraction of the volume flux for the experiment that was release through those outlets.

Exp. #	Number of outlets	Equivalent spacing (cm)	Flux fraction (%)
1	19	8.5	39
2	28	7.0	34
3	54	5.1	37
4	43	5.6	32
5	45	5.5	27

4.4 Discussion

4.4.1 Flux magnitudes in lab and field scales

The long-term spatiotemporal average flux from the experiment was approximately 0.6 mL/cm^2/day, or 600 mL/m^2/day. This value is large compared with the mean ebullitive flux from the sonar deployments in 2012, 10 mL/m^2/day. The majority of the experiments were carried out with hydrostatic triggering of ebullition following a period of high water level to inhibit ebullition and allow a buildup of stored gas in the sediments, which likely increased the fluxes during the experiments relative to the long-term average. A more appropriate comparison, then, is with the average flux during high-flux events from the sonar record (defined as having a spatial mean flux above the long-term average, with 20-minute binning). These high-flux events had an average of 30 mL/m^2/day, which is larger but still 20 times smaller than the fluxes from the incubation experiment.

The discrepancy may be explained with a combination of factors increasing the flux in the tank and potential underestimation of flux by the sonar. The increased rate of ebullition in the tank may be attributed to a combination of higher temperature for incubation ($20 - 22^\circ$ C in the laboratory vs. $4 - 6^\circ$ C in the hypolimnion of UML), increased availability of organic matter and a more uniform depth profile of methanogenesis due to reconstituting of the sediments. The sonar may also underestimate fluxes due to limitations in sensitivity to small bubbles, though those did not contribute significantly to the flux in the tank (Fig. 4-6). The sonar signal could also

underestimate the flux if the method of rejecting anchor signals spuriously rejected strong bubble events, though a validation dataset indicated that the sensitivity of the method (fraction of bubble volume identified as bubbles, not anchors) was above 99% (Section 2.2.5).

4.4.2 Hydrostatic control

The spatially-averaged time series for the 5 experiments show that high or rising hydrostatic pressure inhibits ebullition and low or falling pressure triggers it, when the sediments are not depleted of gas. Episodes of enhanced ebullition appeared to be triggered by rapid drops the water level in Experiments 1, 2 and 4, as well as by more gradual drops in the barometric pressure in Experiments 2, 3 and 5 (and potentially 1). The magnitude of the flux increase was roughly proportional to the magnitude of the barometric pressure decreases in Experiments 2, 3 and 5, however even in these cases the correlation between hydrostatic pressure and flux remained below $R^2 = 0.34$ (Table 4.1). In Experiments 1, 2 and 4, with imposed changes in water level, the negative correlation was smaller than 0.03, and it was even positive in Experiment 4. Therefore, the relationship between flux and hydrostatic pressure is clearly nonlinear, consistent with previous analyses [*Scandella et al.*, 2011].

One aspect of the nonlinearity is a delay between drops in hydrostatic pressure and the onset of enhanced ebullition. The onset of ebullition after hydrostatic pressure drop is typically shorter than 2 hours. For the case of slow, barometrically-driven drops, the flux typically increases immediately (relative to the 2-hour resolution plotted in Figs. 4-7–4-11) in Experiments 2, 3 and 5. Large, rapid drops in the water level also appear to trigger ebullition within 1–2 hours in Experiments 2 and 4, and to a lesser extent in Experiment 1. However, there are also examples of peaks in ebullition that occur significantly after the drop in hydrostatic pressure. In Experiment 1, the 0.4 mL/cm2/day peak on 5/11 begins approximately 1 day after the large water level drop (Fig. 4-7). The later series of increasing-magnitude peaks also begins more than a day after the onset of falling barometric pressure on 5/11. These delays may be caused by slow gas migration from deep within the sediments, or they may reflect

enhanced strengthening of the sediments in some cases that requires a particularly large perturbation to jostle the system out of its stable state. In the case of the gas flux from 5/13–5/15, the increase in flux begins at the nadir of a barometric pressure drop, and that pressure may have provided the required stress to begin a cascade of growing ebullition events that triggered subsequent bubble mobility.

The role of hydrostatic pressure appears mediated by the presence of gas within the sediments. During Experiment 1, an extended period of intense ebullition ($\geq$ 0.2 mL/cm2/day for $>$ 1 day) was followed by a continuous period of quiescence ($\leq$ 0.02 mL/cm2/day for $>$ 6 days). This quiescence persisted even during a $>$20 cm drop in hydrostatic pressure, which was large enough to trigger ebullition events in Experiments 2, 3, and 5 (and perhaps in 1). The inability to trigger ebullition even with a significant hydrostatic pressure drop suggests a second control on ebullition, and the most intuitive control given the preceding high-flux episode is that the sediments had been depleted of gas.

The demonstration of hydrostatic control of ebullition is consistent with previous observations at the field scale [*Strayer and Tiedje*, 1978; *Martens and val Klump*, 1980; *Kuipphet and Martens*, 1982; *Chanton et al.*, 1989; *Fechner-Levy and Hemond*, 1996; *Tokida et al.*, 2007; *Torres et al.*, 2002; *Yamamoto et al.*, 2009; *Varadharajan and Hemond*, 2012]. However, these field observations were reported under natural conditions and did not impose hydrostatic pressure changes under controlled laboratory conditions. Our results are also consistent with a mechanistic model explaining how the hydrostatic forcing is mediated by the effective stress [*Scandella et al.*, 2011]. However, the richness of this new dataset provides a basis for a more detailed understanding in a number of ways. For example, the clear anti-correlation between gas flux and hydrostatic pressure in Experiments 2, 3 and 5 suggests that even barometric pressure changes on the order of 20 cm can control the rate of ebullition in a sustained fashion. This is important because the conduit dilation model assumed that gas was released instantly (on the daily scale) when the hydrostatic pressure dropped to a level sufficient to trigger mobilization. If that model was to be used to explain these results, then explaining the continued venting would require additional

mechanisms such as spatial heterogeneity in the tensile strength (so that dropping the pressure activated more conduits), or else a condition that moderated the rate of gas release from a given outlet as a function of the stress state (rather than just "open" or "closed"). In real sediments, it is likely that both mechanisms play a role, as well as that the tensile strength varies in time.

4.4.3 Temporal clustering

In all experiments the hazard function $h(\tau)$ exhibits power-law decay indicative of temporal clustering. The long-term regime has a slope of ≈ -0.4, corresponding to a Weibull process with $\beta = 0.6$. The temporal clustering is consistent with a process controlled by sediment conduits that heal in time following bubble passage. If the sediment tensile strength within a conduit is temporarily destroyed as a gas bubble forces apart the fine-grained (0.1–10 μm) mud particles, it may be re-established over time after the conduit closes.

One difference between our observations of short-τ temporal clustering and previous work showing recovery of yield stress [*Merckelbach et al.*, 2002] is the timescale over which these processes operate. That work showed recovery of up to 200 Pa in yield stress over order of 100 days, with a roughly linear increase over time. If tensile strength recovery is the cause of the short-term temporal clustering in our system, then its magnitude would have to be significant, even over the scale of seconds and minutes, to show an appreciable decline in $h(\tau)$ over those time scales. The power-law scaling of $h(\tau)$ suggests that σ_T could recover as $\tau^{1-\beta}$ so that the initial rate of recovery could be larger than the late-term recovery scale, but if the work above is used to estimate the magnitude of the late-term recovery (200 Pa in 100 days), then for $\beta \approx 0.4$, the amount of recovery at 1 hour would only be 4 Pa. Such stress is small relative even to the buoyancy of a 1-cm bubble, $\sim$ 100 Pa. Therefore, tensile strength recovery alone does not appear to be a sufficient explanation for the temporal clustering. Other mechanisms that could mediate bubble release over short time scales include viscous behavior of the sediment-water matrix [*Boudreau et al.*, 2005; *Algar et al.*, 2011a,b] and disturbance of nearby surrounding sediments with bubble

motion, triggering or facilitating aftershock mobilization.

4.4.4 Spatial clustering

The spatial signature of ebullition from sediments at the sub-meter scale is characterized by outlets that are most active over bursts of 1–2 minutes but are capable of persisting for days and even months. The spacing between these hot spots varied between experiments, becoming more dense and with smaller clusters in the later experiments.

At the shortest timescale, bubbles tended to escape in bursts of activity that were strongest within 3 cm and 2 minutes, as seen in the spatio-temporal RDF (Fig. 4-22). The strong temporal component of spatial clustering is consistent with the observation of temporal clustering in the decaying hazard function, even for pixels of size 3 cm (Section 4.3.2).

This spatial clustering persisted over at least several hours, and it continued to shape the spatial signature of short-range spatial clustering and long-range spacing in the RDF over days (Fig. 4-21). Progressively longer samples show decay of the clustering signal over at least 2 days, suggesting that over time new outlets at independent locations become active and make the spatial pattern resemble that of a CSR process. Despite this, for each experiment a number of major active outlets could be detected in the long-term composite flux map (Fig. 4-15), and these outlets showed mild but significant spatial clustering when combined across experiments (Fig. 4-24).

The spatial character of the ebullition, both the persistence of outlets and their spacing, appeared to progress over the 10-month course of running experiments. The first 2 experiments showed greater persistence in the spatial clustering, with $\leq 50\%$ decay in $g(r = 1 \text{ cm})$ between 15-minute and 2-day samples, compared with $\geq 50\%$ decay in the later 3 Experiments. The persistence of spatial clustering in Experiments 1 and 2 was manifest as fewer major active outlets compared with the later experiments (19 and 28 vs. ≥ 43), corresponding with more distant average spacing (8.5 and 7.0 cm, vs. 5.1–5.6 cm). The difference in spatial character could be explained by different forcing conditions (Table 4.1). However, Experiment 4 was

also forced with a large water level drop and showed a significant ebullition peak (Fig. 4-10), yet still its spatial character resembles that of Experiments 3 and 5 qualitatively (Fig. 4-15) and quantitatively (Fig. 4-21). So, the spatial character appears independent of the mode of gas release.

The progression towards more densely-spaced major outlets over the 10 months that were spanned by the 5 experiments may be indicative of development of a more ramified outlet network that allows gas to escape from a greater number of (more densely-spaced) locations. This is a surprising finding given that the initial condition was one of homogeneity; the expectation was that the system would progress towards a greater degree of spatial organization that favored re-use of fewer, more distantly-spaced outlets. Other laboratory experiments have indicated that bubble escape networks progress towards a more stable state [*Ramos et al.*, 2015], although those experiments were carried out with a needle injection source at constant flowrates, and with larger grains (diameter > 200 μm, vs. clay platelets of order $0.1 - 10$ μm) that became "fluidized" with gas passage.

4.4.5 Summary

In summary, a laboratory incubation of lake sediments has demonstrated both hydrostatic triggering of ebullition and re-use of outlets over the scale of days and even months. The re-use of outlets and their spacing may be interpreted as resulting from a significant reduction of sediment tensile strength with gas passage, and their persistence is rationalized as slow recovery of the outlets relative to the timescales of hydrostatic forcing and gas generation. The short-term temporal clustering of bubble releases may arise from a combination of tensile strength reduction and recovery, localized disturbance of aftershocks, and viscous sediment deformation. Together, these observations point to a refined mechanistic, conceptual model for gas bubble growth and mobility in soft sediments.

Chapter 5

Summary and future work

5.1 Combined discussion

The *main findings* from this work are:

1. *Hydrostatic pressure* plays a clear role in enhancing and inhibiting ebullition.

2. Ebullition events and bubble arrivals are *clustered in time* relative to a Poisson process over a range of spatial scales (3 cm–8 m), consistent with a combination of reduction and healing of sediment tensile strength following bubble passage, viscous deformation and localized sediment disturbance triggering aftershock mobilization.

3. Ebullition events and bubble arrivals are *clustered in space* both at the scale of individual outlets ($\sim 1-5$ cm) and seep clusters ($\sim 1-3$ m). Individual outlets show persistence over the scale of days and even months, while activity within a seep cluster appears ephemeral, limited to ~ 1 day, depending on the flux mode.

Each is discussed below, comparing results from the field-scale sonar observations and laboratory-scale incubation experiment.

5.1.1 Hydrostatic triggering

The ability of hydrostatic pressure to enable and inhibit ebullition was observed in both the field-scale sonar results (Fig. 3-2) and the laboratory-scale experimental results (Fig. 4-7–4-11), demonstrating this effect for the first time under controlled laboratory conditions. During cycles of pressure variation at roughly daily frequency and with magnitude < 0.3 m H_2O of water column, the ebullitive flux varied continuously in a roughly anti-correlated manner with hydrostatic pressure (Figs. 4-9 and 4-11). Raising the pressure by > 0.3 m of water and maintaining that level was able to inhibit significant ebullition for at least 5 days (Fig. 4-7), but it is likely that after a prolonged period at that level the gas bubbles would reach sufficient pressure and size to overcome the tensile strength of the sediment and force their way out. Conversely, lowering the pressure and keeping it low caused a large spike in the ebullition rate (Figs. 3-2, 4-7, 4-8, and 4-10). Over time, depletion of stored gas appears to play a role, as the ebullition spikes subsided within 1–2 days even when the pressure was kept low, and following massive ebullition events the system demonstrates quiescence even when subjected to further hydrostatic pressure variations (Figs. 3-2 and 4-7).

5.1.2 Temporal clustering

Ebullition events and bubble arrivals are clustered in time relative to a Poisson process over a range of spatial scales (3 cm–8 m), consistent with a process of reduction and healing of sediment tensile strength following bubble passage. The distribution of inter-arrival times, as quantified using the hazard function, shows power-law decay for pixels of size 3 and 37 cm in the experiment and size 0.5 and 8 m in the sonar data. This power-law decay can be modeled as a Weibull process, used in failure analysis to model a collection of components that show premature failure and increasing reliability with time. We propose that the gradual increase in reliability is consistent with healing of sediment tensile strength following bubble passage, making it progressively less likely that a bubble will have sufficient pressure to reduce the effective stress and

force the grains apart with time. The fact that $h(\tau)$ shows power-law decay over a range of spatial scales reflects the fact that a collection of Weibull elements still behaves like a Weibull element, though in simulations this spatial upscaling should produce slightly shallower decay because the elements act independently. The main potential inconsistency with our interpretation relates to the fact that we see hazard decay over short inter-arrival times (≤ 1 day), compared with previous observations of relatively slow recovery in sediment strength (10–90 days) [*Merckelbach et al.*, 2002]. Therefore, the recovery of reliability over short timescales may involve other processes, including the slow rise of bubbles through viscous sediments [*Boudreau et al.*, 2005; *Algar et al.*, 2011a,b], as well as aftershock triggering of gas release.

Comparing the temporal clustering observed in the experimental results (Section 4.3.2, Fig. 4-12) and field-scale observations of ebullition events (Section 3.3.1, Fig. 3-4) leads to interesting questions. The sonar data revealed stronger temporal clustering, both in the short-term (slope < -1 for $\tau < 5$ min) and the long term (slope $= -0.6$, vs -0.4 ± 0.1 in the experiment). The weaker clustering in the tank experiment, whose entire area is smaller than the 0.5-m pixels used in the sonar analysis, is surprising given that it resolves arrival of individual bubbles, which could show potentially strong temporal dependence that would not be masked by the fusion of bubbles into ebullition events for the sonar record (Section 2.2.5). The fact that the sonar showed stronger temporal clustering suggests that this fusion does not mask temporal clustering above the scale of $\tau = 15$ s over which the sonar data were analyzed. However, the strength of clustering (slope of $h(\tau)$) has some uncertainty in both analyses, and the 95% confidence intervals likely overlap at a slope of ≈ -0.5. Even if that is the case, a mystery remains in that the 0.5-m pixels in the sonar record showed stronger temporal clustering, with slope < -1 for $\tau < 5$ min (Fig. 3-4), and weaker clustering for $\tau > 5$ min, compared with the opposite situation for the 0.37-m pixels in the experiment (Fig. 4-12).

5.1.3 Spatial clustering

Ebullition events and bubble arrivals are clustered in space both at the scale of individual outlets ($\sim 1-5$ cm) and seep clusters ($\sim 1-3$ m), and these spatial features persist to different extents. The experimental results show clustering of activity with a radius of 2–5 cm and spacing of 5–9 cm (Section 4.3.3, Fig. 4-21), and these clusters (which we associate with individual outlets given the resolution of the method) may persist for days (Fig. 4-21) and, to a lesser extent, over months (Fig. 4-24). This persistence was surprising because spatial clusters at the field scale (radius 1–3 m) only dominated the spatial distribution of gas flux over hours or days, depending on the flux regime (Section 3.3.2, Fig. 3-7). How can small-scale heterogeneity persist, even given a roughly homogeneous initial condition, when large-scale heterogeneity is ephemeral?

We can rationalize the persistence of fine-scale heterogeneity as arising from a different process at a different scale (individual conduits or clusters of conduits vs. entire 0.5-m sediment tiles populated with hundreds or thousands of outlets), or as evidence of incomplete progress towards a steady state in the incubation tank. The persistence and spacing of outlets appeared to decay over the 10-month course of experiments, suggesting that a fully-mature sediment conduit network would display even less persistent, preferential re-use of distant outlets (barring deposition of concentrated sources of methanogenesis). In the limit where conduit spacing is limited by diffusive mass flux from surrounding sediments towards ecah conduit, the length scale is expected to be on the order of $\approx 5-7$ cm for diffusion over ~ 1 month between major ebullition events, and this distance is similar to the spacing of the major outlets in later experiments. As an alternative explanation for the significant role of conduit re-use, the strong methanogenesis source in the experiment (both from high temperature and a > 20 cm column of fresh organic matter) could support conduit re-use simply by more frequent bubble release due to a larger population of bubbles accessed by a single outlet.

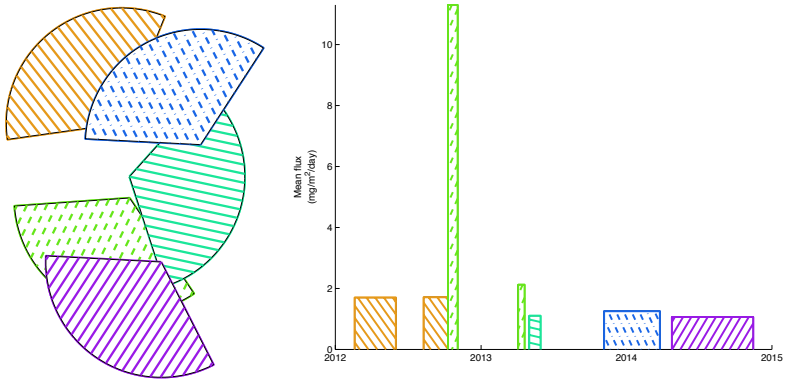

Figure 5-1: Left: schematic showing all deployment locations relative to each other. The side of each fan is length 20 m. Right: time series showing the continuous deployment periods at each deployment location, with the height of each bar showing the spatiotemporal average gas flux at that location.

5.2 Future work

The work described above yields evidence of spatial and temporal clustering that may be associated with methane transport within the sediments, but further work is required to definitively identify the mechanisms at play. Here we describe potential avenues for future research, both in terms of expanding the scope of the field research and in terms of deepening the analysis and mechanistic modeling of the results from the incubation experiment.

5.2.1 Field scale

Unpublished data from 2013-2015

In addition to the results presented in Chapter 3, data were also collected using the sonar lander during 4 subsequent periods not analyzed above. Their relative locations and deployment periods are shown in Fig. 5-1. Preliminary analysis suggests that the directional sensitivity of the sonar may have changed over the course of the following year, necessitating a similar beam pattern correction to that applied to the data presented above (see Section 2.2.6). One of the deployment periods shows a composite flux map with enhanced activity in a region $\sim$ 10 m in diameter and centered $\sim$ 15 m from the sonar head, which would not arise as an artifact

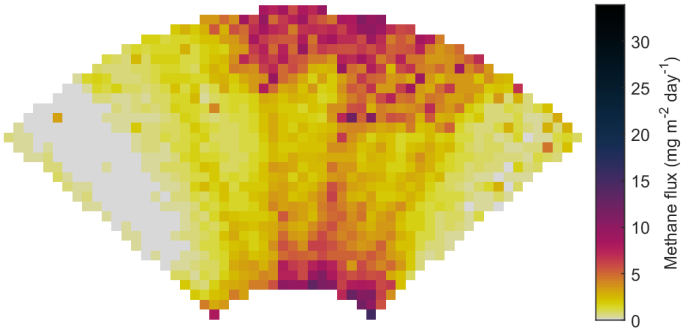

Figure 5-2: Composite spatially gridded data from May 1–31, 2013, showing spatially-correlated signals that vary over the scale of $\sim 5 - 10$ m and appear to depend on both direction and distance.

of spurious directional sensitivity correction (Fig. 5-2). Thus, there may be some degree of qualitative variability in the large-scale heterogeneity of ebullition between deployment sites, though this preliminary finding requires further investigation.

Given the proximity of the deployment locations, and if the character of ebullition is found to be similar between them, the data from these subsequent deployments could potentially be used to detect *seasonal and inter-annual variability in ebullition*. Also, a daily cycle in the raw sonar signal (typically too low-intensity to be detected as bubbles) during May 2012 and 2013 is synchronous with daily solar radiation and is thus consistent with *diurnal migration of midge larvae* (Chaoborus or Chironomus) to the anoxic hypolimnion to avoid fish predation. The increasing amplitude of the diurnal cycle in the sonar record over the month of May is also consistent with the migration of Alewife herring into UML during late April and early May [*Herron*, 2016].

Other deployments

The deployment of the sonar tripod to the deepwater basin of UML leaves open the question of what different results would be obtained in other regions of the lake, as well as in other lakes and water bodies? Within UML, a primary constraint is the availability of shore power and shelter for the control and recording equipment. If the Tufts sailing team continues to support this research, the lander could be deployed

closer to the boathouse in the southeast corner of the lake, or it could be deployed further with an additional length of cable. Given the required 12 A power-on inrush current for the sonar, more detailed calculations are prudent before attempting to extend the 16-gage wires beyond their current range of 360 m (Section 2.3.1).

In other deployment locations where indoor storage is available, the shore equipment fits within a $0.6 \times 0.4 \times 0.4$ m plastic container with holes for ventilation, and the primary challenge is finding an appropriately secure place to thread the cable through the building walls. In principle, the shore equipment could be deployed in an outdoor weather-proof container, though it would require secure locking and anti-theft mechanisms and have appropriate ventilation to avoid overheating, which caused computer problems early in the deployment.

For more remote deployments, the lander would require re-design to accommodate on-board power, computer control and data storage, while eliminating the need for the ethernet extender. Deployment and recovery would also be more complex. The Imagenex 837B DeltaT unit used in this study was rated to 300 m depth, but the manufacturers offer the same unit with housings rated to 1000, 2000 and 6000 m depths. Therefore, the horizontal multibeam method presented in Chapter 2 could even be used to estimate fluxes from seeps in marine environments, given the appropriate deployment system.

For example, the Ocean Networks Canada NEPTUNE observatory detects but does not quantify ebullition using a vertically-oriented Imagenex 837B on a mechanically-rotating chassis to observe the vertical and lateral components of bubble streams in the Pacific Ocean [*Roemer et al.*, 2015; *Spence*, 2016]. That system is powered and controlled via a cable that supports a broad range of scientific instruments, including seismometers, current profilers, cameras, fluorometers and other chemical sensors. In another study, a Kongsberg M3 multibeam sonar was deployed in the horizontal orientation on an ROV to characterize the dimensions of gas flares as a function of their height, and such data could be interpreted for flux estimates using the visually-characterized bubble size distributions [*Wang et al.*, 2016].

Extended range

The Imagenex 837B sonar used on the NEPTUNE observatory is set to the maximum range of 100 m, instead of the 20 m range used in this study. While it is unclear whether bubble quantification, and especially discrimination of bubbles from non-bubble targets in low-flow rate settings like lakes, is reliable at the 100 m range setting, making this change would significantly increase the observation area, from ≈ 400 m^2 by a factor of 25, to $\approx 10^4$ m^2. In addition to potentially lower detectable flow rates, this adaptation would also decrease the pulse repetition rate by $\approx 50\%$, which for the system used here would ping only ≈ 3 per second. The reduced frequency of pings would make individual bubbles harder to detect close to the sonar head (Section 2.2.4), though a bubble ≥ 2 m away should be insonified by at least one ping. The spatial resolution would also decrease, with pixels 20 cm long and as wide as 1.75 m at 100 m range.

5.2.2 Laboratory scale

The analysis of the incubation experiment presented above hints at the mechanisms driving the episodicity of ebullition and the re-use of conduits, but many questions still remain:

- Is sediment tensile strength reduction the mechanism driving conduit and nucleation site re-use?
- Does disturbance of sediments with bubble passage travel far enough with large enough magnitude to trigger "aftershock" activity in surrounding conduits?
- What causes the hazard function decay over short time periods? Does healing of tensile strength occur over a short enough timescale to play a role?
- What is the spacing and size distribution of bubbles trapped within sediments?
- What is the morphology of gas conduits?
- Do outlets collect bubbles laterally from surrounding sediments?

- Was the more distant spacing observed in Experiments 1 and 2 a transient effect of incomplete development of the conduit network, or a persistent characteristic of the system controlled by other factors not at play in the other experiments?
- Does the distribution of bubble sizes (and therefore bubble survival) change depending on the mode of gas release?
- What is the role of compositional heterogeneity of the sediments?

Some further insight may be gained with further analysis of the existing data, such as calculating the hazard function over the major outlets, as opposed to gridded data in the above analysis (Section 4.3.3). Bubbles arrive in spatiotemporal clusters (Fig. 4-22), but these clusters themselves may also arrive with spatial and temporal organization that is not completely spatially random.

A way to test the hypothesized conceptual model that motivated our research is by simulating it numerically and comparing its behavior against the statistical analysis of the data presented above. Such a model would be a fairly natural extension of 1D models of gas transport and release from lake sediments [*Scandella et al.*, 2011] and hydrate-bearing ocean sediments [*Scandella and Juanes*, 2011]. Some of the elements of the mechanistic model could include:

1. Evolution of areally-variable (but depth integrated) gas volume saturation.
    - Generate gas volume at a constant rate.
    - Allow some of the trapped gas to escape with each bubble mobilization or ebullition event.
2. Constraint of the effective stress between 0 and $-\sigma_T$, causing plastic gas cavity compression and dilation at these limits, respectively [*Scandella et al.*, 2011].
3. Tensile strength σ_T reduction with bubble passage and recovery with time between events.
4. Bubble mobilization conditions:

- Minimum volume threshold to capture the role of buoyancy in mobilizing bubbles [*Algar et al.*, 2011a]. To reproduce periods if intense activity followed by periods of inhibition due to depletion, this threshold could drop and recover proportionally to the tensile strength.
- Probabilistic tensile failure, simulated with probability proportional to $(-\sigma'/\sigma_T)$. This formulation reproduces the Weibull decay in hazard (rate of failure) with increasing inter-arrival time τ if $\sigma_T \sim \tau^{1-\beta}$, assuming that σ' changes slowly relative to the timescale for recovery of σ_T.

5. Collection of gas from surrounding sediments. Allow the outlet in a given pixel to reach the volume threshold for release depending on the total volume of stored gas within some radius of influence.

6. Triggering of aftershocks by reduction of σ_T in some the vicinity bubble mobilization.

7. Gas pressurization with gas generation, to allow gas mobility in the absence of an external forcing.

However, some of these questions can only be answered with other methods. A comparative incubation of minimally-disturbed sediments would elucidate the role of clumps of more-labile organic matter and more-cohesive sediments in the creation of persistent heterogeneity in ebullition. Further characterization of the sediment heterogeneity, conduit morphology and distribution of trapped bubbles could be observed using in-situ x-ray imaging and freeze coring [*Spliethoff and Hemond*, 1996]. The chemistry and biology of methanogenesis could be assessed using isotopic analysis of the pore water and evaded gas, as well as genomic analysis of the sediment microflora.

5.3 Broader impacts

The problem of estimating methane emissions from submerged sediments remains a challenge because of difficulties with measurement and a meager mechanistic basis

for modeling the process with sufficient spatiotemporal resolution to predict bubble survival during rise through the water column. The work presented here has expanded the state of the art on both fronts, with development of methods for quantifying spatiotemporally-resolved ebullitive fluxes over long periods at the laboratory and field scales, as well as interpretation that lends to further mechanistic modeling of individual conduits and large collections of them. Taken together, and in conjunction with efforts to constrain bubble size distributions and model gas dissolution during rise [*McGinnis et al.*, 2006; *Ostrovsky et al.*, 2008; *DelSontro et al.*, 2015; *Delwiche et al.*, 2015], these developments are a part of the larger effort to estimate the methane source to the atmosphere at the global scale and to predict how its magnitude will shift with changes induced by climate change, such as shifts in precipitation patterns that influence the timing and magnitude of hydrostatic pressure triggering of ebullition.

Appendix A

Estimation of statistics for detecting spatiotemporal clustering and spacing

A.1 Hazard function

Further insight into processes controlling ebullition is furnished by the distribution of inter-arrival times between bubble release events—'events' are bubble-release sequences that persist with breaks no longer than 2 s (given 5-s moving-average filtering). Distributions of inter-arrival times may be analyzed using the hazard function,

$$h(\tau) = \frac{f(\tau)}{1 - F(\tau)}, \tag{A.1}$$

where $f(\tau)$ is the probability density function (PDF) of inter-arrival times τ, and $F(\tau)$ is the cumulative density function (CDF) [*Stapelberg*, 2009]. $h(\tau)$ quantifies the probability of an event occurring conditioned on a given amount of time having passed since the last event. For a Poisson process, events are independent and have uniform probability, corresponding to constant h since the events have no memory of previous arrivals. For a Weibull process—a model often used in reliability engineering to model component failures—the hazard function is a power law, $h(\tau) = (\beta/\lambda)(\tau/\lambda)^{\beta-1}$, where β and λ are the shape and scale parameters, respectively. A decreasing power law ($\beta < 1$) corresponds to strong temporal clustering, while an increasing power law

($\beta > 1$) is associated with more regularly periodic arrivals [*Stapelberg*, 2009].

A volume-weighted hazard function (HF) $h_V(\tau)$ was estimated numerically by weighting each event's contribution by the volume of gas released during a given ebullition event (in the case of the sonar data) or the volume of each bubble (for the incubation experiment. The function is estimated as:

$$h_V(\tau) = \frac{\sum_{i \in \text{arrived}} V_i}{d\tau \sum_{i \in \text{exposed}} V_i}, \tag{A.2}$$

where V_i is the gas volume of the i^{th} event, and the sets "arrived" and "exposed" represent the events that have arrived following wait times in the interval $[\tau, \tau + d\tau]$, and those that have not yet arrived after time τ, respectively. Logarithmically-spaced bins in τ were used to reduce the variance of the estimator at long inter-arrival times, and the estimator was validated with simulations of Poisson and Weibull processes. For the sonar analysis, a minimum inter-arrival time of 15 s was used because this represents the characteristic duration of bubbling events. For the experimental analysis, a minimum inter-arrival time of 1 s reflected the resolution of the imaging method.

A.1.1 Handling breaks in continuous observation periods

In both the sonar field observations and laboratory incubation experiment, the observation methods went through occasional periods of inoperation. These were caused by a combination of intentional pauses, such as for switching hard drives, and unintentional breaks, like when a hard drive was accidentally filled, or when the building power went out. The periods of active recording were tracked and used when handling the data, for example to extrapolate flux estimates in time when the system was recording during at least 50% of the sample interval. Knowing breaks in recording periods is especially important when estimating the HF because an observation system may fail to detect events while it is offline. If the HF is estimated without accounting for breaks in observation periods, the relative importance of long inter-arrival times will be overestimated. The problem may be remedied by removing IATs that span periods of inactive recording. Periods of observation that were separated by less than

1 second were treated as continuous.

A.2 Radial distribution function

A.2.1 Overall estimation methods

To account for the enhanced importance of events releasing large volumes of gas, the volume-weighted RDF $g(r)$ was estimated using the marked pair correlation function [*Illian et al.*, 2008]. Estimating the RDF requires an observation window within which the data are first-order stationary in density and magnitude [*Illian et al.*, 2008]. This stationary window was found to span the central 60° of the sonar fan and from 6-20 m from the sonar head (Fig. 3b), after correcting for the directional sensitivity of the sonar.

To account for the enhanced importance of events releasing large volumes of gas, the volume-weighted RDF was estimated using the marked pair correlation function [*Illian et al.*, 2008, Eqn. (5.3.54)] and the mark-sum intensity [*Illian et al.*, 2008, Eqns. (4.2.20) and (5.2.2)], with the volume of gas released during an event serving as its mark. The isotropized set covariance was estimated numerically for the irregular observation window and used in place of the pair-specific displacement area [*Ohser and Mücklich*, 2000, Eqn. (9.29)]. The method was confirmed as unbiased using simulations of a CSR process on the same domain used by the sonar.

To account for the enhanced importance of events releasing large volumes of gas, the volume-weighted RDF was estimated using the marked pair correlation function [*Illian et al.*, 2008, Eqn. (5.3.54)] and the mark-sum intensity [*Illian et al.*, 2008, Eqns. (4.2.20) and (5.2.2)], with the volume of gas released during an event serving as its mark. A box-window was used, and the isotripic version of the estimator was used that weighted events by the radially-dependent isotropized set covariance instead of the intersection of the distance-shifted observation window [*Illian et al.*, 2008, Eqn. (4.3.31)]. This approximation greatly decreases the computational load of the estimation without sacrificing significant accuracy, when such large numbers of

bubbles (≈ 1000) were available. In addition to the spatial RDF, the spatiotemporal RDF (ST-RDF) was estimated to understand the relationship between spatial and temporal scales of clustering and spacing [*Illian et al.*, 2008, Eqn. (6.10.15)]

A.2.2 Spatial RDF

Data from Feb 18–May 31, 2012 were divided into segments of 20 min in duration, which were classified as high- or low-flux relative to the average over the whole deployment period. From these segments, continuous samples of durations from 10 min to 4 days were analyzed to test the impact of observation time on the spatial signature observed.

The sonar technique provides sufficient resolution to confirm that the outlets are distinct, as the maximum pixel separation of 0.35 m is finer than the event separation of ≥ 0.5 m, and bubbles are unlikely to drift laterally by more than 0.1 m during their rise of ~ 1.5 m from the sediment surface to the sonar fan, given typical lateral currents on the scale of 1 cm/s (observed from slow, spatially-coherent drift of low-intensity signals reflecting suspended flocs) and bubble rise velocities of $20 - 25$ cm/s [*Ostrovsky et al.*, 2008]. It is possible that non-bubble targets, such as anchor lines, contaminate the RDF sufficiently to create an appearance of spatial clustering in the mean, but these constitute $\leq 6\%$ of the flux so should not create the pronounced effect seen here (Figs. 3-7).

A.2.3 Spatio-temporal RDF

Therefore, the STRDF can elucidate the temporal and spatial scales associated with active cluster formation, while the spatial RDF (SRDF) sampled at different time interval lengths can tell about the persistence of those clusters. If clusters appear over the scale of 10 minutes and then go dormant, they will only show spatial clustering up to 10 min in the STRDF. However, if the appearance of new clusters happens slowly enough, then only a small handful of clusters may exist within an hour-long or even day-long sample of the data, and a clustered signature may appear in the SRDF

over hour or day-long samples. Only when sufficiently dense activity has appeared that can create the appearance of a spatially-random process will the SRDF show a homogeneous process, so the SRDF is effective at detecting timescales of declustering, the dominance of independent arrivals. The STRDF detects the timescale of activity of those clusters, which may be significantly shorter than the timescale for declustering of the spatial pattern (Fig. 4-22).

Appendix B

Design drawings for sonar lander

The sonar tripod was constructed with few components listed in Table B.1 and labeled in Fig. B-1. Stainless steel bolts were used to inhibit galvanic corrosion, and while their presence caused the aluminum parts of the tripod (especially the base speed rail fittings) to corrode over approximately 1 year of deployment in the anoxic hypolminion of Upper Mystic Lake, MA, the structural integrity of the tripod was maintained. Brackets for attaching the sonar head and ethernet communications bottle to the central PVC pipe were fabricated out of aluminum and PVC, respectively (not shown). The gimbal for self-leveling was designed and constructed by E. Bergeron at the U.S. Geological Survey at Woods Hole (Figs. B-3 and B-4).

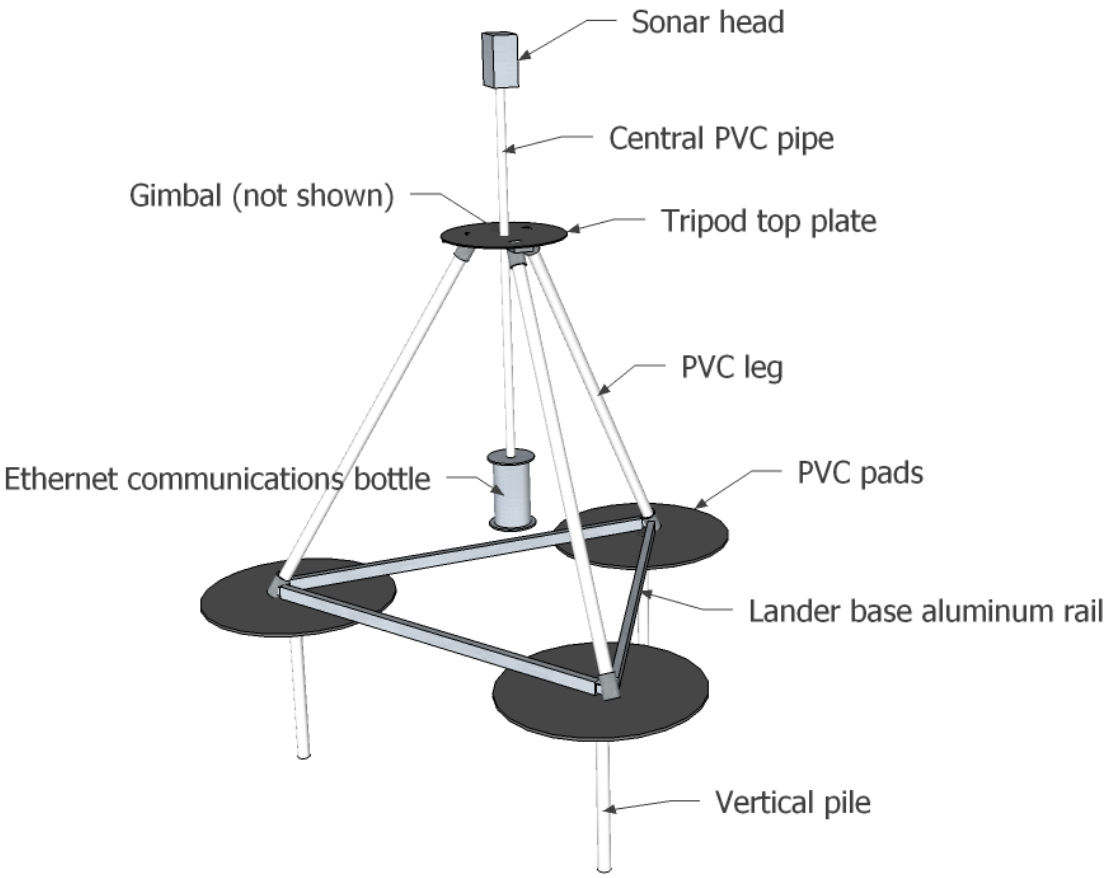

Figure B-1: Schematic of the sonar tripod, labeling parts referenced in Table B.1.

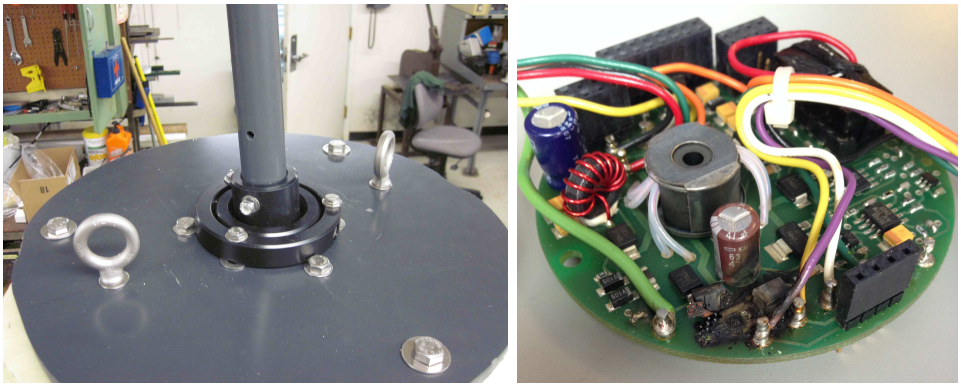

Figure B-2: Left: Photograph of the top plate of the tripod, showing attachment bolts for the legs, eye bolts for the lifting harness, the gimbal and central PVC pipe. Right: Photograph of the power circuit board damaged by a high-voltage surge on May 29, 2013.

Table B.1: List of major lander components and their dimensions. PVC legs and vertical were 1.5 in nominal, schedule 40 PVC. Central PVC pipe is 1 in sch. 40. The base speed rail fittings were welded to the base rails with a 60° angle of elevation. See labeled diagram in Fig. B-1. Other important compontents of the system not listed here include the surface ethernet extender, control computer, surge protector, hard drive, and (optionally) internet connection equipment.

Item	Number	Length (cm)	Diameter (cm)
Sonar transducer	1	16.5	10.7 by 7.9
Ethernet communications bottle	1	27.0	15.9
Sonar-bottle connection cable	1	100	
Strain relief mesh loop	1		
Top plate	1	0.5 in	15 in
Speed rail 48SBC flanges	3		
Gimbal	1	Fig. B-2	
Aluminum base rails	3	152	
Base speed rail fittings	3		1.5 in NPS
Pull pins	3		
PVC legs	3	161	4.826 (1.5 in NPS)
Vertical PVC piles	3	61	4.826 (1.5 in NPS)
PVC pads	3	0.64 ($\frac{1}{4}$ in)	41
Central PVC pipe	1	137	3.340 (1 in NPS)
Bottle attachment bracket	1		
Sonar attachment bracket	1		
Cable to shore	1	275 m	
Medium cable	1	60 m	
Indoor cable	1	25 m	
Foam plates	3		15 in
Bridle PVC	1	100	(1.5 in NPS)

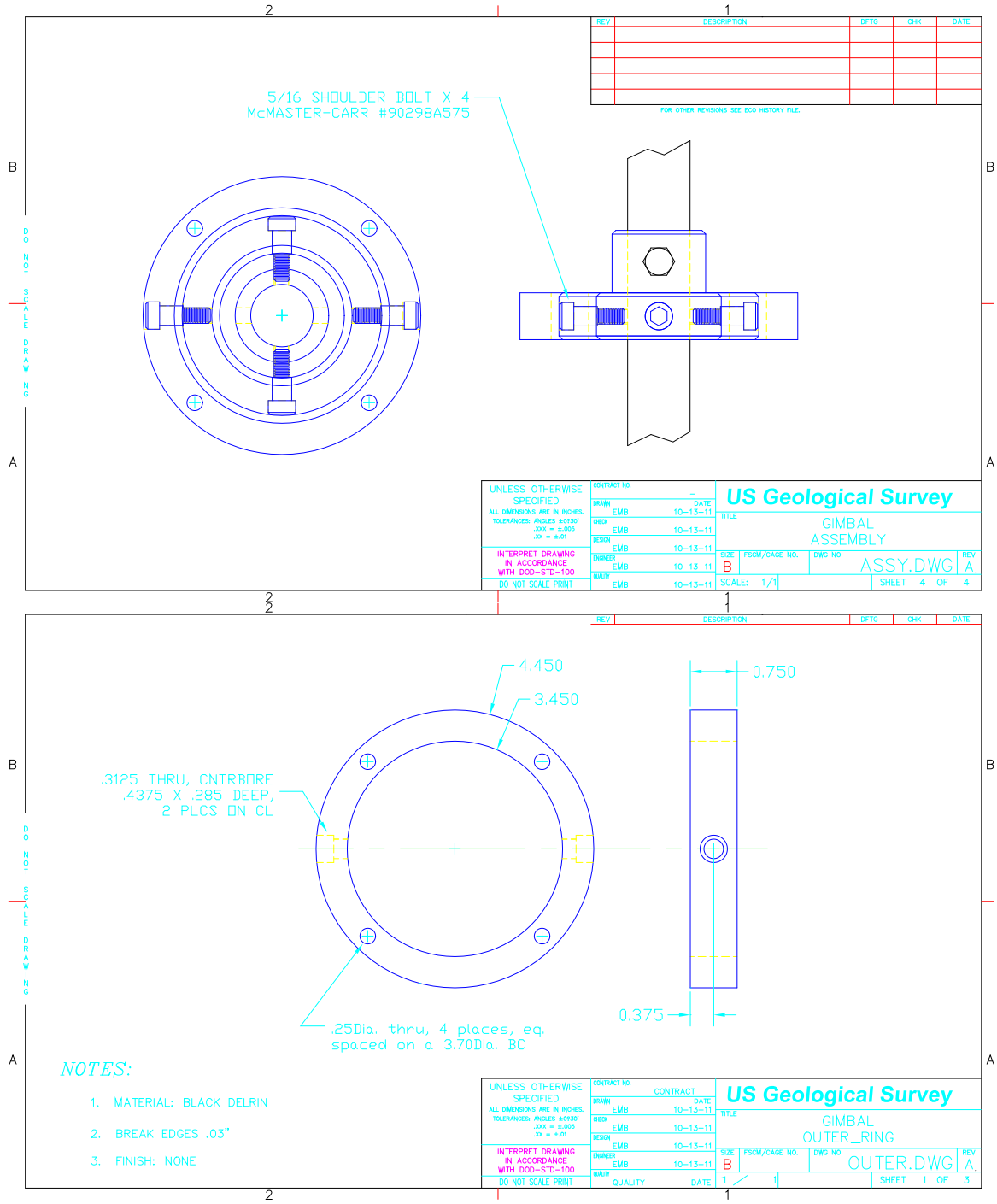

Figure B-3: Design drawings for the gimbal: assembly and outer pieces. Design and construction by E. Bergeron, USGS Woods Hole.

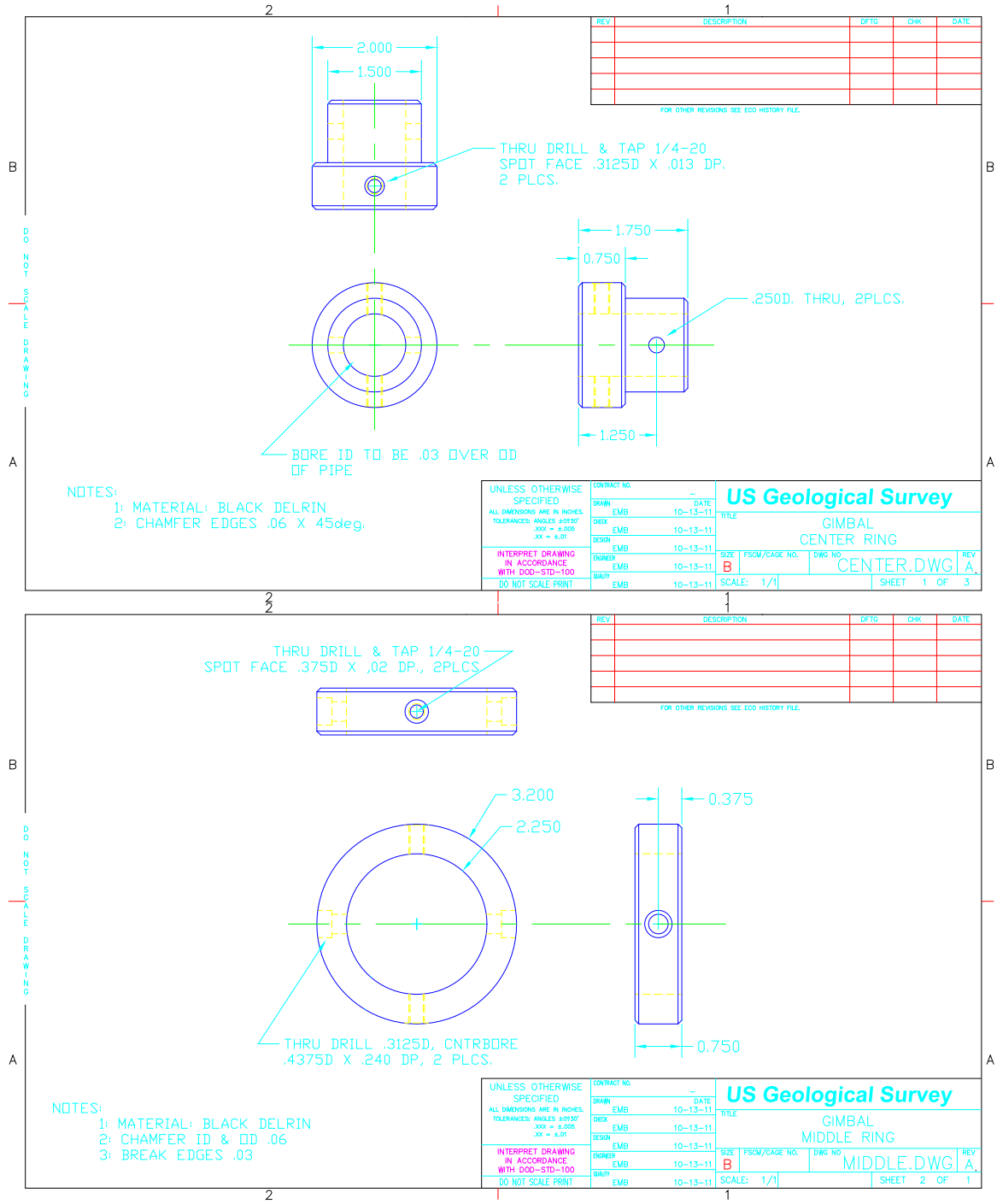

Figure B-4: Design drawings for the gimbal: center and middle pieces. Design and construction by E. Bergeron, USGS Woods Hole.

Bibliography

Algar, C. K., and B. P. Boudreau (2009), Transient growth of an isolated bubble in muddy, fine-grained sediments, *Geochimica et Cosmochimica Acta*, *73(9)*(9), 2581-2591.

Algar, C. K., B. P. Boudreau, and M. A. Barry (2011a), Initial rise of bubbles in cohesive sediments by a process of viscoelastic fracture, *Journal of Geophysical Research*, *116*, B04207.

Algar, C. K., B. P. Boudreau, and M. A. Barry (2011b), Release of multiple bubbles from cohesive sediments, *Geophysical Research Letters*, *38*, L08606.

Allen, M. R., D. J. Frame, C. Huntingford, C. D. Jones, J. A. Lowe, M. Meinshausen, and N. Meinshausen (2009), Warming caused by cumulative carbon emissions towards the trillionth tonne, *Nature*, *458*(7242), 1163-1166.

Anderson, V. C. (1950), Sound Scattering from a Fluid Sphere, *Journal of the Acoustical Society of America*, *22*(4), 426-431.

Archer, D. (2007), Methane hydrate stability and anthropogenic climate change, *Biogeosciences*, *4*(4), 521-544.

Archer, D., B. Buffett, and V. Brovkin (2008), Ocean methane hydrates as a slow tipping point in the global carbon cycle, *Proceedings of the National Academy of Science*, *106*, 20596-20601.

Bastviken, D., J. Cole, M. Pace, and L. Tranvik (2004), Methane emissions from lakes: Dependence of lake characteristics, two regional assessments, and a global estimate, *Global Biogeochemical Cycles*, *18*(4), GB4009.

Bastviken, D., L. J. Tranvik, J. A. Downing, P. M. Crill, and A. Enrich-Prast (2011), Freshwater methane emissions offset the continental carbon sink, *Science*, *331*, 50.

Bayrakci, G., et al. (2014), Acoustic monitoring of gas emissions from the seafloor. Part II: a case study from the Sea of Marmara, *Marine Geophysical Research*.

Berndt, C., et al. (2014), Temporal constraints on hydrate-controlled methane seepage off Svalbard, *Science*, *343*(6168), 284-287.

Boles, J., J. Clark, I. Leifer, and L. Washburn (2001), Temporal variation in natural methane seep rate due to tides, Coal Oil Point area, California, *Journal of Geophysical Research*, *106*(C11), 27077-27086.

Boudreau, B., et al. (2005), Bubble growth and rise in soft sediments, *Geology*, *33*(6), 517-520.

Bussmann, I., S. Schlomer, M. Schluter, and M. Wessels (2011), Active pockmarks in a large lake (Lake Constance, Germany): Effects on methane distribution and turnover in the sediment, *Limnology and Oceanography*, *56*(1), 379-393.

Chanton, J., C. Martens, and C. Kelley (1989), Gas transport from methane-saturated, tidal freshwater and wetland sediments, *Limnology and Oceanography*, *34*(5), 807-819.

Chen, Y.-H., and R. G. Prinn (2005), Atmospheric modeling of high- and low-frequency methane observations: Importance of interannually varying transport, *Journal of Geophysical Research*, *110*, D10303.

Chen, Y.-H., and R. G. Prinn (2006), Estimation of atmospheric methane emissions between 1996 and 2001 using a three-dimensional global chemical transport model, *Journal of Geophysical Research*, *111*, D10307.

Ciais, P., et al. (2013), *Carbon and Other Biogeochemical Cycles*, chap. 6, pp. 465–570, Cambridge University Press, Cambridge, United Kingdom and New York, NY, USA.

Clark, J. F., L. Washburn, and K. S. Emery (2010), Variability of gas composition and flux intensity in natural marine hydrocarbon seeps, *Geo-Marine Letters*, *30*(3-4), 379-388.

Comas, X., and W. Wright (2012), Heterogeneity of biogenic gas ebullition in sub-tropical peat soils is revealed using time-lapse cameras, *Water Resources Research*, *48*.

Crill, P., K. Bartlett, J. Wilson, D. Sebacher, R. Harriss, J. Melack, S. Macintyre, L. Lesack, and L. Smithmorrill (1988), Tropospheric methane from an Amazonian floodplane lake, *Journal of Geophysical Research*, *93*(D2), 1564-1570.

Daszykowski, M., B. Walczak, and D. Massart (2001), Looking for natural patterns in data - Part 1. Density-based approach, *Chemometrics and Intelligent Laboratory Systems*, *56*(2), 83-92.

Delsontro, T., D. F. McGinnis, S. Sobek, I. Ostrovsky, and B. Wehrli (2010), Extreme methane emissions from a Swiss hydropower reservoir: Contribution from bubbling sediments, *Environmental Science and Technology*, *44*(7), 2419-2425.

DelSontro, T., M. J. Kunz, T. Kempter, A. Wueest, B. Wehrli, and D. B. Senn (2011), Spatial heterogeneity of methane ebullition in a large tropical reservoir, *Environmental Science & Technology*, *45*(23), 9866-9873.

DelSontro, T., D. F. McGinnis, B. Wehrli, and I. Ostrovsky (2015), Size does matter: Importance of large bubbles and small-scale hot spots for methane transport, *Environmental Science & Technology*, *49*(3), 1268-1276.

Delwiche, K., S. Senft-Grupp, and H. Hemond (2015), A novel optical sensor designed to measure methane bubble sizes in situ, *Limnology and Oceanography: Methods*, *Online issn: 1541-5856*.

Denman, K. L., et al. (2007), Couplings Between Changes in the Climate System and Biogeochemistry, in *Climate Change 2007: The Physical Science Basis. Contribution of Working Group I to the Fourth Assessment Report of the Intergovernmental Panel on Climate Change*, edited by S. Solomon, D. Qin, M. Manning, Z. Chen, M. Marquis, K. Averyt, M.Tignor, and H. Miller, pp. 499–588, Cambridge University Press, Cambridge, United Kingdom and New York, NY, USA, chapter 7.

Fechner-Levy, E., and H. Hemond (1996), Trapped methane volume and potential effects on methane ebullition in a northern peatland, *Limnology and Oceanography*, *41*(7), 1375–1383.

Flemings, P., X. Liu, and W. Winters (2003), Critical pressure and multiphase flow in Blake Ridge gas hydrates, *Geology*, *31*(12), 1057-1060.

Gardiner, B., B. Boudreau, and B. Johnson (2003), Growth of disk-shaped bubbles in sediments, *Geochimica et Cosmochimica Acta*, *67*(8), 1485-1494.

Gong, X., S. Takagi, and Y. Matsumoto (2009), The effect of bubble-induced liquid flow on mass transfer in bubble plumes, *International Journal of Multiphase Flow*, *35*(2), 155-162.

Greene, S., K. M. Walter Anthony, D. Archer, A. Sepulveda-Jauregui, and K. Martinez-Cruz (2014), Modeling the impediment of methane ebullition bubbles by seasonal lake ice, *Biogeosciences*, *11*(23), 6791-6811.

Greinert, J. (2008), Monitoring temporal variability of bubble release at seeps: The hydroacoustic swath system GasQuant, *Journal of Geophysical Research*, *113*, C07048.

Greinert, J., and B. Nutzel (2004), Hydroacoustic experiments to establish a method for the determination of methane bubble fluxes at cold seeps, *Geo-Marine Letters*, *24*(2), 75-85.

Greinert, J., D. F. McGinnis, L. Naudts, P. Linke, and M. De Batist (2010), Atmospheric methane flux from bubbling seeps: Spatially extrapolated quantification from a Black Sea shelf area, *Journal of Geophysical Research - Oceans*, *115*.

Hamblin, W. K., and E. H. Christiansen (2004), *Earth's Dynamic Systems*, Pearson Education, Inc., New Jersey, Brigham Young University, Provo Utah.

Heede, R., and N. Oreskes (2016), Potential emissions of {CO2} and methane from proved reserves of fossil fuels: An alternative analysis , *Global Environmental Change*, *36*, 12 - 20.

Heeschen, K., A. Trehu, R. Collier, E. Suess, and G. Rehder (2003), Distribution and height of methane bubble plumes on the Cascadia Margin characterized by acoustic imaging, *Geophysical Research Letters*, *30*(12).

Herron, P. (2016), Herring Monitoring Program, Mystic River Watershed Association, published online at http://mysticriver.org/herring-monitoring/ and accessed 27 April 2016.

Hoehler, T., M. Alperin, D. Albert, and C. Martens (1994), Field and laboratory studies of methane oxidation in an anoxic marine sediment - evidence for a methanogen-sulfate reducer consortium, *Global Biogeochemical Cycles*, *8*(4), 451-463.

Holgerson, M. A., and P. A. Raymond (2016), Large contribution to inland water CO2 and CH4 emissions from very small ponds, *Nature Geoscience*, *9*, 222-226.

Holtz, R. D., and W. D. Kovacs (2010), *An Intrudction to Geotechnical Engineering*, Prentice Hall, New Jersey.

Hornbach, M., D. Saffer, and W. Holbrook (2004), Critically pressured free-gas reservoirs below gas-hydrate provinces, *Nature*, *427*(6970), 142-144.

Huttunen, J., T. Vaisanen, S. Hellsten, and P. Martikainen (2006), Methane fluxes at the sediment-water interface in some boreal lakes and reservoirs, *Boreal Environment Research*, *11*(1), 27-34.

Illian, J., A. Penttinen, H. Stoyan, and D. Stoyan (2008), *Statistical Analysis and Modelling of Spatial Point Patterns*, Wiley, West Sussex, England.

IPCC (2013), *Climate Change 2013: The Physical Science Basis. Contribution of Working Group I to the Fifth Assessment Report of the Intergovernmental Panel on Climate Change*, 1535 pp., Cambridge University Press, Cambridge, United Kingdom and New York, NY, USA.

Isaksen, I. S. A., M. Gauss, G. Myhre, K. M. W. Anthony, and C. Ruppel (2011), Strong atmospheric chemistry feedback to climate warming from Arctic methane emissions, *Global Biogeochemical Cycles*, *25*.

Jain, A. K., and R. Juanes (2009), Preferential mode of gas invasion in sediments: Grain-scale mechanistic model of coupled multiphase fluid flow and sediment mechanics, *Journal of Geophysical Research*, *114*, B08101.

Johnson, B., B. Boudreau, B. Gardiner, and R. Maass (2002), Mechanical response of sediments to bubble growth, *Marine Geology*, *187*(3-4), 347-363.

Joyce, J., and P. W. Jewell (2003), Physical Controls on Methane Ebullition from Reservoirs and Lakes, *Environmental & Engineering Geoscience*, *IX*(2), 167-178.

Keller, M., and R. Stallard (1994), Methane emission by bubbling from Gatun Lake, Panama, *Journal of Geophysical Research*, *99*(D4), 8307-8319.

Kelly, C., and D. Chynoweth (1981), The contributiions of temperature and of the input of organic matter in controlling rates of sediment methanogenesis, *Limnology and Oceanography*, *26*(5), 891-897.

Kirschke, S., et al. (2013), Three decades of global methane sources and sinks, *Nature Geoscience*, *6*(10), 813-823.

Klein, S. (2006), Sediment porewater exchange and solute release during ebullition, *Marine Chemistry*, *102*(1-2, Sp. Iss. SI), 60-71, 8th International Estuarine Biogeochemistry Symposium, Solomons, MD, MAY, 2004.

Kong, X.-Z., W. Kinzelbach, and F. Stauffer (2009), Migration of air channels: An instability of air flow in mobile saturated porous media, *Chemical Engineering Science*, *64*(7), 1528-1535.

Kong, X.-Z., W. Kinzelbach, and F. Stauffer (2010), Compaction and size segregation in a liquid-saturated grain packing due to pulsation effect during air injection, *Chemical Engineering Science*, *65*(9), 2680-2688.

Kuipphet, G., and C. Martens (1982), Biogeochemical cycling in an organic-rich coastal marine basin. 3. Dissolved gas transport in methane-saturated sediments, *Geochimica et Cosmochimica Acta*, *46*(11), 2049-2060.

Leifer, I. (2010), Characteristics and scaling of bubble plumes from marine hydrocarbon seepage in the Coal Oil Point seep field, *Journal of Geophysical Research*, *115*.

Leifer, I., and J. Boles (2005), Turbine tent measurements of marine hydrocarbon seeps on subhourly timescales, *Journal of Geophysical Research*, *110*, C01006.

Leifer, I., B. P. Luyendyk, J. Boles, and J. F. Clark (2006), Natural marine seepage blowout: Contribution to atmospheric methane, *Global Biogeochemical Cycles*, *20*(3).

Leitch, A., and W. Baines (1989), Liquid volume flux in a weak bubble plume, *Journal of Fluid Mechanics*, *205*, 77-98.

Liikanen, A., T. Murtoniemi, H. Tanskanen, T. Vaisanen, and P. Martikainen (2002), Effects of temperature and oxygen availability on greenhouse gas and nutrient dynamics in sediment of a eutrophic mid-boreal lake, *Biogeochemistry*, *59*(3), 269-286.

Liu, X., and P. B. Flemings (2007), Dynamic multiphase flow model of hydrate formation in marine sediments, *Journal of Geophysical Research*, *112*, B03101.

Lubarda, V. A., and K. A. Talke (2011), Analysis of the Equilibrium Droplet Shape Based on an Ellipsoidal Droplet Model, *Langmuir*, *27*(17), 10705-10713.

Maeck, A., T. DelSontro, D. F. McGinnis, H. Fischer, S. Flury, M. Schmidt, P. Fietzek, and A. Lorke (2013a), Sediment trapping by dams creates methane emission hot spots, *Environmental Science & Technology*, *47*(15), 8130-8137.

Maeck, A., H. Hofmann, and A. Lorke (2013b), Pumping methane out of aquatic sediments; forcing mechanisms that affect the temporal dynamics of ebullition, *Biogeosciences Discussions*, *10*(11), 18687–18722.

Martens, C., and J. val Klump (1980), Biogeochemical cycling in an organic-rich coastal marine basin. 1. Methane sediment-water exchange processes, *Geochimica et Cosmochimica Acta*, *44*(3), 471-490.

Mattson, M. D., and G. Likens (1990), Air pressure and methane fluxes, *Nature*, *347*(6295), 718-719.

McGinnis, D. F., J. Greinert, Y. Artemov, S. E. Beaubien, and A. Wuest (2006), Fate of rising methane bubbles in stratified waters: How much methane reaches the atmosphere?, *Journal of Geophysical Research*, *111*, C09007.

McGlade, C., and P. Ekins (2015), The geographical distribution of fossil fuels unused when limiting global warming to 2 degrees C, *Nature*, *517*(7533), 187-U143.

Medwin, H., and S. Clay (1998), *Fundamentals of Acoustical Oceanography (Applications of Modern Acoustics)*, Academic Press Limited.

Meier, J. A., J. S. Jewell, C. E. Brennen, and J. Imberger (2011), Bubbles emerging from a submerged granular bed, *Journal of Fluid Mechanics*, *666*, 189-203.

Meinshausen, M., N. Meinshausen, W. Hare, S. C. B. Raper, K. Frieler, R. Knutti, D. J. Frame, and M. R. Allen (2009), Greenhouse-gas emission targets for limiting global warming to 2 degrees C, *Nature*, *458*(7242), 1158-1162.

Merckelbach (2000), Consolidation and strength evolution of soft mud layers, Ph.D. Thesis, UT Delft.

Merckelbach, L. M., C. Kranenburg, and J. C. Winterwerp (2002), Strength modelling of consolidating mud beds, *Proceedings in Marine Science*, *5*, 359-373.

Muyakshin, S. I., and E. Sauter (2010), The hydroacoustic method for the quantification of the gas flux from a submersed bubble plume, *Oceanology*, *50*(6), 1045-1051.

Nakamura, T., Y. Nojiri, M. Utsumi, T. Nozawa, and A. Otsuki (1999), Methane emission to the atmosphere and cycling in a shallow eutrophic lake, *Archiv fur Hydrobiologie*, *144*(4), 383-407.

Naudts, L., J. Greinert, Y. Artemov, P. Staelens, J. Poort, P. Van Rensbergen, and M. De Batist (2006), Geological and morphological setting of 2778 methane seeps in the Dnepr paleo-delta, northwestern Black Sea, *Marine Geology*, *227*(3-4), 177-199.

Nikolovska, A., H. Sahling, and G. Bohrmann (2008), Hydroacoustic methodology for detection, localization, and quantification of gas bubbles rising from the seafloor at gas seeps from the eastern Black Sea, *Geochemistry Geophysics Geosystems*, *9*.

Ohser, J., and F. Mücklich (2000), *Statistical Analysis of Microstructures in Materials Science*, Wiley, West Sussex, England.

Osti, G., F. Wolf, and P. Philippi (2009), Spreading of liquid drops on acrylic surfaces, in *Proceedings of the 20th International Congress of Mechanical Engineering*, Gramado, RS, Brazil.

Ostrovsky, I., D. F. McGinnis, L. Lapidus, and W. Eckert (2008), Quantifying gas ebullition with echosounder: the role of methane transport by bubbles in a medium-sized lake, *Limnology and Oceanography-Methods*, *6*, 105-118.

Pacala, S., and R. Socolow (2004), Stabilization wedges: Solving the climate problem for the next 50 years with current technologies, *Science*, *305*(5686), 968-972.

Paull, C., B. Schlining, W. Ussler, J. Paduan, D. Caress, and H. Greene (2005), Distribution of chemosynthetic biological communities in Monterey Bay, California, *Geology*, *33*(2), 85-88.

Price, P., and T. Sowers (2004), Temperature dependence of metabolic rates for microbial growth, maintenance, and survival, *Proceedings of the National Academy of Science*, *101*(13), 4631-4636.

Queré, D. (2005), Non-sticking drops, *Reports on Progress in Physics*, *68*, 2495-2532.

Ramos, G., G. Varas, J.-C. Géminard, and V. Vidal (2015), Gas-induced fluidization of mobile liquid-saturated grains, *Phys. Rev. E*, *92*, 062210.

Reagan, M. T., and G. J. Moridis (2007), Oceanic gas hydrate instability and dissociation under climate change scenarios, *Geophysical Research Letters*, *34*(22).

Rehder, G., P. Brewer, E. Peltzer, and G. Friederich (2002), Enhanced lifetime of methane bubble streams within the deep ocean, *Geophysical Research Letters*, *29*(15).

Rehder, G., I. Leifer, P. G. Brewer, G. Friederich, and E. T. Peltzer (2009), Controls on methane bubble dissolution inside and outside the hydrate stability field from open ocean field experiments and numerical modeling, *Marine Chemistry*, *114*(1-2), 19-30.

Roemer, M., M. Scherwath, M. Heesemann, G. Spence, and M. Riedel (2015), Tidal influence on gas bubble emissions from permanent seafloor observations at Ocean Networks Canada's cabled array NEPTUNE, poster OS31B-02 at AGU Fall 2015 Conference, presented 12/16/15.

Rudd, J., R. Hamilton, and N. Campbell (1974), Measurement of Microbial Oxidation of Methane in Lake Water, *Limnology and Oceanography*, *19*(3), 519-524.

Ruppel, C. D. (2011), Methane Hydrates and Contemporary Climate Change, *Nature Education Knowledge*, *3*(10), 29.

Scandella, B. P. (2010), Numerical modeling of methane venting from lake sediments, Master's Thesis, Massachusetts Institute of Technology, Cambridge, Massachusetts.

Scandella, B. P., and R. Juanes (2011), Numerical Modeling of Hydrate Formation and Methane Gas Transport Through Dynamic Conduits, in *Proceedings of the 7th International Conference on Gas Hydrates*, Edinburgh, Scotland, United Kingdom.

Scandella, B. P., C. Varadharajan, H. F. Hemond, C. Ruppel, and R. Juanes (2011), A conduit dilation model of methane venting from lake sediments, *Geophysical Research Letters*, *38*, L06408.

Scandella, B. P., L. Pillsbury, T. Weber, C. Ruppel, H. F. Hemond, and R. Juanes (2016), Ephemerality of discrete methane vents in lake sediments, *Geophysical Research Letters*, *43*, 2016GL068668.

Schmidt, K. A. G., G. K. Folas, and B. Kvamme (2007), Calculation of the interfacial tension of the methane-water system with the linear gradient theory, *Fluid Phase Equilibria*, *261*(1-2, Sp. Iss. SI), 230-237, 11th International Conference on Propeties and Phase Equilibria for Product and Process Design, Crete, GREECE, MAY 20-25, 2007.

Schneider von Deimling, J., G. Rehder, D. McGinnnis, J. Greinert, and P. Linke (2011), Quantification of seep-related methane gas emissions at Tommeliten, North Sea, *Continental Shelf Research*, *31*, 867-878.

Shakhova, N., et al. (2014), Ebullition and storm-induced methane release from the East Siberian Arctic Shelf, *Nature Geoscience*, *7*(1), 64-70.

Sills, G. C., S. J. Wheeler, S. D. Thomas, and N. T. Gardner (1991), Behavior of offshore soils containing gas-bubbles, *Geotechnique*, *41*(2), 227-241.

Skarke, A. D., C. D. Ruppel, M. Kodis, D. Brothers, and E. Lobecker (2014), Widespread methane leakage from the sea floor on the northern US Atlantic margin, *Nature Geoscience*, *7*(9), 657-661.

Spence, G. (2016), Instrument Information: Multibeam Rotary Sonar. Oceans Network Canada. Published online at http://www.oceannetworks.ca/installations/infrastructure/instrument-info/33, accessed 4/27/16.

Spliethoff, H., and H. Hemond (1996), History of toxic metal discharge to surface waters of the Aberjona Watershed, *Environmental Science & Technology*, *30*(1), 121-128.

Stapelberg, R. F. (2009), *Handbook of Reliability, Availability, Maintainability and Safety in Engineering Design*, Springer, London.

Strayer, R., and J. Tiedje (1978), In situ methane production in a small, hypereutrophic, hard-water lake: loss of methane from sediments by vertical diffusion and ebullition, *Limnology and Oceanography*, *23*(6), 1201-1206.

Thomanek, K., O. Zielinski, H. Sahling, and G. Bohrmann (2010), Automated gas bubble imaging at sea floor - a new method of in situ gas flux quantification, *Ocean Science*, *6*(2), 549-562.

Tokida, T., T. Miyazaki, M. Mizoguchi, O. Nagata, F. Takakai, A. Kagemoto, and R. Hatano (2007), Falling atmospheric pressure as a trigger for methane ebullition from peatland, *Global Biogeochemical Cycles*, *21*(2), GB2003.

Torres, M., J. McManus, D. Hammond, M. de Angelis, K. Heeschen, S. Colbert, M. Tryon, K. Brown, and E. Suess (2002), Fluid and chemical fluxes in and out of sediments hosting methane hydrate deposits on Hydrate Ridge, OR, I: Hydrological provinces, *Earth and Planetary Science Letters*, *201*(3-4), 525-540.

Vallebuona, G., A. Casali, and W. Kracht (2005), Characterization and modeling of bubbles size distribution in mechanical flotation cells, *Revista de Metalurgia*, *41*(4), 243-250.

van Huissteden, J., C. Berrittella, F. J. W. Parmentier, Y. Mi, T. C. Maximov, and A. J. Dolman (2011), Methane emissions from permafrost thaw lakes limited by lake drainage, *Nature Climate Change*, *1*(2), 119-123.

Varadharajan, C. (2009), Magnitude and Spatio-Temporal Variability of Methane Emissions from a Eutrophic Freshwater Lake, Ph.D. Thesis, Massachusetts Institute of Technology, Cambridge, Massachusetts.

Varadharajan, C., and H. F. Hemond (2012), Time-series analysis of high-resolution ebullition fluxes from a stratified, freshwater lake, *Journal of Geophysical Research*, *117*, G02004.

Varas, G., V. Vidal, and J.-C. Geminard (2009), Dynamics of crater formations in immersed granular materials, *Physical Review E*, *79*(2, Part 1).

Varas, G., V. Vidal, and J.-C. Géminard (2011), Venting dynamics of an immersed granular layer, *Physical Review E*, *83*(1), 011302.

Veloso, M., J. Greinert, J. Mienert, and M. De Batist (2015), A new methodology for quantifying bubble flow rates in deep water using splitbeam echosounders: Examples from the Arctic offshore NW-Svalbard, *Limnology and Oceanography-Methods*, *13*(6), 267-287.

Walter, K. M., S. A. Zimov, J. P. Chanton, D. Verbyla, and F. S. Chapin, III (2006), Methane bubbling from Siberian thaw lakes as a positive feedback to climate warming, *Nature*, *443*, 71-75.

Walter Anthony, K. M., and P. Anthony (2013), Constraining spatial variability of methane ebullition seeps in thermokarst lakes using point process models, *Journal of Geophysical Research*, *118*(3), 1015–1034.

Walter Anthony, K. M., P. Anthony, G. Grosse, and J. Chanton (2012), Geologic methane seeps along boundaries of Arctic permafrost thaw and melting glaciers, *Nature Geoscience*, *5*, 419-426.

Wang, B., S. A. Socolofsky, J. A. Breier, and J. S. Seewald (2016), Observations of bubbles in natural seep flares at MC 118 and GC 600 using in situ quantitative imaging, *Journal of Geophysical Research*, *121*, 2203–2230.

Weber, T. C., L. Mayer, K. Jerram, J. Beaudoin, Y. Rzhanov, and D. Lovalvo (2014), Acoustic estimates of methane gas flux from the seabed in a 6000 km2 region in the Northern Gulf of Mexico, *Geochemistry, Geophysics, Geosystems*, *15*(5), 1911–1925.

Westbrook, G. K., et al. (2009), Escape of methane gas from the seabed along the West Spitsbergen continental margin, *Geophysical Research Letters*, *36*, L15608.

Wheeler, S. J., W. K. Sham, and S. D. Thomas (1990), Gas-pressure in unsaturated offshore soils, *Canadian Geotechnical Journal*, *27*(1), 79-89.

Wiegand, T., and K. A. Moloney (2014), *Handbook of Spatial Point Pattern Analysis*, Chapman and Hall, Boca Raton, FL.

Wik, M., P. M. Crill, D. Bastviken, A. Danielsson, and E. Norback (2011), Bubbles trapped in arctic lake ice: Potential implications for methane emissions, *Journal of Geophysical Research*, *116*, G03044.

Wik, M., P. M. Crill, R. K. Varner, and D. Bastviken (2013), Multiyear measurements of ebullitive methane flux from three subarctic lakes, *Journal of Geophysical Research*, *118*(3), 1307-1321.

Wik, M., B. F. Thornton, D. Bastviken, S. MacIntyre, R. K. Varner, and P. M. Crill (2014), Energy input is primary controller of methane bubbling in subarctic lakes, *Geophysical Research Letters*, *41*(2), 555-560.

Wik, M., B. F. Thornton, D. Bastviken, J. Uhlbäck, and P. M. Crill (2016), Biased sampling of methane release from northern lakes: A problem for extrapolation, *Geophysical Research Letters*, *43*, 1256–1262.

Witherspoon, P. A., and D. N. Saraf (1965), Diffusion of methane, ethane, propane and n-butane in water from 25 to 43 degrees, *Journal of Physical Chemistry*, *69*(11), 3752-3755.

Yamamoto, A., M. Hirota, S. Suzuki, Y. Oe, P. Zhang, and S. Mariko (2009), Effects of tidal fluctuations on CO2 and CH4 fluxes in the littoral zone of a brackish-water lake, *Limnology*, *10*(3), 228-237.

Yapa, P. D., L. K. Dasanayaka, U. C. Bandara, and K. Nakata (2008), Modeling the Impact of an Accidental Release of Methane Gas in Deepwater, in *Oceans*, pp. 109–118, IEEE, 345 E 47TH ST, NEW YORK, NY 10017 USA, oCEANS 2008 Conference, Quebec City, CANADA, SEP 15-18, 2008.

Yuan, Q., K. T. Valsaraj, D. D. Reible, and C. S. Willson (2007), A laboratory study of sediment and contaminant release during gas ebullition, *Journal of the Air & Waste Management Association*, *57*(9), 1103-1111.

Yvon-Durocher, G., A. P. Allen, D. Bastviken, R. Conrad, C. Gudasz, A. St-Pierre, N. Thanh-Duc, and P. A. del Giorgio (2014), Methane fluxes show consistent temperature dependence across microbial to ecosystem scales, *Nature*, *507*, 488-491.

Zeng, Q., and J. Cai (2014), Three-dimension simulation of bubble behavior under nonlinear oscillation, *Annalso of Nuclear Energy*, *63*, 680-690.

Zinder, S. H. (1993), *Methanogenesis: Ecology, Physiology, Biochemistry and Genetics*, chap. Physiological ecology of methanogens, Chapman and Hall.